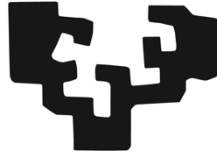


eman ta zabal zazu



Universidad
del País Vasco

Euskal Herriko
Unibertsitatea

PhD Thesis

Surface Engineering of Biomimetic Antibacterial and Biocompatible Hybrid Materials Through Molecular Layer Deposition

Karina Ashurbekova

Supervised by Prof. Mato Knez

2022

This PhD thesis has been carried out at:

CIC nanoGUNE

Nanomaterials group

Donostia, Spain

The tutor of this dissertation was

Prof. Dr. Jose M. Pitarke



Abstract

Evolution has led to a variety of processes, algorithms, materials, and designs that are constantly being improved for optimizing the efficiency of their operation. Biomineralization is a natural concept of manipulating the mechanical properties of materials, often to harden or stiffen existing tissues, while preserving certain features like lightness, ductility, etc. Among the most typical examples of mineralized tissues are bone and teeth, both are extremely strong materials but at the same time are elastic and able to compensate stress.

Biomimicry is an opportunity for humanity to innovate by imitating and manipulating naturally occurring biological systems. From the materials science perspective, mimicking biomineralization became highly interesting with a resulting vast variety of approaches towards realizing functional hybrid materials. The imitation of this concept has led to a large variety of approaches to the fabrication and application of functional hybrid materials.

Besides the mechanical properties, natural materials have plenty further functionalities which are worth of mimicking. Among the most prominent functions is the protection against microbes. In the present work, we are mimicking a biomineralization process by creating hybrid materials of various types of naturally occurring materials with inorganics to fabricate antibacterial and biocompatible thin films for various applications in future.

Chapter 3 of this thesis highlights a new method for obtaining ultrathin conformal films composed of chitin and chitin-based organic-inorganic hybrid biomaterials from the gas phase by molecular layer deposition (MLD). MLD is a solvent-free deposition technique in which a nanoscale film is grown on a substrate through successive self-limiting gas-solid interface reactions. The technique enables the growth of both organic and hybrid organic-inorganic films. A distinctive feature of this technology is the precise control of the composition and thickness of the deposited films, the high degree of conformality of coatings and their excellent adhesion due to the chemisorptive nature of the surface reactions. We applied this method for the first solid foundation for the growth of conformal ultrathin functional films of chitin-based hybrid biomaterials, which we term metallochitins or, more generally, metallosaccharides. Inspired by the properties of natural chitin, we have developed a series of bioactive coatings by fusion of sugar-type molecular precursors with metalorganic compounds. A variety of experimental (FTIR, QCM, XPS, XRR, HR-TEM, EELS, EDX) and theoretical (DFT) studies were performed

to confirm the metallochitin film growth and characterize their composition and structure. The evaluation of the antimicrobial activity and biocompatibility of alumochitin and titanochitin MLD film was also assessed. In vitro tests have confirmed that from the bioactivity prospect the metallosaccharides are an excellent analogue of natural chitin, stimulating cell growth and proliferation, while simultaneously preventing the adhesion of Gram-negative and Gram-positive bacteria.

Silicon-based polymeric thin films have shown a unique combination of physical and biological properties and are currently intensely investigated. They promise great advances in the biomedical field for smart nanotechnology-based devices, tissue targeting, drug delivery and biocompatible packaging of implantable medical devices e.g., neural prosthesis in near future. Biocompatible packaging plays an increasingly important role in implantable medical devices due to the emergence of new technologies such as neural prosthesis. Because the encapsulation polymer has multiple interfaces with packaged objects (sensors, Si chip, pins, and bond wire), the poor adhesion of encapsulation polymer to various interfaces and their non-conformal growth often results in voids or microcracks and eventually leads to interfacial delamination. Therefore, there is a need to develop processes for strongly adhering flexible, conformal, and soft biocompatible ultrathin layers, which is challenging with conventional solution-based deposition methods, spin-coating, or CVD techniques.

Chapter 4 of this thesis investigates such silicon-based films with application potential in packaging or further biomedical applications. We explored the MLD growth of a new materials group of hybrid alumosilazane. The hybrid alumosilazanes were for the first time synthesized as thin films from the vapor phase by utilizing a ring-opening reaction of 2,4,6-trimethyl-2,4,6-trivinylcyclotrisilazane (V_3N_3) and coupling it with trimethylaluminum (TMA). XPS, FT-IR, and in-situ QCM were employed to analyze the structural changes, composition, and the growth dynamics of the film. The developed process has proven to be stable and easy to control, while the used materials are not critical to handle. Furthermore, it can be applied to particles or surfaces with any kind of morphology. The biocompatibility of the hybrid organic–inorganic alumosilazane (Si-ALCNH) films was assessed with the growth of Human Embryonic Kidney (HEK293T) cells. The strong adhesion to substrates, and conformal growth, assets of the MLD technique, allow the formation of flexible high-quality silazane-alumina and siloxane-alumina thin films with excellent biocompatibility that have an application potential as ultrathin bioactive coatings for surface grafting of artificial joints, encapsulation of implantable or analytical biomedical devices with complex topologies and high-aspect-ratio structures.

Poly(2-oxazolines) (POx) are considered pseudopeptides, i.e., bioinspired polymers, due to their structural relationship to polypeptides. POx have a special place in the field of polymer science due to their features and properties. The most priority areas for the

use of such polymers are medicine, biotechnology, and bioengineering. Their biocompatibility, non-toxicity, as well as the ability to form complexes with low molecular weight compounds allow them to be considered as medical polymers. Currently, poly-2-alkyl-2-oxazolines are already used for drug delivery and gels to suppress bleeding, but they are exclusively synthesized in a wet-chemical way.

Chapter 5 of the thesis reports on the first gas-phase solvent-free synthesis of POx via living cationic ring-opening polymerization. For this a new type of MLD process has been developed, which uses p-Toluenesulfonyl chloride (TosCl) as initiator for polymerizations of 2-methyl-2-oxazoline, 2-phenyl-2-oxazoline and 2-isopropenyl-2-oxazoline.

The demonstrated gas-phase POx synthesis includes two steps: initiation and propagation. To stop the polymerization, a terminating agent, which forms a stable bond with the living cationic chain end, is needed. During the initiation stage, a substrate is exposed to TosCl vapors which leads to the formation of a tosyl-functionalized monolayer. The second step is the chain propagation, which includes alternating pulse/purge sequences of the monomer. The monomers undergo a cationic ring-opening polymerization reaction upon contact with the tosyl-functionalized substrate and in this way grow a POx backbone with a living oxazolinium chain-end. The living polymer chains can be terminated with a pulse of water vapor. This approach has proven to be very efficient as it ensures the conformality of the grown film, the absence of impurities, thickness control, and strong adhesion of coatings to most substrates due to the chemisorption nature of surface reactions.

Resumen

El progreso de nuestra civilización y el bienestar de la humanidad implica el desarrollo perpetuo de materiales funcionales sofisticados. Las superficies multifuncionales con biocompatibilidad mejorada que previenen simultáneamente la contaminación bacteriana y la formación de biopelículas son un gran desafío y un importante escenario de la investigación actual sobre biomateriales.

La naturaleza es la fuente de una variedad de procesos, algoritmos, materiales y diseños que la humanidad intenta imitar. La biomimética representa una oportunidad para que la humanidad innove imitando y manipulando sistemas biológicos naturales.. La biomineralización es un concepto natural de producción de minerales, a menudo para endurecer o endurecer los tejidos existentes. La imitación de este concepto esta en el punto de mira tecnológico, lo que ha dado lugar a una amplia variedad de enfoques para la implementación de materiales híbridos funcionales. Uno de los ejemplos más típicos de tejidos mineralizados son los huesos y los dientes, ambos son materiales extremadamente fuertes pero al mismo tiempo son elásticos pudiendo compensar la tensión.

En un enfoque bioinspirado, estamos imitando una biomineralización creando varios tipos de materiales naturales para hacer películas delgadas, híbridas, antibacterianas y biocompatibles para una variedad de aplicaciones.

El trabajo presentado en el primer capítulo destaca un nuevo método para la obtención de películas de quitina ultrafinas conformes y biomateriales híbridos a base de quitina a partir de la fase gaseosa mediante Deposición de Capas Moleculares (MLD). MLD es un enfoque libre de solventes, en el que la estructura se construye a través de sucesivas reacciones autolimitantes de gas-sólido, lo que permite el crecimiento de materiales híbridos orgánicos e inorgánicos. Una característica distintiva de esta tecnología es el control preciso de la composición y el espesor de las películas depositadas, el alto grado de conformidad de los recubrimientos sobre sustratos nanoestructurados y la excelente adhesión debido a la naturaleza de quimisorción de las reacciones superficiales.

Este trabajo proporciona la primera base sólida para el crecimiento de películas funcionales ultrafinas conformes de biomateriales híbridos basados en quitina, que denominamos metaloquitinas o, más generalmente, metallosacáridos. Inspirándonos en las propiedades de la quitina natural, hemos desarrollado una serie de recubrimientos bioactivos por fusión de precursores moleculares tipo azúcar con compuestos metalorgánicos a través de MLD. Se realizaron una variedad de estudios experimentales (FTIR, QCM, XPS, XRR, HR-TEM, EELS, EDX) y teóricos (DFT) para

confirmar el crecimiento de la película de metaloquitina y caracterizar su composición y estructura. Se evaluó *in vitro* la actividad antimicrobiana de las películas de metaloquitina frente a bacterias grampositivas (*Staphylococcus aureus*, *S. aureus*) y gramnegativas (*Escherichia coli*, *E. coli*).

Las micrografías confocales resultantes de biopelículas bacterianas de *E. coli* teñidas se muestran en la Figura 1.

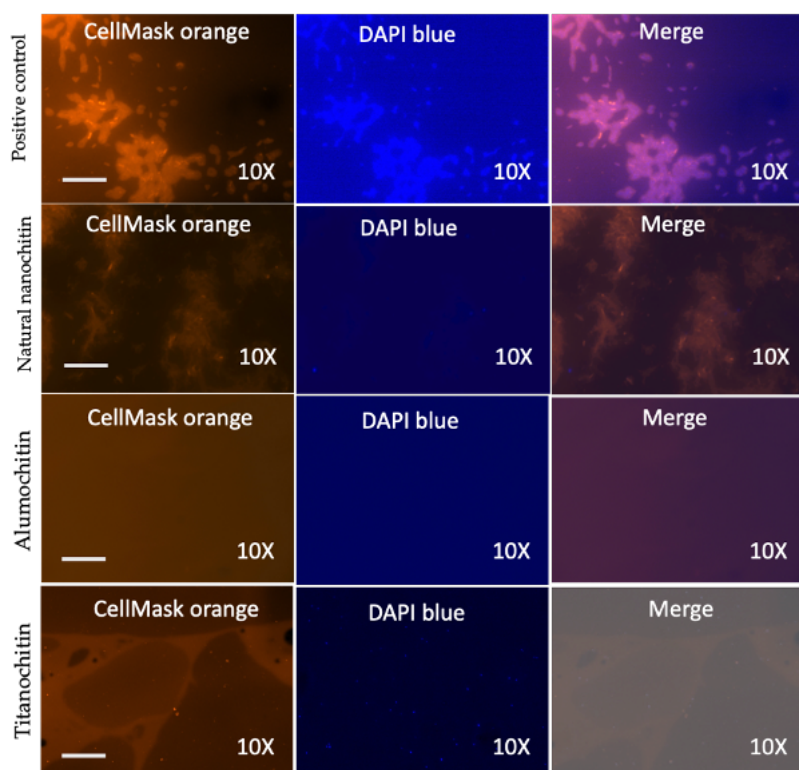


Figura R1: Actividad antibacteriana de alumoquitina y titanochitina frente a bacterias Gram negativas (*E. coli*). Micrografías confocales de biopelícula bacteriana de *E. coli* sobre sustratos de alumoquitina y titanochitina después de 24 h de exposición con dos aumentos originales diferentes, 10x (barra de escala = 10 μm). Se ha utilizado una película MLD híbrida de aluminosilazano (SiAlCNH) basada en silicio de 25 nm de espesor como sustrato de control positivo para el crecimiento de *E. coli*. No se observó crecimiento bacteriano en las muestras de control negativo (muestras expuestas solo al medio, pero sin bacterias), como se esperaba. Tanto las bacterias gramnegativas como las grampositivas se tiñeron con DAPI (azul) y CellMask naranja para marcar las membranas plasmáticas y los núcleos, respectivamente.

La alumoquitina demostró actuar de forma antimicrobiana al inhibir la adhesión de ambos tipos de bacterias, lo que en última instancia suprime la formación de biopelículas. Curiosamente, la titanochitina tenía una actividad antimicrobiana

selectiva contra las bacterias gramnegativas, pero permitía la formación de biopelículas bacterianas grampositivas. El origen de las actividades antimicrobianas puede estar en la carga de la superficie, la rugosidad, la humectabilidad y la química del sustrato, todo lo cual puede tener un impacto en la unión e interacción de las cepas bacterianas con el sustrato. El comportamiento diferente de ambas metaloquitinas frente a ambos tipos de bacterias probablemente se deba al potencial zeta más positivo y, por lo tanto, a la carga superficial de la alumoquitina en comparación con la titanoquitina y a la carga más negativa de las bacterias gramnegativas en comparación con las bacterias grampositivas.

Esto sugiere una interacción electrostática más débil de la titanoquitina con la bacteria *S. aureus* y, en consecuencia, una menor tendencia a la ruptura física de la pared celular. Además, la pared celular más gruesa y la ausencia de una membrana celular externa en *S. aureus* contribuyen a su estabilización. Eventualmente, la actividad antibacteriana de las dos metaloquitinas probadas difiere entre sí, lo cual es un punto muy intrigante ya que otorga un enorme potencial de aplicación para el diseño y desarrollo de superficies antimicrobianas selectivas. Es importante destacar que los grupos funcionales que se cree que son responsables de la actividad antimicrobiana se conservaron durante la síntesis de MLD.

Se evaluó la biocompatibilidad in vitro de las metaloquitinas caracterizadas por el cultivo de riñón embrionario humano (HEK293T) y células de fibroblastos humanos en las películas de metaloquitina. Ambas metaloquitinas mostraron una mayor proliferación celular que los cubreobjetos sin recubrimiento que se usaron como muestras de referencia y en ambas investigaciones celulares.

Por lo tanto, las pruebas in vitro han confirmado que, desde el punto de vista de la bioactividad, los metalosacáridos son un excelente análogo de la quitina natural, estimulando el crecimiento y la proliferación celular, al mismo tiempo que previenen la adhesión de bacterias Gram-negativas y Gram-positivas.

Existe una demanda de nuevos biomateriales que puedan reemplazar los tejidos dañados, estimular los propios mecanismos de regeneración del cuerpo y promover la curación de los tejidos.

Las biocerámicas son de gran interés en el campo de la biomedicina por su biocompatibilidad, dureza, resistencia a la abrasión y extrema durabilidad, y se suelen utilizar como materiales rígidos en implantes quirúrgicos para reducir el desgaste y la respuesta inflamatoria. Por lo general, las biocerámicas se han utilizado para la reparación de tejidos duros, pero recientemente esta categoría de biomateriales también ha encontrado aplicaciones prometedoras en el campo de la ingeniería de tejidos blandos. La ingeniería de tejidos requiere una gran biocompatibilidad de la matriz para promover el crecimiento de tejido deseado. La matriz puede ser rígida o

flexible y tener varias morfologías, las formas de funcionalización de la superficie y los resultados de funcionalidad resultantes son de importancia crítica.

Las películas delgadas poliméricas a base de silicio han mostrado una combinación única de propiedades físicas y biológicas, las cuales en la actualidad se investigan con gran intensidad. Hoy en día, se observan grandes avances en el campo biomédico para dispositivos inteligentes basados en nanotecnología, selección de tejidos, administración de fármacos y envases biocompatibles de dispositivos médicos implantables, por ejemplo, prótesis neurales en un futuro próximo. Los envases biocompatibles desempeñan un papel cada vez más importante en los dispositivos médicos implantables debido a la aparición de nuevas tecnologías, como las prótesis neurales. Debido a que el polímero de encapsulación tiene múltiples interfaces con objetos empaquetados (sensores, chip de Si, clavijas y alambre de enlace), la mala adhesión del polímero de encapsulación a varias interfaces y su crecimiento no conforme a menudo da como resultado vacíos o microfisuras y, finalmente, conduce a la delaminación interfacial. Por lo tanto, existe la necesidad de desarrollar procesos para adherir fuertemente capas ultrafinas biocompatibles flexibles, conformes y blandas, lo cual es un desafío con los métodos convencionales de deposición basados en soluciones, el recubrimiento por rotación o las técnicas de CVD.

En la segunda parte de esta tesis, exploramos el crecimiento de MLD de un nuevo grupo de materiales de películas híbridas de aluminosilazano. Desarrollamos un proceso MLD nuevo y de fácil aplicación para cultivar películas a nanoescala de un nuevo tipo de material híbrido silazano-alúmina. Las películas delgadas híbridas de aluminosilazano se sintetizaron por primera vez a partir de la fase de vapor utilizando una reacción de apertura de anillo de 2,4,6-trimetil-2,4,6-trivinilciclotrisilazano (V_3N_3) y acoplándola con trimetilaluminio (TMA). Se emplearon XPS, FT-IR y QCM in situ para analizar los cambios estructurales, la composición y la dinámica de crecimiento de la película. El proceso desarrollado ha demostrado ser estable y fácil de controlar, mientras que los materiales utilizados no son críticos de manipular. Además, se puede aplicar a partículas o superficies y también se puede escalar fácilmente, incluso a nivel industrial.

La principal ventaja de MLD es que permite una excelente conformidad de la película desarrollada, un control extremo del espesor y una fuerte adhesión de los recubrimientos a la mayoría de los sustratos debido a la quimiosorción de los precursores durante las reacciones superficiales.

La biocompatibilidad de las películas híbridas orgánicas-inorgánicas de silazano-alúmina $SiAlCNH$ se evaluó con el crecimiento de células de riñón embrionario humano (HEK293T). La fuerte adhesión a los sustratos y el crecimiento conformado, activos de la técnica MLD, permiten la formación de películas delgadas flexibles de alta calidad de silazano-alúmina y siloxano-alúmina con excelente biocompatibilidad que tienen un

potencial de aplicación como recubrimientos bioactivos ultrafinos para el injerto superficial de tejidos artificiales, articulaciones, encapsulación de dispositivos biomédicos implantables o analíticos con topologías complejas y estructuras de alta relación de aspecto.

En la tercera parte de esta tesis, se reporta la primera síntesis libre de solventes en fase gaseosa de polioxazolininas (POx)s mediante polimerización catiónica viva por apertura de anillo. Las poli(2-oxazolininas) (POxs) se consideran pseudopéptidos, es decir, polímeros bioinspirados, debido a su relación estructural con los polipéptidos. Los POx tienen un lugar especial en el campo de la ciencia de los polímeros debido a sus características y propiedades. Las áreas más prioritarias para el uso de dichos polímeros son la medicina, la biotecnología y la bioingeniería. Su biocompatibilidad, no toxicidad, así como la capacidad de formar complejos con compuestos de bajo peso molecular, les permite ser considerados como polímeros médicos. Actualmente, las poli-2-alkil-2-oxazolininas ya se utilizan en la administración de medicamentos, recubrimientos anti-quemaduras y geles para detener el sangrado.

La polimerización de 2-metil-2-oxazolinina, 2-fenil-2-oxazolinina y 2-isopropenil-2-oxazolinina se ha realizado usando cloruro de p-toluenosulfonilo (TosCl) como iniciador. La Figura 2 representa esquemáticamente el mecanismo para la polimerización catiónica de apertura de anillo de 2-oxazolininas usando tosilato de metilo como

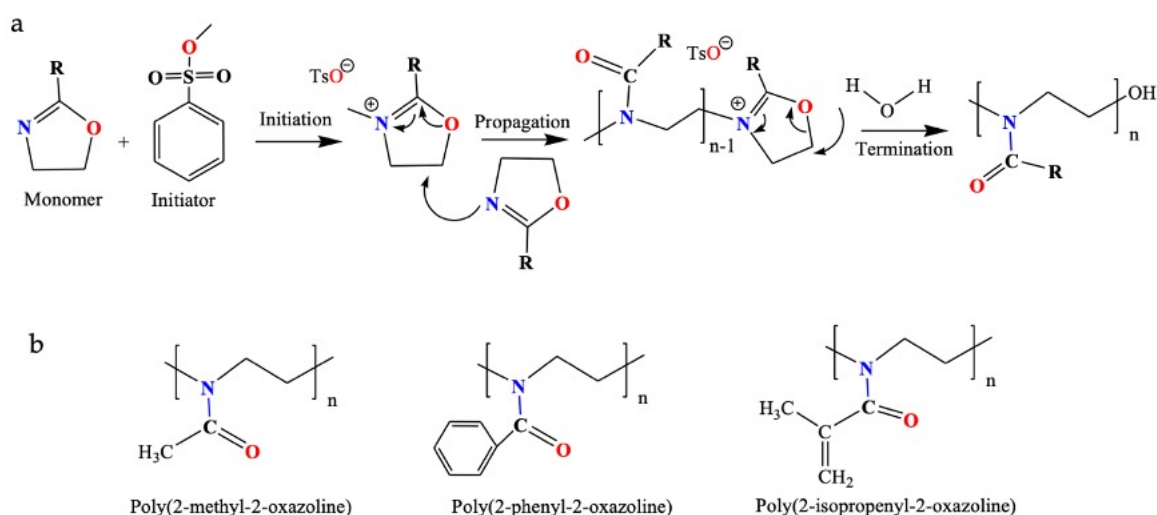


Figura R2: (a) Representación esquemática del mecanismo de polimerización por apertura de anillo catiónico de poli(oxazolininas) iniciado por p-toluenosulfonato y extinguido con agua. (b) Estructuras químicas de los polímeros presentados en este trabajo: Poli(2-metil-2-oxazolinina), Poli(2-fenil-2-oxazolinina) y Poli(2-isopropenil-2-oxazolinina). El grupo R representa el grupo lateral que se puede variar para cambiar las propiedades de las poli(2-oxazolininas) resultantes.

iniciador y H₂O como agente de terminación. Las estructuras químicas de los polímeros obtenidos, presentadas en la figura 2 (b).

La síntesis propuesta de POxs en fase gaseosa incluye dos pasos: iniciación y propagación. Para detener la polimerización, se necesita un agente de terminación que forme un enlace estable con el extremo vivo de la cadena catiónica. Durante la etapa de iniciación, un sustrato se expone a vapores de TosCl, lo que conduce a la formación de una monocapa funcionalizada con tosilo. El segundo paso es la propagación, que incluye pulsos alternos del monómero en la cámara de reacción.

El sustrato funcionalizado con tosilo se utiliza como iniciador para la polimerización de apertura de anillo catiónica viva, donde los monómeros al entrar en contacto con el sustrato funcionalizado con tosilo dan como resultado el esqueleto de poli(2-oxazolona) por apertura de anillo, formación de una amida mientras permanece el extremo vivo de la cadena de oxazolinio. Las cadenas vivas de polímero se pueden terminar directamente con el pulso de agua en la cámara.

Las principales ventajas de este enfoque son que garantiza la conformidad de la película cultivada, la ausencia de impurezas, el control del espesor y una fuerte adhesión de los recubrimientos a la mayoría de los sustratos debido a la naturaleza de quimisorción de las reacciones superficiales.

Por lo tanto, dichos materiales tienen una aplicación potencial en el campo biomédico y podrían aplicarse en dispositivos inteligentes basados en nanotecnología, selección de tejidos y administración de fármacos.

Surface Engineering of Biomimetic Antibacterial and Biocompatible Hybrid Materials Through Molecular Layer Deposition

Abstract

Resumen

Table of Contents

Chapter 1: Introduction	16
1.1 Atomic and Molecular Layer Deposition	17
1.2 Bioactive hybrid materials synthesized by ALD/MLD.....	22
1.3 Natural chitin and chitosan. Bioinspired approach: why chitin?	26
1.4 Synthesis and applications of chitin and chitosan	27
1.5 Hybrid diffusion barriers by ALD/MLD.....	28
1.6 Objective and structure of the thesis.....	31
Chapter 2: Experimental techniques and methods	34
2.1 Laboratory setup for Atomic and Molecular Layer Deposition	36
2.2 In-situ quartz crystal microbalance (QCM)	38
2.3 X-ray photoelectron spectroscopy (XPS)	40
2.4 Fourier transform infrared spectroscopy – attenuated total reflectance (FTIR–ATR)	41
2.5 X-ray Reflectivity (XRR).....	42
2.6 High resolution transmission electron microscopy (HRTEM) and X-ray energy dispersive spectrometry (EDXS) in TEM.....	43
2.7 Thermogravimetry (TG) analysis.....	43

2.8 Experimental setup for Water Vapor Transmission Rate (WVTR) measurements	44
--	----

2.9 Precursors and substrates	45
-------------------------------------	----

Chapter 3: Engineering of Biomimetic, Selectively Antibacterial and Biocompatible Metallochitin Films49

3.1 Introduction.....	51
-----------------------	----

3.2 Experimental details.....	53
-------------------------------	----

3.3 Results	56
-------------------	----

3.3.1 Fabrication of organic chitin thin films by MLD.....	56
--	----

3.3.2 Fabrication of hybrid alumochitin thin films by MLD	60
---	----

3.3.3 Fabrication of hybrid titanochitin thin films by MLD.....	63
---	----

3.4 Mechanistic investigations. DFT analysis of the steric trends of the reaction	67
---	----

3.4.1 Alumochitin DFT studies	67
-------------------------------------	----

3.4.2 Titanochitin DFT studies.....	69
-------------------------------------	----

3.5 Bactericidal activity of the alumochitin and titanochitin MLD films against Gram-positive (Staphylococcus aureus) and Gram-negative (Escherichia coli) bacteria	71
---	----

3.6 Biocompatibility of the metallochitin films	77
---	----

3.6.1 Human Embryonic Kidney (HEK293T) cells growth	77
---	----

3.6.2 Fibroblast cells growth	79
-------------------------------------	----

3.7 Conclusions.....	81
----------------------	----

Chapter 4: Biocompatible Silicon-Based Hybrid Nanolayers for Functionalization of Complex Surface Morphologies.....83

4.1 Introduction.....	85
-----------------------	----

4.2 Experimental details.....	86
4.3 Results and discussion.....	88
4.3.1. Fabrication and Characterization of the MLD Films.....	88
4.3.2 Stability of Alumosilazane and Alumosiloxane MLD films.....	91
4.3.3 Analysis of In-Vitro Biocompatibility Assessment for Human Embryonic Kidney (Hek293T) Cells.....	96
4.3.4 In-Vitro Analysis of Bactericidal activity of the MLD films against Gram- negative (Escherichia coli) bacteria.	99
4.4 Conclusions.....	101
Chapter 5: Bioinspired Peptidomimetic Poly(2-oxazoline)s via Vapor Phase Living Cationic Ring-Opening Polymerization	103
5.1 Introduction.....	104
5.1.1 Biomedical applications of Poly(2-oxazolines)	104
5.1.2 Cationic ring-opening polymerization of 2-oxazolines	106
5.2 Results and discussion.....	110
5.2.1 Living Cationic Ring-Opening Polymerization mechanism of 2-oxazolines	110
5.2.2 Thermogravimetric analysis of the obtained from the gas-phase Polyoxazoline (POx) polymeric films.	117
5.3 Conclusions.....	118
Chapter 6: Summary and Outlook	120
Acknowledgments	124
References.....	126

Chapter 1

Introduction

1.1 Atomic and Molecular Layer Deposition

Atomic layer deposition (ALD) is one of the bottom-up operating technologies for nanomaterials synthesis. This technology has been also known as Molecular Layering (ML) since the early 1960s, when Stanislav Koltsov, Valentin Aleskovsky and colleagues experimentally developed the principles of the technology at the Leningrad Technological Institute (LTI) in the former Soviet Union. The ML technology is based on the “framework” hypothesis proposed by V. B. Aleskovskii in 1952.¹ Later, as much of the soviet research has not been available to the rest of the world, ALD has been developed independently by Tuomo Suntola in 1974 in Finland under the name atomic layer epitaxy (ALE), which is commonly considered as the origin of ALD.

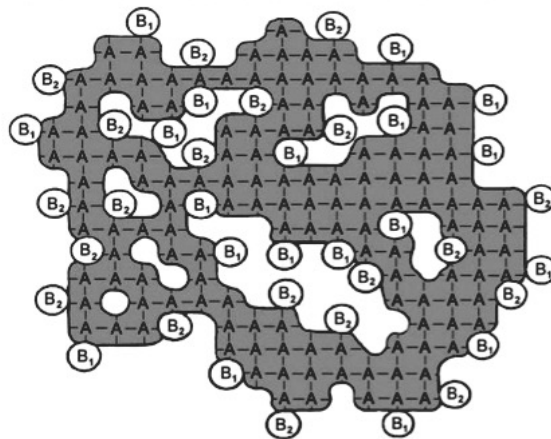


Figure 1.1: The chemical model of a solid proposed by V.B. Aleskovskii.¹

According to the "framework" hypothesis of V.B. Aleskovskii, regardless of the method of synthesizing a solid, one can always distinguish the "core" and the functional surface of a solid matrix. From a chemical point of view, any framework is a macroradical which consists of structural units (A) and functional groups (B) (Figure 1) that form the surface of the framework and are formed due to the chemisorption of atoms and molecules from the environment. From the above, the composition of a solid can be represented as (1):

$$A_{n-s} (AB)_s \quad (1)$$

where n and s are the numbers of structural units (A) and surface functional groups (B), respectively.

According to this structure of solids, the chemical composition of the solid on the surface and in the volume may differ. As a result, some reactions may occur only with the functionalities (B) on the surface of the solid or reactions may be accompanied by a change in the entire core of a solid. Transformations of the first type, when solid substances cognate in structure and composition of the core are obtained, differing only in the set of functionals, form the basis of the ALD technique. The idea of the ALD method consists in consistent growth of monolayers of structural units of a given chemical composition on the surface of a solid-phase matrix. To implement the ALD process, the following principles must be ensured:

1. The chemical ALD reactions between the surface functional groups of the solid and the molecules of the exposed precursors must be irreversible under the experimental conditions.

2. To consistently grow layers of a new material, it is necessary to repeat ALD cycles for the regeneration of surface functional groups.

3. For the ALD reaction to occur, the structural accordance between the surface of the substrate and the given compound is needed, as well as the presence of a sufficient number of functional groups both on the initial surface and on the surface formed during deposition.¹

A schematic illustration of the two step ALD process is shown in Figure 1.2. ALD is a modified version of chemical vapor deposition (CVD) in which a substrate is sequentially exposed to gas-phase precursors, separated by an inert gas purging step.

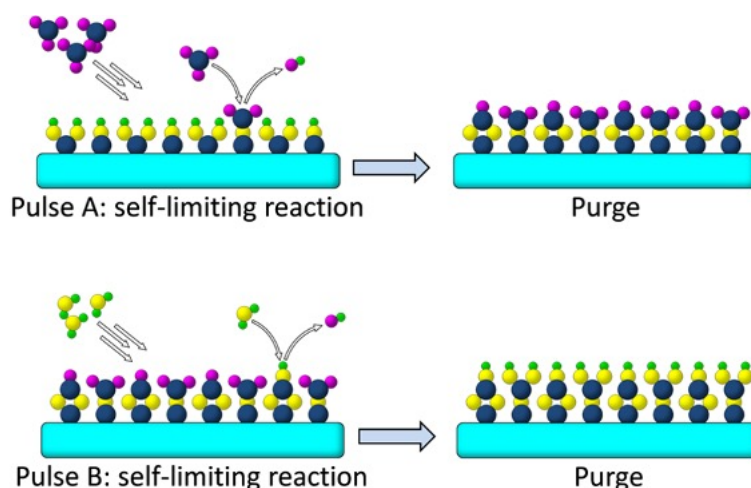


Figure 1.2: Illustration of the ALD process.³ Reprinted with permission from ref. 42. Copyright (2015) American Chemical Society.

First, precursor A reacts selectively with functional surface groups, saturating the surface with the first species. Next, the excess molecules are removed, and a second

precursor B is introduced to react with the adsorbed precursor A and generate a layer of the desired coating material. Repeating these successive exposures results in a constant increase in material per cycle (GPC).

ALD has proven to be the best method to deposit continuous, conformal, and pinhole-free films with superb control over film thickness, composition, and conformality at the atomic level.² Sequential self-limiting surface chemistry is an important requirement for ALD, which grants such film characteristics even on ultrahigh-aspect-ratio structures without gradients in thickness or composition.³

Organic or hybrid organic-inorganic thin films with well-defined composition and conformality can be deposited by a variant of ALD, commonly known as molecular layer deposition (MLD).^{4,5} MLD resembles the benefits of ALD in controlling film thickness, uniformity, conformity, and crystallinity. While ALD is a well-established coating technology, even industrially, with a plethora of developed processes for many inorganic materials and compounds, MLD is still in its infancy in terms of process development and understanding of growth mechanisms.⁶ It still requires considerable attention, since it offers great opportunities for materials development, for example, in the field of bioactive surfaces.

The original work on MLD dates back to early work of Yoshimura et al. in 1991 on layered deposition of a purely organic polyimide.⁷ Subsequently various further organic polymeric materials, such as polyimide, polyamide, polyurea, and crosslinked carbosiloxane, have been synthesized using all-organic precursors based on condensation polymerization reactions.⁸⁻¹¹

By combining organic precursors and inorganic ALD precursors, MLD can be extended to the production of a huge variety of organic-inorganic hybrid materials.¹²

Organic-inorganic hybrids have properties that are intermediate between organic and inorganic materials. The inclusion of organic fragments opens up unlimited possibilities for controlling the final composition of films at the molecular level and tuning their properties in favor of various applications.¹³⁻¹⁵

Various types of hybrid organic-inorganic MLD films known as “metalcones”, e.g., alucone,¹⁶ zincone,^{17,18} titanicone,¹⁹ have been successfully grown. Even mixed organic-inorganic titanium-vanadium and aluminum-vanadium alkoxide thin film alloys have been obtained by MLD,²⁰ showing the versatility of the process and therefore promise for the development of more complex processes.

One of the classic examples of hybrid organic-inorganic materials is alucone, a polymeric aluminum alkoxide with a carbon-containing backbone.

Figure 1.3 (a-d) shows a conformal film of alucone (AlGL), deposited on Si nanoparticles using trimethylaluminum (TMA) and glycerol (GL) as MLD precursors.²¹

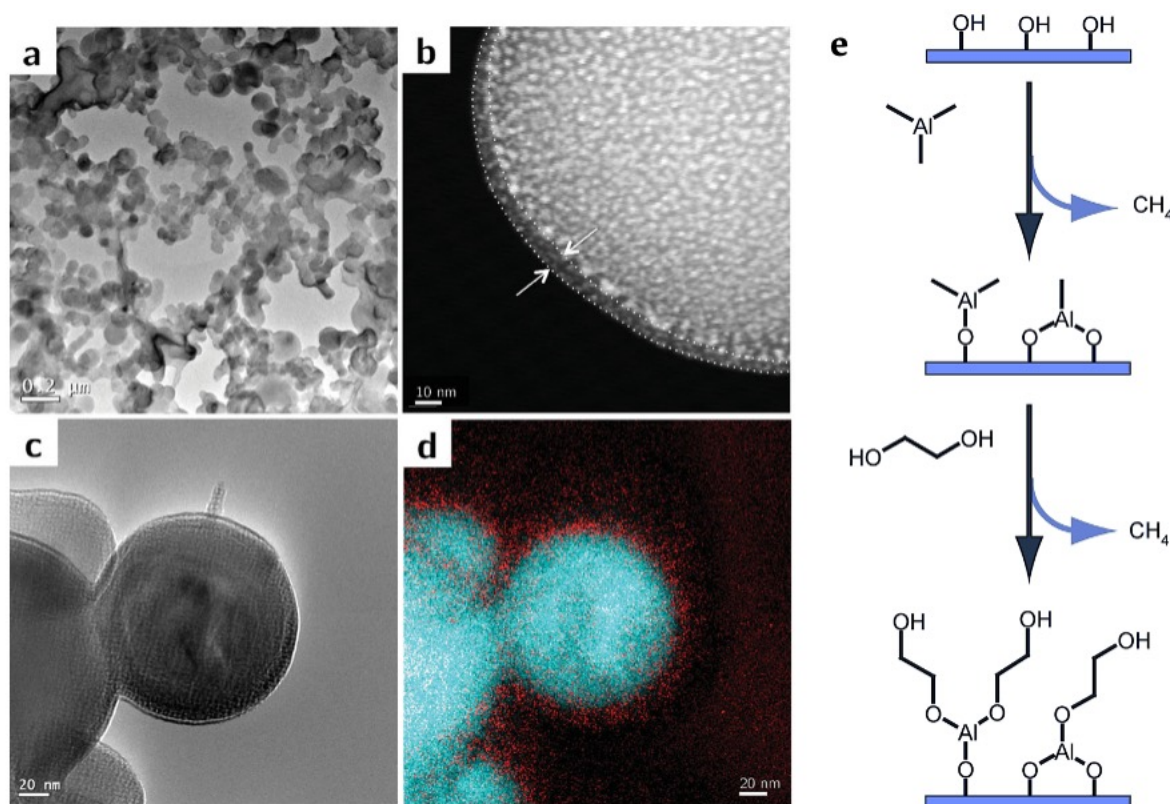


Figure 1.3: (a) TEM image of a nano-Si/AlGL (MLD alucone AlGL, deposited using TMA and GL as precursors) electrode showing a highly porous composite network. (b) HAADF-STEM image of a nano-Si particle coated with a ~5 nm thick dense and conformal layer of AlGL. (c) TEM image of a nano-Si/AlGL electrode. (d) EELS elemental mapping (Si: cyan; Al: red) of the structure in (c). (e) Schematic depicting the alucone (AIEG) MLD growth using the sequential exposures of trimethylaluminum (TMA) and ethylene glycol (EG).

The schematic of alucone (AIEG) MLD growth using sequential exposure to trimethylaluminum (TMA) and ethylene glycol (EG) as precursors is shown in figure 1.3,e. During the first half-cycle, the hydroxylated substrate is exposed to TMA which reacts with the available OH groups and CH₄ is released as a by-product. Once all surface functional groups have been consumed, TMA will no longer adsorb, which is key for ensuring the self-limiting nature of the process.

During the second half-cycle, EG vapor is introduced, which reacts with the immobilized TMA on the surface. This reaction leads to the restoring of surface hydroxyl groups, which is critical for enabling subsequent surface reactions with TMA in repeated cycles. CH₄ is again released as a product.

The growth rates of MLD films are often lower than expected, considering the calculated length of the molecular monomers. There are several possible reasons for such slower growth.

Organic molecules with long chains are flexible and prone to bend so that the growth is not perfectly perpendicular to the surface. In an extreme case, if they are homobifunctional, such molecules can bend to yield double reactions on the surface with their other end, thereby reducing the number of functional groups on the surface and lowering the growth rate with each deposition cycle. Another aspect is that organic precursors are often bulky, causing steric hindrance in MLD processes. Those and further issues that may occur upon using organic precursors are discussed in detail in a review article by George et al.¹² The most common strategies to improve the degree of control of the MLD growth process include the use of organic precursors with rigid backbones,²²⁻²⁴ heterobifunctional precursors,^{25,26} ring-opening reactions,²⁷ or using three different reagents instead of two.²⁸

The ratio $r = \text{growth rate} / \text{LM}$, where LM is the ideal length of the monomer (without bending, Figure 1.4 (left)), indicates a measure of ideal growth.²⁴

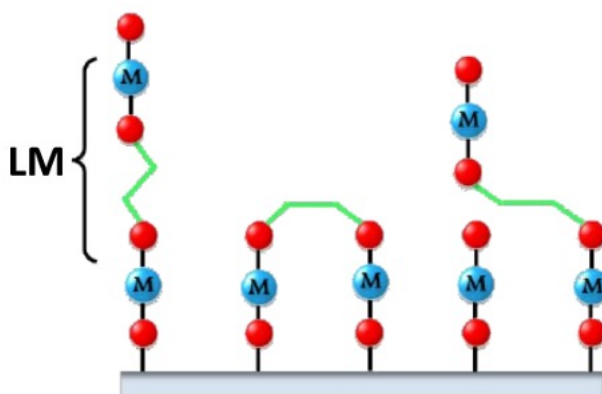


Figure 1.4: Ideally, an organic precursor molecule reacts with only one surficial functional group and remains straight (left). The molecule can also react with the surface with both of its ends (center) or bend (right).²⁴ LM is the ideal length of the monomer.

For the ideal case, $r = 1$. The achievable value of r depends mostly on different combinations of precursors. For purely organic MLD films, r is usually below 0.5. For hybrid ALD/MLD films, there is a greater spread of r values, depending on the used organic precursor. The choice of the metal precursor is also of great importance. For example, with a linear ethylene glycol molecule as an organic precursor and trimethylaluminum ($\text{Al}(\text{CH}_3)_3$), diethylzinc ($\text{Zn}(\text{C}_2\text{H}_5)_2$), titanium tetrachloride (TiCl_4) and zirconium tert-

butoxide ($\text{Zr}(\text{C}_4\text{H}_9\text{O})_4$) as inorganic precursors, the growth processes showed values of $r = 0.6, 0.1, 0.6,$ and $0.2,$ respectively.^{16,19,29}

1.2 Bioactive hybrid materials synthesized by ALD/MLD

Hybrid materials have been used for a wide range of biomedical applications, such as, tissue engineering, implant coatings with improved biocompatibility, antibacterial surfaces, targeted drug delivery systems, biosensors etc. Hybridized organic-inorganic systems are very attractive biomaterials since they show enhanced physical or chemical properties compared with their individual counterparts, while minimizing many of their specific limitations.

Various vacuum-based deposition techniques were applied to design hybrid bioactive or bioinert surfaces. However, ALD/MLD techniques have not yet been extensively applied in that field. The design of biocompatible and bioactive surfaces is an important development field for which MLD just started to provide solutions. Here, approaches where bioactive or bio-relevant organic molecules are used as precursors are most common and promising.

The development and characterization of bioactive MLD surfaces based on amino acids and nucleobases were first reported by the group of O. Nilsen. Among the scarce examples, a novel class of hybrid materials, containing essential amino acids combined with biocompatible titanium, called titaminates, were obtained by MLD.³⁰ The films were grown from titanium tetra-isopropoxide (TTIP) and glycine or L-aspartic acid as precursors. Hybrid films composed of TTIP and succinic acid were investigated for comparison with L-aspartic acid due to their structural similarities. FTIR and XPS analyses proved the hybrid nature of the grown materials and that the organic linkers preferably react with titanium through their carboxylic acid functional groups. The wettability of the hybrid films of glycine and L-aspartic acid was investigated by measuring the contact angle of water. The Ti-glycine and Ti-L-aspartic acid films showed hydrophilic nature with a contact angle of approximately 30° for films deposited at temperatures in the range of $225\text{--}350^\circ\text{C}$. The films were then used as substrates for the growth of epithelial cells (rat goblet cells), where their proliferation has been monitored. The cell proliferation on these substrates was significantly increased compared to uncoated coverslips. It was shown that epithelial cells can be successfully grown on such amino acid-based surfaces and that the cells retain a high viability.

Tailoring the surface functionality of materials is an important task in tissue engineering, specifically for designing bioactive and biocompatible materials. In the follow-up

work, Momtazi et al.³¹ further explored the MLD technique for building surface coatings consisting of bioactive compounds: amino acids, nucleobases, and the biocompatible metal titanium. The substrates were coated using TTIP and L-lysine, glycine, L-aspartic acid, L-arginine, thymine, uracil, or adenine as building units. Subsequently, immunofluorescence, cell attachment, proliferation, and viability of rat conjunctival epithelial goblet cells were analyzed. The results showed that amino acid, nucleobase-, and titanium oxide-coated substrates, prepared by MLD, do not reduce the cell attachment. The proliferation results indicated that proliferation of first-passage conjunctival goblet cells on Ti-L-lysine and TiO₂ was significantly higher than on uncoated coverslips. Cell growth studies on further substrates, containing different amino acids and nucleobases, were also performed.

Using immunofluorescence, primary cultures of rat conjunctival cells from one animal, grown on uncoated glass coverslips, demonstrated a goblet cell phenotype as indicated by the presence of cells positive for anti-CK7 and anti-MUC5AC antibodies, and the lectin UEA-1 (Figure 1.5 (a)). Thus, the cells in the primary culture were conjunctival goblet cells.

The viability of the cells was tested using the calcein acetoxymethyl/ethidium homodimer-1 live/dead assay. Figure 1.5 (b) shows a selection of fluorescence micrographs of the cells grown on the various coated substrates. The staining demarks the live rat conjunctival goblet cells as green and the dead cells as red, while the merged images show both. The results showed that the cell attachment on the MLD-coated substrates was at least as good as on coverslips. It was demonstrated that the MLD substrates increased the cell proliferation, except for MLD substrates containing terephthalic acid, which revealed a lower proliferation. Generally, the study showed that the cell viability was very high (>85%) for all substrates.

The same group³² also described in more detail the MLD-growth of organic-inorganic hybrid thin films by combining titanium tetra-isopropoxide (TTIP) and nucleobases, such as, thymine, uracil or adenine. The bonding modes of the films have been characterized by FTIR, XPS and X-ray diffraction, confirming the hybrid nature of the as-deposited films.

The wettability of the surfaces was investigated by measuring the contact angle of water on the various films. The films appeared to be highly hydrophilic with contact angle values of $19 \pm 2^\circ$ for Ti-thymine (deposited at 225 °C), $19 \pm 1^\circ$ for Ti-uracil (deposited at 225 °C), and $45 \pm 3^\circ$ for Ti-adenine (deposited at 250 °C). This hydrophilicity is an asset for the cell growth. Also, the effect of water on the film thickness upon exposure

was investigated. Most of the nucleobases leached out during the initial 15 minutes of immersion in water, but thereafter the thicknesses remained nearly constant over time.

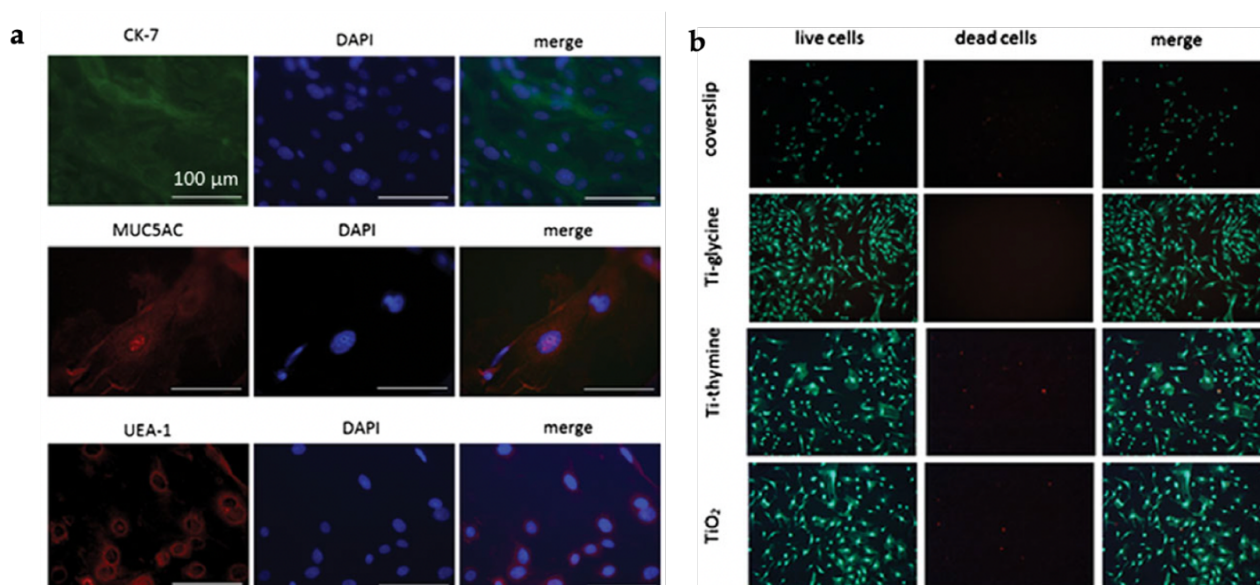


Figure 1.5: (a) Primary culture rat conjunctival goblet cells were grown for 7 days in RPMI 1640. The cells were then immunostained with anti-cytokeratin 7 (CK-7) (green; cyanine), mucin 5AC (MUC5AC) (red; indocarbocyanine), and Ulex europaeus agglutinin (UEA-1) (red; rhodamine). Nuclei were counterstained with DAPI (blue). Original magnification: $40\times$ (scale bar = $100\ \mu\text{m}$). Images are representative of samples from one animal. (b) First passage rat conjunctival goblet cells were cultured in RPMI 1640 on molecular layer deposition substrates, including Ti-glycine, Ti-thymine, and TiO_2 . Uncoated coverslips served as control. (A) After 5 days, viability was assessed using calcein acetoxymethyl/ethidium homodimer-1 live/dead assay. Micrographs show live (green), dead (red) cells, and merged live/dead images. Original magnification: $10\times$. Images are representative of nine and three samples for Ti-amino acid and Ti-nucleobase substrates, respectively (5 samples for Ti-L-arginine).³¹ Reprinted with permission from 23.

A series of recent studies has demonstrated that ALD/MLD can be used to fabricate biocompatible substrates via molecular design, which enables the use MLD within the field of regenerative medicine and tissue engineering for regulating cell and tissue development. Such biomaterials can be applied for implants where the surface functionality is a key factor for adhesion and interaction of the implant with the surrounding tissue.

Even though the work is not involving hybrid materials but purely inorganic materials, it is worth mentioning that Putkonen et al.³³ applied ALD to grow biocompatible hydroxyapatite (HA) thin films from $\text{Ca}(\text{thd})_2$ (thd = 2,2,6,6-tetramethyl-3,5-heptanedionato) and $(\text{CH}_3\text{O})_3\text{PO}$. The importance of this process lies in the fact that such materials

are very difficult to obtain from the gas phase and the proof of the growth by ALD allows for a precise tuning of the coating thickness, which is not possible in other ways. The biocompatibility of the substrates was demonstrated with cultures of Mouse MC 3T3-E1 cells. It was shown that, according to the bioactivity studies, the cell proliferation was enhanced on as-deposited ALD-grown Ca–P–O films and greatly enhanced on films annealed at 500 °C, in comparison with references grown on borosilicate glass or polystyrene, which is commonly used for cell cultures.

Puvvada et al.³⁴ examined the interactions of *E. coli* bacteria with ALD ZnO nanocoatings on cotton fabrics with systematically varying thicknesses between 0.2 and 20 nm. Woven cotton fabrics were conformally coated with ZnO films using ALD at 90 °C. They examined the bacterial growth on both treated and untreated cotton fabrics, fully immersed in aqueous dispersions of *E. coli* as well as drier test conditions. Under the dry test conditions, a stack of three treated cotton swatches, each 4.8 cm in diameter, were dampened with 1 mL bacterial solution for only 5 s. After the swatches were dampened, exposing the bacteria to the ALD ZnO coating, they were transferred to a sterile jar with 100 mL sterile (phosphate-buffered saline) PBS and then shaken for 1 min to collect the exposed bacteria. This solution was then sampled and plated on agar dishes, which then were incubated for 20 h, and the resultant colonies were counted. In fully aqueous conditions, a monotonic increase in the number of bacteria was observed for cotton fabrics coated with 1, 3, and 10 cycles of ZnO ALD. The samples coated with ten cycles showed that the bacterial growth increased by more than five times compared to the positive control. Coatings with fifty cycles (approximately 10 nm thickness) and beyond resulted in quantitative bacterial death. This may be related to the dissolution of ZnO. At low concentrations, Zn²⁺ ions function as nutrient, promoting the bacterial growth. In contrast, high concentrations of Zn²⁺ are cytotoxic for *E. coli*. Similarly enhanced bacterial growth was observed for up to 10 ALD cycles under pseudo-dry growth conditions. However, under such conditions, for 100 ALD cycle coatings (~20 nm), it required approximately 1 day to cause complete *E. coli* death.

The ability of ALD films to support cell attachment was also demonstrated by Liang et al.³⁵ They grew ultrathin conformal alumina and titania films on highly porous poly(styrene-divinylbenzene) (PS-DVB) particles applying low-temperature ALD processes in a fluidized bed reactor. The biocompatibility of the resulting composites was evaluated by HA formation and cell adhesion. The ability of the uncoated and coated porous particles to promote cell attachment and spreading was evaluated using a model cell, NIH/3T3 fibroblasts. The bioactivity studies of the composite particles were performed in vitro by immersion of the substrates into simulated body fluid (SBF) for various periods of time. The improved bioactivity of the polymer substrates was demonstrated with the formation of HA on the surface of the substrates from SBF. Indeed, an accelerated formation of HA on the ALD-modified polymer surface was observed, which

was likely caused by the negatively charged surface provided by the ultrathin ceramic interface.

Panchawagh et al. ³⁶ studied a flip-chip-based encapsulation process using surface micromachined polysilicon caps for packaging of MEMS actuators for BioMEMS applications. Aimed at protecting the MEMS structures from particulate matter present in biological liquids, the device was coated with alumina by ALD. Afterwards the Al₂O₃ coating was terminated with a covalently bound hydrophobic monolayer using a tridecafluoro-1,1,2,2-tetrahydro-octylmethylbis-(dimethylamino) silane (FOMB(DMA)S, C₈F₁₃H₄(CH₃)Si(N(CH₃)₂)₂) precursor. Such coatings may find their use in biomedical microelectromechanical systems and 'lab-on-a chip' microfluidic devices, including in vivo pressure sensors, implantable biochemical sensors, DNA sequencing chips, drug delivery systems, micro-assays, microelectrode arrays, microsurgical tools, and sensors.

More detailed information on this topic is provided here: Vapor Phase processing: A novel approach for fabricating functional hybrid materials. Ka. Ashurbekova, Kr. Ashurbekova, G. Botta, O. Yurkevich, M. Knez. *Nanotechnology* 31 (34), 342001.

1.2 Natural chitin and chitosan.

Bioinspired approach: why chitin?

Nature has created materials with properties and mechanisms that go far beyond the current man-made synthetic materials. Inspired by the remarkable characteristics of natural biological materials, scientists are trying to create materials with diverse new functionalities and composites to reproduce those properties by adapting principles similar to nature.

One of the goals of the present work was to design a surface with advanced functionality that can prevent bacterial adhesion, at the same time being biocompatible and nontoxic for the human body. In order to achieve that goal and design a material that would satisfy the above stated requirements, we used a bioinspired approach. In particular, we have tried to replicate the functionality of various types of naturally occurring, biocompatible, antibacterial and biodegradable substances.

Poly-(1→4)-β-D-N-acetylglucosamine is a good candidate for an antimicrobial coating and our material of choice, as this polymer has the demanded properties. When speaking about poly-(1→4)-β-D-N-acetylglucosamine, scientists refer to chitin, which

is a naturally occurring polysaccharide. Chitin is a linear polymer and the second most abundant natural biopolymer on Earth after another polysaccharide, cellulose. It is found in fungi, plankton, and the exoskeletons of insects and crustaceans.³⁷ Chitin is mechanically robust, nontoxic, and physiologically inert. It's inherent biocompatibility, biodegradability, bioactivity, wound healing, and intrinsic antibacterial properties made researchers introduce chitin and its derivatives into cosmetics, textiles, water treatment, tissue engineering, wound treatment, drug delivery,^{38,39} pharmaceuticals, catalysis,⁴⁰ or as component in biosensors.⁴¹ The physical coloration, typically originating from chitin-built hierarchical micro- and nanostructures in many insects, is often a source of inspiration for optical biomimetics.^{42,43}

Despite the demonstrated use of chitin and its water-soluble derivative chitosan in various industrial applications, their potential is much greater than presently perceived.

1.4 Synthesis and applications of chitin and chitosan

Chitin-based coatings are of enormous interest and are conventionally fabricated from solutions by spin-coating or other wet chemical processes through a series of synthetic multi-steps, which limits the flexibility of the material's final properties and use. Despite the variety of approaches, the large-scale fabrication of pure chitin is impaired by the difficulties in dissolution and regeneration of chitin. The lack of solubility of chitin in water and common organic solvents causes difficulties in improving its processability, fusibility, and functionality.

Solution-cast chitin films with thicknesses between 200 to 600 nm were fabricated from ionic liquids by several groups.^{44,45} Kikkawa et al. spin-coated a 50 nm chitin film from an ionic liquid onto silica, but the surface roughness of the film exceeded 20 nm.⁴⁶ Kittle et al. reported smoother chitin films (with roughnesses below 2 nm), formed by spin-coating gold or silica substrates with trimethylsilyl chitin and further exposing the substrate to the vapor of hydrochloric acid to regenerate the chitin.⁴⁷ However, unlike native chitin, the regenerated chitin films only showed amorphous chitin structures. Later, the same group reported on nanocrystalline chitin thin films obtained after spin-coating an aqueous colloidal chitin nanocrystal suspension onto a gold surface, previously modified by an amine-terminated self-assembled monolayer.⁴⁸ Duan et al.⁴⁹ demonstrated a complete dissolution of chitin in an aqueous solution of 11 wt.% NaOH and 4 wt.% urea and afterwards preparation of a pure regenerated chitin film from the

transparent chitin solution by coagulation with ethanol or 45 wt.% dimethylacetamide in water.

Despite the variety of approaches mentioned above, the fabrication of pure chitin remains being a challenge due to the difficulties in complex multistep dissolution and regeneration steps in the process. Furthermore, although there is large and growing interest in making a wide variety of materials and surfaces antimicrobial, and at the same time non-toxic to human body, the solubility of chitin is a major obstacle and the more complex the solvents are, the higher is the probability to trap impurities or solvents inside the chitin films, potentially negatively affecting the film stability or its properties. It is therefore desirable to avoid the use of solvents and additives as good as possible. The workaround is an adaptation of the chemistry to processing from the vapor phase.

The synthesis of such a polysaccharide, if it is aimed to be carried out from the gas phase, is very challenging. The low vapor pressure of the corresponding monomers and the thermal sensitivity of chitin/chitosan itself have so far made it unattainable for gas-phase syntheses. Reducing the process temperature was crucial, as materials such as the organic monomers (N-acetylglucosamine) and resulting polymers (chitin, chitosan) are temperature-sensitive and can easily decompose at conditions typically found in ALD/MLD processes.

We evaluated various approaches to create a reasonable working system that allows the fabrication of chitin-like layers using MLD. An elegant strategy for a controlled MLD growth of bioinspired chitin-analogues from the vapor phase was found to be the polymerization of the monosaccharide N-acetyl-D-mannosamine (ManNAc) upon layer-by-layer activation of the hydroxyl functionalities with thionyl chloride (SOCl₂). The thus grown chitin showed rather poor stability, therefore its integrity was improved by combining it with metal ions to obtain a completely new material composition, namely hybrid metallochitins. Inheriting the advantages of MLD with respect to uniformity, conformality, and controllability, the metallochitins showed exciting bioactivity, certainly being a good mimic of natural chitin.

The results of this work, including the established MLD toolbox introducing saccharides as precursors, and metallosaccharides as final products are presented in chapter 3 “Engineering of Biomimetic, Selectively Antibacterial and Biocompatible Metallochitin Films”.

1.5 Hybrid diffusion barriers by ALD/MLD

One of the further goals of the work project was to develop a process for the fabrication of ultrathin, flexible, bio-inorganic, and organic-inorganic hybrid surfaces as efficient

barriers for oxygen and water vapor permeation. The permeation barrier is important for enhancing the shelf life of packaged food. It minimized the exposure of food to oxygen or water vapor, which together with elevated temperatures are the main causes for food to spoil.

The most common materials used as permeation barriers are inorganic oxides and nitrides, such as SiO_2 , silicon nitrides (SiN_x), TiO_2 , or Al_2O_3 . However, pure inorganic materials typically have detrimental weaknesses, such as brittleness and pinhole defects. Moreover, thin film barriers consisting of single layers usually show high water vapor transmission rates (WVTR) due to defects in the films caused by the deposition processes or cracks caused by stress in the brittle films, especially when increasing the film thickness.

The incorporation of organic layers by MLD could prolong the diffusion pathways of the permeator molecules and reduce the stress in the thin film by adding a certain level of flexibility to the coating. For instance, an ultra-water vapor proof polymer hybrid with a $\text{WVTR} < 10^{-7} \text{ g/m}^2 \text{ day}$ can be achieved by filling the free volume of the polymer with Al_2O_3 via gas-phase infiltration by atomic layer deposition (ALD).

The requirements for an optimal thin film barrier can be summarized as follows:

- Low deposition temperatures to enable coating of polymers
- High uniformity
- High density of the thin film
- Amorphous structure to avoid diffusion along grain boundaries
- Defect and pinhole free
- Stress free
- High flexibility
- High transparency (for optical applications)

MLD is the method-of-choice to fulfill these requirements, as it allows for the deposition of a wide variety of materials, many of which exhibit the above-mentioned requirements.

Organic-inorganic hybrid materials are proven to be efficient for encapsulation. Besides MLD, vapor phase infiltration (VPI), also known as sequential vapor infiltration (SVI) or sequential infiltration synthesis (SIS), are other approaches to produce hybrid materials from the gas phase. VPI is based on similar principles and chemistries as ALD and MLD, and it allows not only the precise thin film deposition but also modification of the near-surface of soft materials. As polymers contain long chains and free volume throughout the material, filling this empty space can significantly improve the barrier

properties of the polymer. Lynn Lee et al. showed that applying only 50 SVI cycles of Al_2O_3 to polyimide substrates allowed to achieve the WVTR values below the detection limit of a Ca corrosion test ($<10^{-7} \text{ gm}^{-2} \text{ day}^{-1}$).⁵⁰ In a recent work, this approach was extended to Al_2O_3 -polyethylene terephthalate (PET), Al_2O_3 -polyimide, and Al_2O_3 -Nylon 6 organic-inorganic hybrids.⁵¹ The authors performed Ca-tests even on stretched hybrids and the WVTR values remained as low as $<10^{-7} \text{ gm}^{-2} \text{ day}^{-1}$.⁵⁰ The outstanding nanoscale thickness of the complete polymer-alumina hybrids makes SVI aka. VPI a very promising method for sealing foldable, stretchable, and flexible devices.

A literature review shows that pure hybrid MLD materials were also tested as barrier layers but show poor barrier performance when they are applied individually. Because of this, flexible hybrid gas permeation barriers were grown by ALD/MLD using a large variety of organic and inorganic precursors. The MLD alucone layer could potentially decouple defects and improve the mechanical properties of the coating by reducing the internal stress of inorganic films. Therefore, barriers consisting of inorganic - organic multilayers were widely used when high barrier performance was required.

Here, some recent reports on the studies, where the two techniques were combined to obtain hybrid inorganic/organic multilayers in the same vacuum chamber, are described:

Nanolaminate films grown by varying the number of Al_2O_3 ALD and alucone MLD cycles, deposited on Kapton polyimide substrates, were reported by Jen et. al.⁵² The WVTRs were measured for the Al_2O_3 ALD, alucone MLD, and nanolaminate films grown using Al_2O_3 ALD:Alucone MLD cycle ratios varying from 1:1 to 6:1. The results show that excellent diffusion barrier properties can be achieved with nanolaminate films and that the laminates are more flexible than pure Al_2O_3 ALD films.

Chen et. al studied Al_2O_3 /alucone nanolaminates with a maximum thickness of 102.5 nm, fabricated by ALD/MLD at a low temperature.⁵³ It was found that alucone could limit the permeation of the inorganic layer by prolonging the permeation pathway, thereby sequentially improving the moisture barrier performance. The WVTR could be further lowered with increasing the number of dyads of the laminates. The WVTR value reached $10^{-4} \text{ g/m}^2/\text{day}$ for laminates with 5.5 dyads.

Thin encapsulation layers, various nanolaminate structures consisting of $\text{Al}_2\text{O}_3/\text{ZrO}_2$ /alucone, were reported for an encapsulation of organic light-emitting diodes (OLEDs).⁵⁴ The moisture barrier performance was improved with increasing the number of dyads ($\text{Al}_2\text{O}_3/\text{ZrO}_2$ /alucone). The WVTR reached $8.5 \times 10^{-5} \text{ g/m}^2/\text{day}$ at 25°C and a relative humidity (RH) of 85%.

Usually, diffusion barrier coatings are needed on polymers such as polyethylene terephthalate (PET) or polyethylene naphthalate (PEN), which are used for packaging of degradable goods such as food, beverages, or pharmaceuticals. Furthermore, OLEDs need to be protected from moisture and air to avoid degradation. For a long-life of

OLEDs, extremely efficient gas barrier layers must be used that are ideally also flexible. To be efficient, a high activation energy for the permeation and a sufficiently high flexibility of the coating is needed to obtain an ultralow WVTR. For OLEDs, for example, the WVTR should be at least $10^{-6} \text{ g m}^{-2} \text{ day}^{-1}$ to ensure a device working for $>10000\text{h}$.

For the present work, we chose to develop processes by combining vapor phase infiltration (VPI), molecular layer deposition (MLD) and atomic layer deposition (ALD) techniques. Specifically, the development of a new process for a modified polymeric substrate with a hybrid bio-functional top layer, which is suitable as packaging material for a range of applications, from food packaging to encapsulation of OLEDs and solar cells, is of interest. To be suitable as encapsulating layer, the MLD process should provide pinhole-free, ultrathin, transparent and flexible films with unique mechanical properties such as flexibility, stretchability, and reduced brittleness. For the food packaging applications, the anti-bacterial functionality is of additional importance. Therefore, our idea was to generate a functional coating that would provide a combination of characteristics, such as, biocompatibility or bactericidity/fungicidity, chemical stability, mechanical stability, while at the same time being low in cost.

One of the options to solve this problem is a bottom-up approach, which includes the synthesis of an MLD film with suitable functionalities on top of polymeric substrates.

We modified commercially available polymeric packaging materials like cellophane, and polyethylene naphthalate (PEN) with alumochitin and titanochitin MLD films. Besides, the siloxane-alumina hybrid organic-inorganic thin films, deposited using tetramethyl-tetravinylcyclotetrasiloxane (V_4D_4) and trimethylaluminum (TMA) on PEN, were fabricated. The barrier properties of the obtained samples on different substrates were assessed in the framework of a collaboration with TNO, Eindhoven, The Netherlands.

1.6 Objective and structure of the thesis

This thesis aims to explore the potential of MLD for the synthesis of multifunctional hybrid organic-inorganic materials. Multifunctional surfaces with improved biocompatibility, that simultaneously prevent bacterial contamination and biofilm formation, are a great challenge in the current research on biomaterials.

We developed several processes to synthesize such bioactive hybrid films through MLD. The results obtained in this work have considerably broadened the range of materials that can be fabricated by MLD.

Chapter 2 overviews the experimental techniques and methods used in this thesis for the chemical and physical characterization of the samples.

The work presented in Chapter 3 shows our pioneering work on growing conformal ultrathin functional films of chitin-based hybrid biomaterials, which we term metallochitins or, more generally, metallosaccharides.

We have developed a series of bioactive coatings by fusion of sugar-type molecular precursors with metalorganic compounds through MLD. The growth and characterization for both, purely organic chitinoid and hybrid organic–inorganic alumochitin and titanochitin thin films, have been demonstrated. A variety of experimental (FTIR, QCM, XPS, XRR, TEM, EELS, EDX) and theoretical (DFT) studies were performed to confirm the metallochitin film growth and characterize their composition and structure. The antibacterial properties of the obtained chitinoids and hybrid metallochitins were studied with the binding behavior of both Gram-negative and Gram-positive bacteria *in vitro*. The biocompatibility of the alumochitin and titanochitin films was investigated with the proliferative behaviors of Human Embryonic Kidney HEK293T and Fibroblast cells *in vitro*. The results demonstrate that the developed hybrid metallochitins function as versatile biomaterial, being an excellent mimic of natural chitin, stimulating the cell growth and proliferation while simultaneously preventing the adhesion of bacteria, even selectively for gram-positive or gram-negative strains.

Chapter 4 describes the MLD growth of ultrathin and biocompatible hybrid materials that meet the requirements for the development of stable and biocompatible surfaces. We developed a new and facile MLD process to grow hybrid organic–inorganic aluminosilazane films, making use of ring opening reactions of 2,4,6-trimethyl-2,4,6-trivinylcyclotrisilazane (V_3N_3) and coupling the molecules to TMA. The developed simple and solvent-free MLD process allows to grow environmentally sustainable aluminosilazane hybrid thin films with exceptionally good biocompatibility.

Chapter 5 is devoted to the synthesis of oxazoline–based polymers from the gas phase. So far, polyoxazolines have only been prepared by solution-based chemistry. We show for the first time a Living Polymerization from the gas phase, the deposition of polyoxazolines by using Tosyl Chloride (4-Toluenesulfonyl chloride) and oxazolines.

Polyoxazolines of various chemical functionalities were prepared in a living, and, therefore, controlled manner via cationic ring-opening polymerization. *In-situ* QCM, ATR-FTIR, XPS and Thermogravimetric (TGA) analysis were performed to study the composition and reaction mechanism for the formation of the polymers. Such materials

are of interest for many biological and biomedical applications, including drug and gene delivery.

Finally, a summary of the research and future perspectives are given in Chapter 6.

Chapter 2

Experimental techniques and methods

This chapter provides an overview of the experimental techniques used in the thesis. In general, experimental methods such as FTIR, XPS, Thermogravimetric analysis (TGA), TEM and EDX have been used to study the composition, bonding environment and structure of the materials and films. QCM and XRR measurements were performed to characterize the growth of the developed MLD systems, respectively.

Details on some specific methods, such as in vitro antibacterial and biocompatibility testing, depending on the types of bacteria and cells used, are described in the relevant sections. The chapter concludes with data on the precursors and substrates used in this work.

2.1 Laboratory setup for Atomic and Molecular Layer Deposition

Deposition of the films was performed in a commercial ALD reactor (Savannah S100, Cambridge NanoTech Inc).

To analyze the growth profile of the synthesized film, quartz crystal microbalance (QCM) measurements were performed in-situ in the custom-built viscous flow hot-wall ALD reactor, schematically shown in Figure 2.1.

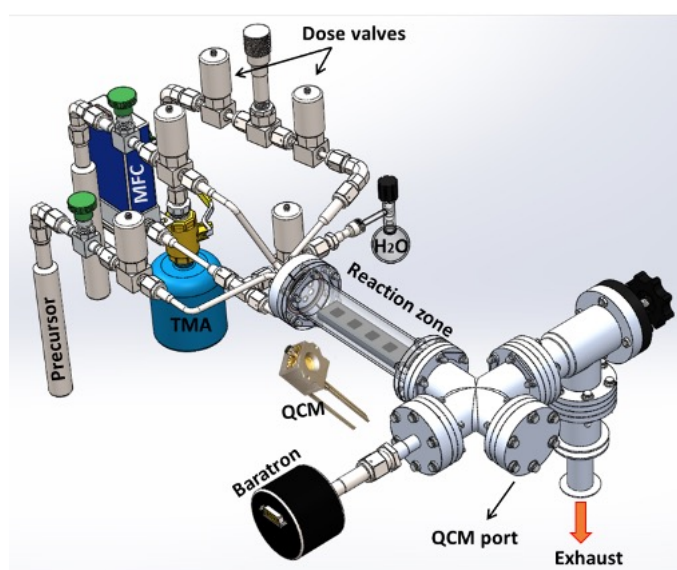


Figure 2.1: Schematic of a vacuum reactor for thin films deposition by ALD/MLD.

The dense flow of inert gas, supplying the reaction zone, is controlled by a digital mass flow controller (MFC, supplied by the company MKS). Ultrahigh purity nitrogen (99.999%) was used as carrier gas for the precursors. The nitrogen pressure in the reactor chamber was maintained at 0.9 Torr (~ 120 Pa) with a nitrogen flow of 150 standard cubic centimeter per minute (sccm) and is variable with the MFC by changing the carrier gas flow. The machine is equipped with four dosing lines for the precursors that consist of a steel cylinder (Swagelok), a metering valve (Swagelok) and a pneumatic high-speed valve (Swagelok). The pressure in the system is monitored with a high-precision digital baratron vacuum gauge (MKS), which allows to detect pressures of 1 - 10 Torr at high temperatures (up to 150 °C). This baratron gauge has a metal membrane which deforms upon pressure changes, changing the distance between the closely spaced electrodes of a capacitor, which consequently alters the capacitance as a function of the pressure change. This condition makes it possible to detect even the smallest changes in pressure. Evacuation of the system is achieved with a rotary vane vacuum pump.

The baseline pressure of 1 Torr in the reactor chamber was maintained to provide a viscous gas flow. To determine the type of gas flow, the so-called Knudsen number (Kn) is used for diluted gases, which is defined as the ratio of the molecular mean free path length λ (m) to a representative physical length scale (relates to a gap length over which thermal transport or mass transport occurs through a gas phase).

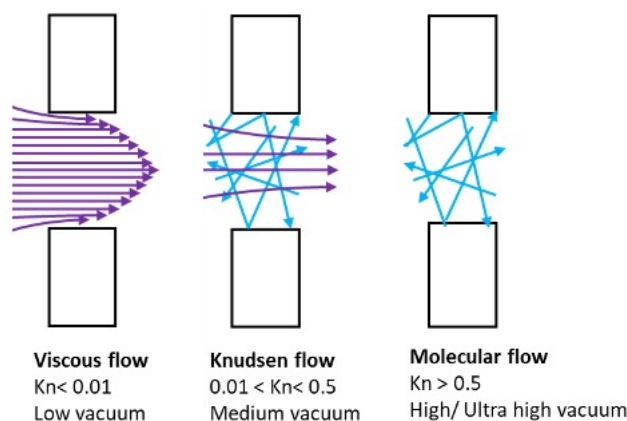


Figure 2.2: Schematic of different types of flow regimes.

Figure 2.2 schematically shows the different types of flow. In viscous (continuous) flow, when the Knudsen number is <0.01 , the collisions between gas molecules happen more frequently than with the chamber walls. In this case the mean free path of the gas molecules is significantly shorter than the dimensions of the flow channel (that is, the internal diameter of the reactor tube in the case of our ALD reactor). In case of molecular flow, that is, when Knudsen number is above 0.5, molecular interaction virtually no longer occurs, and thus the molecules basically collide only with the walls.⁵⁵ In this case, the mean free path is significantly greater than the diameter of the flow channel.

For the ALD/MLD process it is important to stay in the viscous flow regime, where the precursor molecules have a short mean free path providing sufficient chemisorption to fulfill the criteria of the formation of a complete monolayer (in the idealized case) in the reaction zone. Therefore, the Knudsen number is of importance and will be estimated for our home-made reactor.

The mean free path is highly dependent on pressure, while molecular sizes and process temperatures have negligible effect. The mean free path of molecules (λ) for our system can be calculated with equation 1 and accordingly equals to:

$$\lambda = \frac{RT}{\sqrt{2}\pi d^2 N_A P} = \frac{K_B T}{\sqrt{2}\pi d^2 P} = \frac{1.38 * 10^{-23} * 383}{\sqrt{2} * 3.14 * (3.63 * 10^{-10})^2 * 120} = 7.53 * 10^{-5} \text{ m}$$

where K_b is the Boltzmann constant ($1.380649 \times 10^{-23} \text{ J}\cdot\text{K}^{-1}$), T is the temperature of the ALD/MLD process, equal to 383 K (110 °C), d is the average diameter of nitrogen molecules ($363 \text{ pm} - 3.63 \times 10^{-10} \text{ m}$) and P is the pressure ($120 \text{ Pa} = 0.9 \text{ Torr}$). The diameter of the tube (d_t) used as the reaction zone is 3.8 cm.

$$\text{Kn} = \frac{\lambda}{d_t} = \frac{7.53 * 10^{-5}}{0.038} = 1.98 * 10^{-3}$$

Thus, the value $\text{Kn} < 0.01$, which confirms that our reactor operates is in a viscous flow regime.

2.2 In-situ quartz crystal microbalance (QCM)

The deposition process was monitored in-situ with a quartz crystal microbalance (QCM), using an SQM-160 Thin Film Deposition Monitor with a resolution of $\pm 0.31 \text{ ng/cm}^2$ and an AT-cut crystal with the resonant frequency of 6 MHz.

The QCM technique was introduced by Sauerbrey⁵⁶ and is based on the piezoelectric properties of quartz. It is used to control mass changes during film growth, sorption, and other surface studies in gas, as well as in liquid media.⁵⁷ The very high sensitivity of the QCM, which is usually below $1 \mu\text{g}$, is a key advantage of this method. Some QCM tools reach resolutions as good as 0.05 ng.

The sensor in the QCM is an AT-cut ($35^\circ 25'$ to the Z axis) quartz disk with gold electrodes on both sides. When a potential difference is applied to the electrodes of a quartz crystal, an inverse piezoelectric effect occurs under the influence of an electromagnetic field. As a result, the surfaces of the gold plates are shifted relative to each other, and a resonant oscillation occurs. During surface reactions on the crystal, in our case during the ALD process, the resonant frequency changes in accordance with the Sauerbrey equation:

$$\Delta f = \frac{-2f_0^2 \Delta m}{A\sqrt{\mu\rho}} = -C\Delta m$$

where Δf is the change in the resonant frequency of the quartz crystal (Hz), f_0 is the resonant frequency of the quartz resonator, Δm is the mass change, A is the

piezoelectrically active area defined by the two active electrodes, μ is the shear modulus of the AT-cut quartz crystal ($\sim 2.947 \times 10^{11}$ dyne/cm²) and ρ is the quartz density ~ 2.648 g/cm³. Depending on the parameters, μ and ρ , the coefficient C for different QCM sensors will differ.⁵⁸ Using this frequency versus mass dependence allows detecting mass changes up to 10^{-12} kg (pg) (for crystals with frequencies up to 15 MHz), which exceeds the sensitivity limit of any currently used laboratory balance.

The schematic of the QCM tool in an electrical circuit can be represented as an equivalent electrical circuit shown in Figure 2.3.

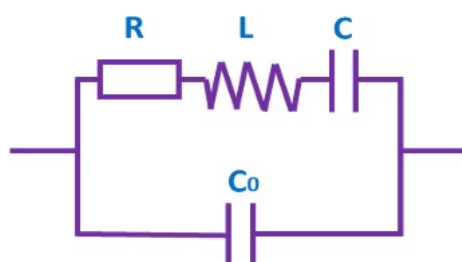


Figure 2.3: Equivalent electrical circuit representing the QCM.

Each element in the circuit represents a certain feature of the crystal. "R" is the resistance loss of the mechanical oscillatory system - the viscosity of the medium, internal friction, damping by the holders, "L" is the inductance of the oscillatory system of the resonator, which depends on the mass of the adsorbed substance, "C" is the capacitance of the mechanical oscillatory system of the resonator, "Co" - the intrinsic capacitance of the crystal that occurs between the electrodes on the crystal and the parasitic capacitance of the crystal.

Given the operation with very small mass amounts, QCM is an indispensable tool in ALD that allows to experimentally find many process parameters, including mass gain during precursor pulsing, optimal precursor saturation time, purge time, temperature dependence of the growth rate, nucleation period, adsorption dynamics of precursors, etc.

2.3 X-ray photoelectron spectroscopy (XPS)

X-ray photoelectron spectroscopy is based on the phenomenon of the photoelectric effect that occurs when using monochromatic X-rays (Figure 2.4). It allows to determine the energies of internal electronic levels based on the measured kinetic energies (KE) of emitted photoelectrons. Schematically, the photoelectron emission process is represented by the Einstein equation used to describe the photoelectron process:

$$h\nu = BE_0 + KE$$

where $h\nu$ is the energy of an X-ray quantum, BE_0 is the binding energy of an electron relative to the vacuum level, KE is the kinetic energy of a photoelectron. Here, the vacuum level is taken as the zero level of the energy scale.

The BE_0 of an electron is defined as the energy required to remove the considered electron to infinity with zero kinetic energy, and is equal to the difference between the total energies of the considered system in the final and initial states:

$$BE_0 = E^{\text{Final}} - E^{\text{initial}}$$

where E^{Initial} is the total initial energy of an atom, molecule or solid, and E^{Final} is the total energy of the system in the final state after electron emission. Thus, the KE of the emitted photoelectron is determined by the BE_0 values of the corresponding atomic levels, which are unique for each element and are determined by the Coulomb interaction of an electron of a given atomic level with other electrons and by the attractive potential of the nucleus.

Consequently, XPS allows elemental analysis of materials, but the exact value of the binding energy of an electron in the ground state in an atom also depends on its chemical environment. The energy of an electron in the inner shell is determined by Coulomb interactions with other electrons and by the attractive potential of the nucleus. Any change in the chemical environment of an element will affect the spatial distribution of the charge of the valence electrons of that atom and cause a potential change perceptible to the inner electron.

The charge redistribution affects the potential of inner electrons and leads to a change in their binding energy, that is, to the so-called chemical shift. This chemical shift process in electronic spectra is one of the main advantages of XPS over other methods for determining the elemental composition of solids.

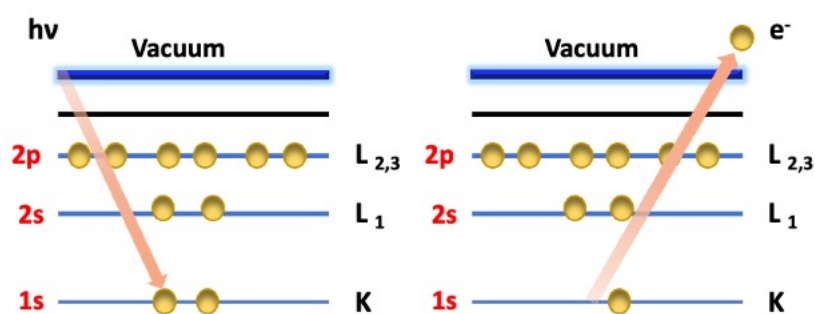


Figure 2.4: Scheme of the photoelectron emission process.

Based on the above, the main advantages of the XPS technique for analysis of thin films and interfaces formed by the ALD method are:

1. Small depth of analysis ~ 5 nm.
2. Possibility of performing elemental analysis.
3. Possibility of determining the chemical state of elements.
4. Possibility to study the electronic structure of thin films and interfaces.
5. Non-destructive research technique.
6. Possibility of obtaining information about the elemental, chemical composition, and electronic structure of the depth of the sample by measuring the angular dependence of the output of photoelectrons.

The last point is of particular importance in the analysis of nanometer layers, since it makes it possible to nondestructively obtain depth profiles of the distribution of elements, chemical and electronic states in thin films.

2.4 Fourier transform infrared spectroscopy – attenuated total reflectance (FTIR–ATR)

Attenuated total internal reflectance Fourier IR (ATR-FTIR) spectroscopy was used to obtain information about the chemical structure of the materials in the resulting films. ATR-FTIR analysis was performed using a PerkinElmer Frontier spectrometer. The spectra were recorded in the range from 600 to 4000 cm^{-1} after 20 scans with a resolution of 4 cm^{-1} . The substrates for ATR-FTIR measurements were made by pressing ZrO_2 nanoparticles into pellets and using those as high surface area substrates (due to their

high porosity) for increasing the amount of deposited materials and in this way increasing the signal-to-noise ratio.

ATR-FTIR spectroscopy is based on the phenomena that occur when an IR beam is reflected at the interface between two media with different optical densities. Figure 2.5 shows a cell for ATR FTIR spectroscopy.

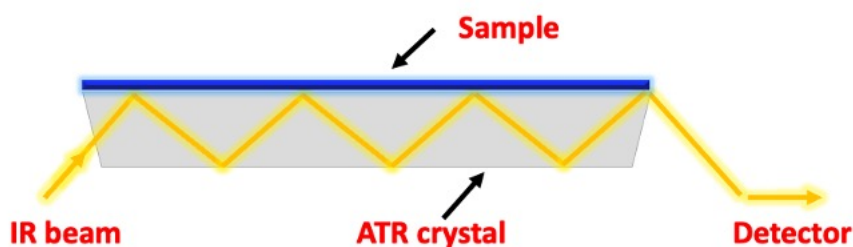


Figure 2.5: A cell for ATR FTIR spectroscopy.

For ATR-FTIR total internal reflections of the IR beam inside an ATR crystal are used. The IR beam is coupled into and passes through an optically dense crystal with a high refractive index at a certain angle. Between coupling in and out, the IR beam hits the interface of the ATR crystal and the sample positions atop one or multiple times. Due to the differences in the refractive indices of both materials, total internal reflection occurs, but the damped radiation wave (evanescent wave) still penetrates the bulk of the sample to a depth of about one micrometer. In the IR region of the spectrum, where the sample absorbs energy, the evanescent wave will be attenuated. The attenuated IR beam is recorded by the detector of the spectrometer and used to generate an IR spectrum.

2.5 X-ray Reflectivity (XRR)

X-ray reflectometry was used to determine the thickness, density, and roughness of films on silicon substrates. The measurements were carried out with a PANalytical X'Pert Pro diffractometer using a Cu K α X-ray source. To simulate the density and roughness of the films, we used the X'Pert Reflectivity program with a given structure: Si/SiO₂/ALD-MLD layer. The error bars obtained for the ALD/MLD films on silicon substrates represent the data obtained from three samples positioned at different positions of the reactor in the same experiment.

The X-ray reflectivity technique is based on the phenomenon of total external reflection of an X-ray beam from a flat sample surface and subsequent measurement of the radiation intensity. X-ray reflection is measured within the critical angle. For total external reflection below the critical angle, the penetration depth of the X-ray beam into the film thickness is only few nm. As the angle increases, the penetration depth of the beam increases. At each interface, at which the electron density changes, a part of the X-rays is reflected, the interference of which creates oscillations in the experimental curves. Based on the obtained curves, the parameters of the layers, such as thickness, density, and roughness, are determined by modeling.

2.6 High resolution transmission electron microscopy (HRTEM) and X-ray energy dispersive spectrometry (EDXS) in TEM

High-resolution transmission electron microscopy (HRTEM) and scanning transmission electron microscopy (STEM) were used to study the structure, homogeneity, and conformity of the resulting coatings. TEM and STEM were carried out on an FEI Titan 60-300 microscope (Thermo Fisher). To study their morphology, the films were deposited on zirconium dioxide nanoparticles for better visualization and for avoiding the necessity of preparation of cross-sections. The microscope was operated in the monochromatic mode at an accelerating voltage of 80 kV. Energy dispersive X-ray spectrometry (EDXS) in TEM was used to perform elemental mapping (EDAX Octane, AMETEC) and was carried out at an accelerating voltage of 300 kV.

2.7 Thermogravimetry (TG) analysis

Thermogravimetry (TG) is a method of thermal analysis in which the change in the mass of a sample is recorded as a function of the temperature. The obtained results allow to examine the thermal stability of the sample at various stages of the process.

The technique is effective provided that the sample emits volatile substances as a result of ongoing physical or chemical processes during thermal treatment. The thermogravimetry device consists of thermobalances, which continuously measure the mass of the sample, while the sample is heated or cooled. The basic operation while performing TG is as follows: the sample is placed in a crucible (Figure 2.6) resting on the balance. The crucible is then heated in an electric furnace so that its temperature rises linearly. The furnace temperature is measured using a thermocouple located inside, and the mass of the sample is recorded with a certain preset step.

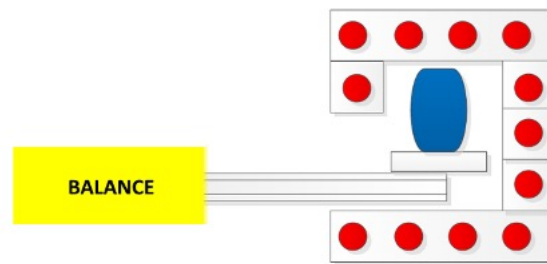


Figure 2.6: Scheme of a setup for performing TG analysis.

The resulting form of the TG curve allows to judge the thermal stability or instability of the sample, gives an information about the formation of intermediate decomposition products, as well as about the chemistry and kinetics of thermal reactions by stages of the process.

2.8 Experimental setup for Water Vapor

Transmission Rate (WVTR) measurements

There are several approaches to measure WVTR values. In our research, we used a GINTRONIC Easyperm 650 tester at the collaborator's site at TNO, Netherlands (Figure 2.7). The measurement system conforms to ISO 15106-1 and ASTM E398-03 standards and can be used for measuring WVTRs down to 10^{-2} g/(m²day). Higher sensitivity measurements require Ca-tests or the optical gas-sensing method.

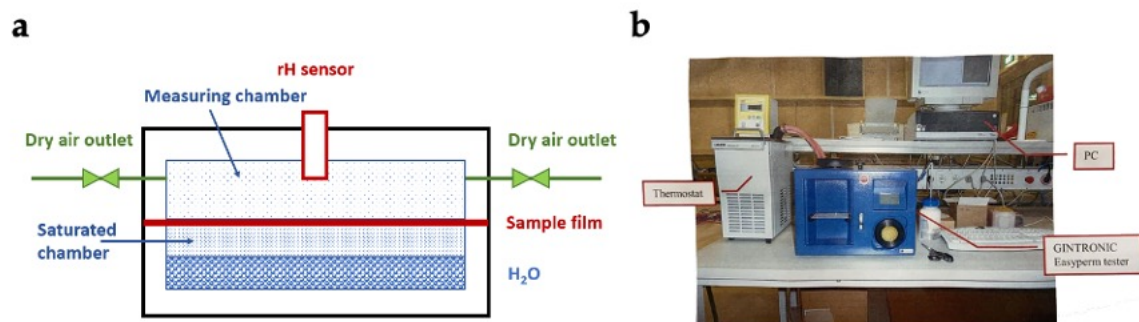


Figure 2.7: (a) Schematic representation of the measurement system. (b) Experimental set-up.

The Gintronic system consists of two chambers separated by a sample (Figure 2.7) for a schematic representation). The lower chamber is filled with water, which creates an atmosphere saturated with water vapor.

The temperature of the water is controlled and set to 38 °C. The measurement chamber is dried to a pre-determined relative humidity value RH1. When this humidity value is reached, the inlet and outlet valves are closed, thus allowing the moisture to permeate through the sample film and accumulate in the measuring chamber.

A humidity increase in the measuring chamber is detected with a RH sensor. When the predetermined threshold of 90 % RH is reached, the measurement is stopped, and the time required to obtain this RH value is recorded. This value of the time is then compared with the reference and the WVTR values are calculated.

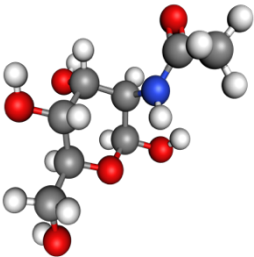
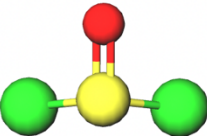
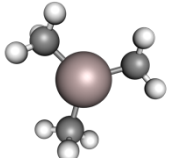
2.9 Precursors and substrates

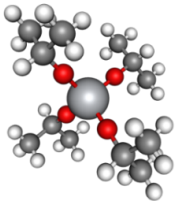
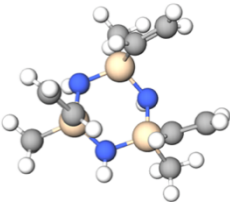
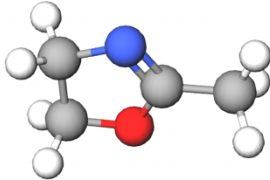
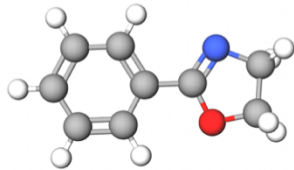
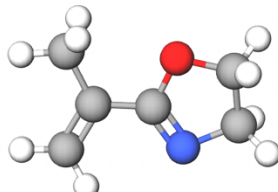
For the ALD process, the choice of precursors is important as those need to fulfil certain requirements. A precursor should be evaporating or subliming at a temperature below the reaction temperature in the ALD chamber, which is necessary to ensure the temperature gradient from the precursor source to the exhaust line. This is important to avoid and condensation of the precursor due to cold spots, as this would result in undesired parasitic CVD deposition. The by-product of the ALD reaction must be volatile and shall not disturb the ALD growth. Furthermore, the precursor should be stable and

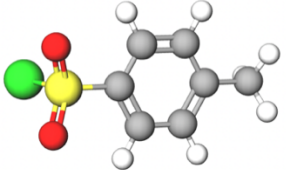
must not thermally decompose at the evaporation temperature or during the deposition process.

The main characteristics of the precursors (heating temperature, vapor pressure, and aggregation state at normal conditions (n.c.)) used for the synthesis of thin films by the ALD/MLD methods in this thesis are summarized in Table 1.

Table 1: Precursors used for MLD processes.

Chemical name and structure	T _{heating} [°C]	Vapor pressure at n.c. [torr]	State at n.c.
N-Acetyl-d-mannosamine (ManNAc) (min. 98% pure, Biosynth Carbosynth) 	100	< 0.1	Solid powder
Thionyl chloride (97% pure, abcr) 	25	97	Fuming liquid
Trimethylaluminum TMA (97% pure, Sigma-Aldrich) 	25	12	Flammable liquid (on air)

<p>Titanium (IV) isopropoxide (TTIP) (97% pure, Sigma-Aldrich)</p> 	70	0.1	Fuming liquid
<p>2,4,6-trimethyl-2,4,6-trivinylcyclotrisilazane (V_3N_3), ($\geq 90\%$ pure, Sigma-Aldrich)</p> 	80	0.5	Colorless liquid
<p>2-Methyl-2-oxazoline ($\geq 98\%$ pure, Sigma-Aldrich)</p> 	50	1	Highly flammable liquid
<p>2-Phenyl-2-oxazoline, (99% pure, Sigma-Aldrich)</p> 	50	< 0.1	Liquid
<p>2-Isopropenyl-2-oxazoline, (98% pure, Sigma-Aldrich)</p> 	25	22	Flammable liquid

<p>P-Toluenesulfonyl chloride, (99% pure, Sigma-Aldrich)</p> 	95	< 0.1	White to gray powdered solid
--	----	-------	------------------------------

High purity nitrogen (99.9999%) was used as the carrier gas for the MLD processes.

The substrates used in this work for different characterization techniques are summarized in Table 2.

Table 2: Substrates used for the growth of MLD films

Substrate	Substrate size	Methods for Studying
Polished quartz AT-cut QCM crystal coated with ALD Al ₂ O ₃	Diameter 14 mm	QCM
Si wafers with a native 2-3 nm thick SiO ₂ layer	1×1 cm	XPS, XRR
ZrO ₂ nanoparticles(Sigma-Aldrich)	diameter 30-40 nm	ATR-FTIR, TEM
ZnO nanoparticles(Sigma-Aldrich)	diameter <100 nm	XPS
Glass coverslips	2×2 cm	Biotesting for bacteria and cell culturing
Cellophane Uncoated cellulose sheets Polyethylene naphthalate (PEN) Polyethylene terephthalate (PET)	Specific sizes	Substrates for barrier performance tests

Chapter 3

Engineering of Biomimetic, Selectively Antibacterial and Biocompatible Metallochitin Films

The progress of our civilization and well-being of humankind entails the perpetual development of sophisticated functional materials. Multifunctional surfaces with improved biocompatibility that simultaneously prevent bacterial contamination and biofilm formation are a great challenge and a major arena of the current research on biomaterials. The present work provides the first solid foundation for growing conformal ultrathin functional films of chitin-based hybrid biomaterials, which we term metallochitins or, more generally, metallosaccharides. Inspired by the properties of natural chitin, we have developed a series of bioactive coatings by fusion of sugar-type molecular precursors with metalorganic compounds through Molecular Layer Deposition (MLD). A variety of experimental (FTIR, QCM, XPS, XRR, TEM, EELS, EDX) and theoretical (DFT) studies were performed to confirm the metallochitin film growth and characterize their composition and structure. The mild process temperature and solvent-free nature of the MLD process enables the growth of conformal hybrid layers on a variety of substrates, regardless of the complexity in topology or presence of high-aspect-ratio features. Our *in vitro* tests have confirmed that from the bioactivity prospect the metallosaccharides are an excellent analogue of natural chitin, stimulating cell growth and proliferation, while simultaneously preventing the adhesion of Gram-negative and Gram-positive bacteria. Metalation of the chitin film with aluminum and titanium increases the chemical and mechanical stability of the organic material. This generates new opportunities for tailoring highly uniform ultra-thin hybrid films with improved biocompatibility and host response, while avoiding bacterial infection.

3.1 Introduction

Nature is the source of a variety of processes, algorithms, materials, and designs that humankind attempts to mimic. The rationale behind is that they have proven their efficiency during evolutionary processes and as such rely on natural optimization over long periods of time, which we can adopt for new applications. For instance, the design of slippery, liquid-repellent porous surfaces to trap insects was inspired by the mechanism of *Nepenthes* pitcher plants.⁵⁹ The development of a potentially biocompatible artificial electric organ was inspired by an electric eel *Electrophorus*⁶⁰ and the construction of pneumatic shape-morphing elastomers was inspired by the morphogenesis of biological structures.⁶¹ Enamel-inspired columnar nanocomposites with combinations of high stiffness, damping and light weight, were achieved by sequential growth of zinc oxide nanowire carpets, followed by layer-by-layer deposition of a polymeric matrix around them.⁶²

Among the applicable and highly demanded materials, the class of bioactive surfaces is of immense societal importance as it impacts plenty biomedical application fields from implants to surgical tools and beyond. Indeed, the recent years have witnessed investment of enormous effort into the development of antibacterial materials for implant surfaces by applying various surface treatments.⁶³⁻⁶⁵ However, poor quality and adhesion of existing materials to the implant often lead to delamination of the coating from the implant, causing infection and implant rejection.⁶⁶

The composition of the bioactive materials plays a crucial role for their development. Metal ions, such as silver and copper, have shown to act against a wide range of bacteria, but their biocompatibility is poor when a high loading is required.^{67,68} Organic/polymeric materials, on the other hand, often require temporally and/or economically demanding manufacturing processes. Materials, which continuously release antibacterial agents into the environment to kill or inactivate bacteria in their proximity, can lead to bacterial resistance to many commonly used agents and influence the long-term performance of these surfaces.^{69,70} An alternative approach is most common in Nature and relies on the design of antibiotic-free surfaces that prevent adhesion of bacteria already in the early stage and, consequently, further biofilm formation.⁷¹ The holy grail herein is an inexpensive surface coating that has significant antibacterial activity against a wide range of microorganisms, while maintaining biocompatibility.

Over the last several decades, the outstanding antimicrobial properties of chitin-based materials have inspired researchers to adopt those for a variety of biomedical problems. Chitin is a biopolymer based on the N-acetyl-glucosamine and is naturally produced by

various fungi, insects, crustaceans, etc., which makes it the second most abundant polysaccharide in nature.^{37,72} Chitin has most of the desired attributes including biocompatibility, antibacterial and antimould activity, complete biodegradability, nontoxicity, and film-forming capability. Not surprisingly, numerous application domains are described in the literature for materials based on chitin or chitosan, the deacetylated form of chitin, which include biomedicine, pharmaceuticals, agriculture, cosmetics, and food packaging.⁷³ For instance, immobilized enzymes based on chitin and chitosan have provided an excellent platform to achieve a high yield in the bioprocessing for various forms of industrial and therapeutic enzymes.⁷⁴

Nanochitin, chitin-based constructs in form of nanocrystals, nanowhiskers, nanofibrils, etc., were used for the development of green, sustainable, and advanced functional materials e.g., sustainable permeation barrier films, mechanically reinforced biocomposites, sealants, hemostatic materials, adhesives, vaccine adjuvants, etc.⁷⁵ Such nanomaterials provide additional functionality due to their unique antioxidant, adhesive, optical transparency, mechanical, and other characteristics.^{76–79}

There are two methods to synthesize nanochitin, based on either top-down or bottom-up strategies. The top-down approach consists of purifying chitin with a base or by enzymatic hydrolysis to remove any proteins, acid treatment to remove inorganic minerals and bleaching to remove pigments and lipids. Further steps include conversion of the purified chitin into nanochitin by TEMPO-mediated oxidation, mechanical processing, partial deacetylation, and other methods.⁸⁰ In the bottom-up approach, pure chitin is completely dissolved in specific solvents to form chitin solutions, and then nanochitin is formed by electrospinning, self-assembly, or dissolution–regeneration.⁸⁰ Obviously, both approaches involve sophisticated multistage processes. Furthermore, the low solubility of chitin is an obstacle and impact both the processability and the purity and stability of the resulting films. This may be avoided by adapting the chemistry and performing the synthesis in a solvent-free environment, that is, from the vapor phase. However, such processes for chitin or chitinoid materials are not yet developed and must be established from scratch.

Inspired by the properties of chitin in Nature, we developed the first solvent-free vapor phase process for growing nanoscale coatings of chitin-based materials. Besides the growth of organic chitin, we present a completely new class of organic–inorganic hybrid polymers, which we coin “metallochitins” or more generally “metillosaccharides”. Our process is based on molecular layer deposition (MLD), which allows the linking of organic and inorganic building blocks in a controlled way and enables the film conformality with precise thickness control and film quality.^{81–83} While the organic chitin is grown from the monosaccharide N-Acetyl-D-mannosamine (ManNAc) and thionyl chloride, for a controlled growth of the hybrid metallochitins, we couple ManNAc with trimethylaluminum (TMA) or Titanium tetrakisopropoxide (TTIP) to obtain the respective biomimetic alumochitin or titanochitin thin films.

After successful film growth, the potential of the metallochitin films to mimic the antimicrobial behavior of chitin had to be assessed. Thus, we evaluated the attachment and proliferation of Gram-positive (*Staphylococcus aureus*, *S. aureus*) and Gram-negative (*Escherichia coli*, *E. coli*) bacteria to the alumochitin and titanochitin surfaces. The results show that both alumochitin and titanochitin MLD films prevent attachment of gram-positive and gram-negative bacteria, making the films highly interesting for the fabrication of bioactive surfaces. The results of in vitro proliferative behaviors of Human Embryonic Kidney (HEK293T) and human fibroblast cells, cultured on the obtained nanolayers, confirmed even better cell attachment and proliferation on the metallochitins than on the positive control. Consequently, the metallochitin films exhibit desirable characteristics such as biocompatibility while preventing bacterial attachment, as the chitin does in nature, thereby confirming its ability to mimic the natural functionality of chitin.

3.2 Experimental details

MLD synthesis of the metallochitin films.

The MLD processes were performed using the Savannah-100 reactor from Cambridge NanoTech. Ultra-high purity nitrogen was used as a carrier gas. The depositions were performed under a constant nitrogen flow of 20 standard cubic centimeters per minute (sccm) at a reactor pressure of about 1 Torr.

The films were deposited using n-Acetyl-d-mannosamine (ManNAc) (min. 98% pure, Biosynth Carbosynth), thionyl chloride (97% pure, abcr), trimethylaluminum TMA (97% pure, Sigma-Aldrich) and Titanium (IV) isopropoxide (TTIP) (97% pure, Sigma-Aldrich). Prior to use, all precursors were filled into airtight cylinders in a glovebox because of their sensitivity to air and moisture. The ManNAc and TTIP precursor bubblers were heated to 100 °C and 70 °C, respectively, to obtain sufficient vapor pressure. TMA and thionyl chloride were kept at room temperature during deposition. The reactor temperatures during chitinoid and alumochitin film growths were ranging from 110 to 125 °C. The reactant pulse, exposure and purge timing are denoted as (t1, t2, t3, t4, t5, t6), where t1 is the ManNAc pulsing time, t2 is the ManNAc exposure time, t3 is the purge after the ManNAc, t4 is the SOCl₂ dose time, t5 is the SOCl₂ exposure time, t6 is the purge time after the SOCl₂ exposures. For the ManNAc and SOCl₂ MLD the timing sequences were (6, 5, 25, 0.2, 3, 25) (in seconds). To enable the complete reaction an exposure time of several seconds was used after each precursor pulse. The MLD cycle

timing used for the alumochitin synthesis was (6, 5, 25, 0.015, 3, 25) (in seconds), for the corresponding pulse, exposure, and purge sequence of ManNAc and TMA. The titanochitin MLD cycle consisted of pulse (6, 5, 30, 1, 4, 30) (in seconds) for the corresponding pulse, exposure, and purge sequence of ManNAc and TTIP.

Attenuated total reflectance–Fourier transform infrared spectroscopy (ATR-FTIR).

ATR-FTIR measurements were carried out with a PerkinElmer Frontier spectrometer. To increase the signal to noise ratio, pressed nanopowder of ZrO_2 (Sigma Aldrich, <100 nm) was used as substrate for the ATR-FTIR measurements. All spectra were recorded in the range from 600 to 4000 cm^{-1} with 4 cm^{-1} resolution.

High resolution transmission electron microscopy (HRTEM).

HRTEM characterization was carried out with an Cs-corrected microscope FEI Titan (ThermoFisher, U.S.A.). To study the morphology of the deposited layer, the microscope was operated in a monochromated mode at 80 kV.

In situ quartz crystal microbalance (QCM).

In-situ quartz crystal microbalance (QCM) measurements were performed using a RC-cut, 6 MHz resonance frequency, polished, gold-plated, quartz crystal sensor (Phillip Tech.). The QCM crystal was mounted in a bakeable sensor housing (Inficon) and sealed using high-temperature epoxy (Epoxy Technology, U.S.A.). The QCM mass resolution was ~ 0.3 ng/cm². The quartz crystal of the QCM was pre-coated with an ALD-grown, 60-80 Å thick Al_2O_3 film prior to any new measurement, to generate identical conditions for all processes.

X-ray Reflectivity (XRR).

The thicknesses and densities of the samples were extracted from XRR measurements with a PANalytical X'Pert Pro diffractometer with Cu K α radiation. Single-side polished P-type silicon (100) wafers were used as substrates for the XRR measurements.

X-ray photoelectron spectroscopy (XPS).

The chemical composition and bonding of MLD films to the ZnO substrate was examined by XPS using a SPECS instrument equipped with a hemispherical electron analyzer and a monochromatized source of Al K λ x-rays. The calibration of the energy scale in all XPS spectra was done by placing the binding energy of characteristic C 1s peak at 284.5 eV. The XPS spectra were deconvoluted into several sets of mixed Gaussian-Lorentzian (G-L) functions with Shirley background subtraction. Pressed ZnO nanopowder (Sigma Aldrich, <100 nm particle size) was used as substrate for the XPS analyses.

In vitro antibacterial test.

50 μL of *E. coli* and *S. aureus* bacteria culture at an Optica density (O.D600) of 0.6 were seeded each on glass slides coated with the MLD films and glass covered with LB media and incubated for 24 hours in the incubator at 37 °C. After incubation the coated

glasses were washed 3 times with phosphate buffer saline (PBS) and the bacteria were dyed with a 4',6-diamidino-2-phenylindole (DAPI) solution (5 mg/ml) diluted in PBS (1:2000) and CellMask Orange Plasma membrane stain and washed three times with PBS. The DAPI and CellMask Orange -stained bacteria were imaged by confocal microscopy after 20 min of incubation. We used glass slides covered with crystalline nanocellulose as positive control and followed the same procedure as with MLD-coated slides.

In vitro biocompatibility test.

HEK293T cells

HEK293T cells were a kind gift of Dr. Maria Muñoz Caffarel. The cells were maintained in DMEN+10% FBS medium supplemented with 1% (w/v) L-glutamine and penicillin–streptomycin (100 IU/ml). The samples were sterilized by UV light for 3 h. 20,000 cells were seeded on each substrate and allowed to grow during several days in the incubator at 37 °C in 5% CO₂. The cells were dyed with CellMask Orange Plasma membrane diluted in PBS, after washing each sample three times with PBS. The cells were investigated by confocal microscopy after 5 min of incubation.

Primary Fibroblast cell line

Cells were maintained in DMEN+10% FBS medium supplemented with 1% (w/v) L-glutamine and penicillin–streptomycin (100 IU/ml). The samples were sterilized by UV light for 3 h. 20,000 cells were seeded on each substrate and allowed to grow during several days in the incubator at 37 °C in 5% CO₂. The cells were dyed with CellMask Orange Plasma membrane stain, diluted in PBS after washing each sample three times with PBS. The cells were investigated by confocal microscopy after 5 min of incubation.

Computational methods

All reported DFT calculations in this paper were performed using density functional theory implemented in the VASP5.4 code [6]. A hydroxylated monoclinic ZrO₂ (111) surface in a (2 × 2) surface supercell was used for MLD modelling. For the chitin films the ZrO₂ surface was modified with SOCl₂ as metal source and ManNAc as organic reactant while for alumochitin it was modified with TMA as metal source and ManNAc as organic reactant. The core electrons were described by projector augmented wave (PAW) potentials [7] and the valence electron configurations for this study are Zr: 5s² 4d², O: 2s² 2p⁴, C: 2s² 2p², N: 2s² 2p³ and H: 1s¹. The exchange–correlation functional was approximated by the Perdew–Burke–Ernzerhof (PBE) approximation [8]. The geometry was optimized by relaxing the ionic positions, using an energy cut-off of 400 eV as well as a Monkhorst–Pack k-point sampling grid of (2 × 2 × 1). The lattice parameters for this surface model are a = b = 14.70 Å, c = 32.45 Å, α = β = 90°, γ = 114°.

The convergence criterion for the energy is 1×10^{-4} eV and for the ionic relaxation, the convergence criterion for the forces is 2×10^{-2} eV /Å.

Adsorption energies were calculated following equation (1), which shows the example of TMA adsorption on hydroxylated ZrO₂ (111):

$$E_{\text{ads}} = [E(\text{Al}(\text{CH}_3)\text{-O-ZrO}_2) + 2E(\text{CH}_4)] - [E(\text{Al}(\text{CH}_3)_3) + E(\text{HO-ZrO}_2)] \quad (1)$$

where $E(\text{Al}(\text{CH}_3)\text{-O-ZrO}_2)$ is the total energy of TMA adsorbed on hydroxylated ZrO₂ (111), $E(\text{CH}_4)$ is the total energy of free CH₄ released after this reaction, $E(\text{Al}(\text{CH}_3)_3)$ is the total energy of free TMA and $E(\text{HO-ZrO}_2)$ is the total energy of the hydroxylated ZrO₂ (111) surface. For interaction of ManNAc with TMA adsorbed on hydroxylated ZrO₂ (111), the interaction energy was computed from:

$$E_{\text{int}} = [E(\text{ManNAc-Al-O-ZrO}_2) + E(\text{CH}_4)] - [E(\text{ManNAc}) + E(\text{Al}(\text{CH}_3)\text{-O-ZrO}_2)] \quad (2)$$

where $E(\text{ManNAc-Al-O-ZrO}_2)$ is the total energy of ManNAc bound to the MMA-ZrO₂ surface, $E(\text{CH}_4)$ is the total energy of free CH₄, $E(\text{ManNAc})$ is the total energy of ManNAc, and $E(\text{Al}(\text{CH}_3)\text{-O-ZrO}_2)$ is the total energy of MMA-ZrO₂ surface.

3.3 Results

3.3.1 Fabrication of organic chitin thin films by

MLD

The initial approach to grow ultrathin biomimetic chitinoid films was based on sequential and repeated activation of the surface with thionyl chloride (SOCl₂) vapors and a following self-limiting chemisorption of vaporized ManNAc on the substrate surface. During the first step, SOCl₂ acts as chlorinating agent, reacting rapidly with the surface-bound hydroxyl groups. In the second step, ManNAc binds to the chlorinated surface. This step generates new surface-bound hydroxyl groups, stemming from the ManNAc, which become available for repeated surface activation with the thionyl chloride,

thereby enabling the layer-by-layer growth of the chitinoid film. The ex-situ investigation of the chitinoid thin film by ATR-FTIR spectroscopy confirmed that its chemical structure resembles the structure of the reference natural chitin. The FTIR spectrum of the artificially grown chitin MLD film (Figure 3.1) shows all typical peaks characteristic of natural α -chitin (Table 3).^{84–86}

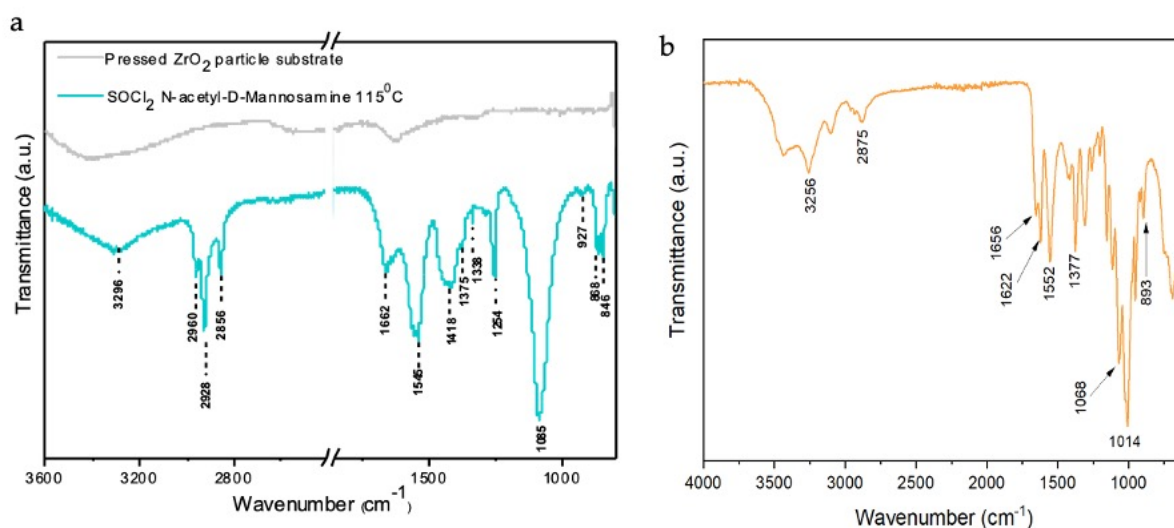


Figure 3.1: ATR-FTIR spectrum of (a) ManNAc/SOCl₂ MLD film, deposited at 115 °C (blue) and the initial pressed ZrO₂ powder (grey). (b) the natural α -Chitin.

We compared the bands obtained from the FTIR spectrum of the chitinoid MLD film (Figure 3.1, (a)) to the reference values measured for the natural α -Chitin (Figure 3.1, (b)). The FTIR spectrum of the chitin MLD film shows all the typical peaks characteristic of natural α -chitin. The major assignments of the peaks are summarized in Table 3.

Table 3: Assignments of the peaks in the ATR-FTIR spectrum of the sample after the ManNAc/SOCl₂ MLD process at 115 °C.

Wavenumber [cm ⁻¹]		Chemical bond
MLD-grown chitinoid film (Fig.3.1, a)	Natural chitin film (Fig. 3.1, b)	
846, 868	893	Ring stretching, β -1,4-glycosidic bond
1085 (broad)	1068, 1014	C-O stretching, C-O-C(ring), C-OH

1254	1258	Amide III (NHCO group)
1375, 1338	1377, 1317	C-H stretching and deformation of the CH ₃ group
1418	1420	CH ₂ wagging, C-H bending
1545	1552	Amide II band (N-H bending)
1662	1656, 1622	Amide I band (C=O stretching)
2960–2856	2962-2875	CH, CH ₃ stretching and asymmetric CH ₂ stretching
3296 (broad)	3256	N-H stretching

The non-line-of-sight deposition allows to coat a variety of substrate types and morphologies, for example ZrO₂ nanoparticles (NPs), which make a microscopic analysis of the films by HR-TEM easier (Figures 3.2).

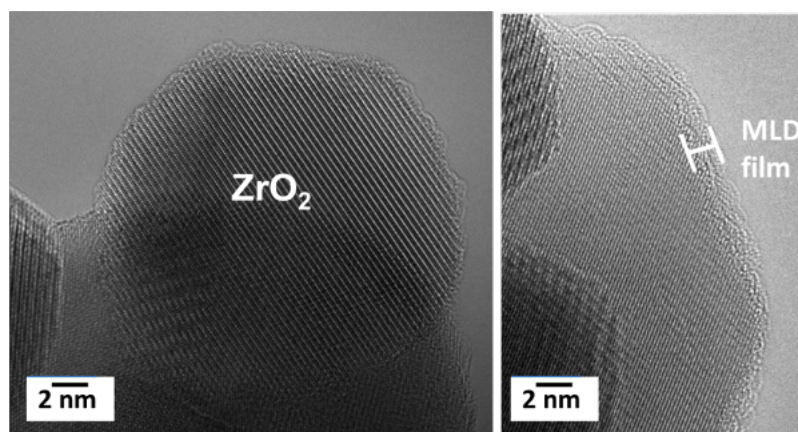


Figure 3.2: HR-TEM images of ZrO₂ NPs after 100 MLD cycles of ManNAc/SOCl₂, processed at 115°C

The XPS analysis of the MLD grown chitinoid sample (Figure 3.3, a,b) reveals the type of chemical bonding around the carbon and nitrogen atoms, characteristic of chitin,^{87,88} as seen in the measured natural chitin reference (Figure 3.3, b,c).

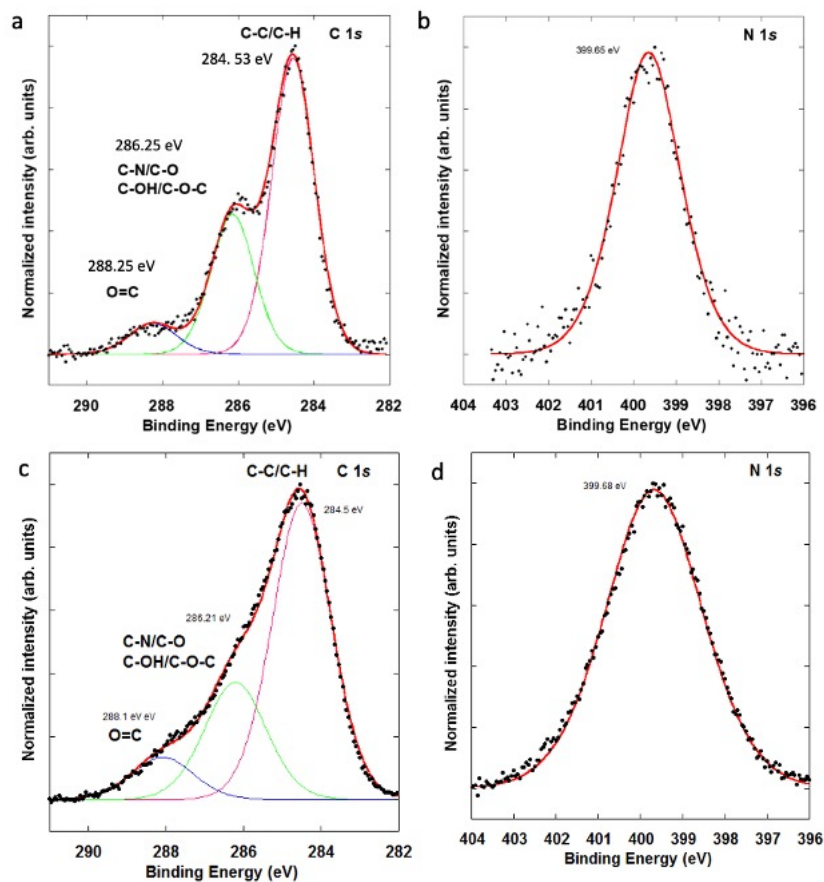


Figure 3.3: (a) C 1s and (b) N 1s XPS spectra of MLD-grown thin chitinoid film. (c) C 1s and (d) N 1s XPS spectra of natural α -Chitin.

In the XPS fits of the chitin reference sample we observe the same type of chemical bonding around carbon and nitrogen atoms as in the MLD grown sample. However, the peaks of the reference sample are slightly broader. We believe that the surface area of the chitin reference sample shows non-uniform charging, causing so-called uncontrolled charging. This type of charging can cause broadening of the XPS peaks (higher full width at half maximum (FWHM)) when analyzed using charge neutralization with low energy electrons. Indeed, the fitted C 1s peaks are broader than the corresponding peaks of the MLD grown chitin sample, which was conductive and therefore analyzed without electron flooding.

Thus, based on these data, it can be stated that we have obtained a conformal thin chitinoid film that mimics chitin in terms of chemical structure.

However, upon characterization in the TEM it was observed that the sensitivity of the chitinoid film to electron beams is very high which may be an obstacle for their

anticipated application. Therefore, their stabilization is desirable, which could be achieved through hybridization of the organic material with inorganics. Indeed, such strategies for stabilization are also observed in nature,⁸⁹ which has also inspired scientists to artificially hybridize (bio)polymers with inorganics to improve certain material properties, for example, the modulus of toughness.^{90,91}

3.3.2 Fabrication of hybrid alumochitin thin films by MLD

For fabricating hybrid alumochitin thin films by MLD, we used ManNAc and Trimethylaluminum (TMA) as reactants, that is, we replaced the SoCl_2 with an aluminum-containing metalorganic. A schematic of the idealized reaction mechanism for the alumochitin process is depicted in Figure 3.4 (a). Herein, the TMA binds to the surface-exposed hydroxyl groups. After purging and subsequent dosing of ManNAc, the saccharide binds with its oxygen functionalities from the hydroxyl groups to the aluminum, thereby restoring the hydroxyl surface species with its remaining hydroxyl functionalities. The growth per cycle (GPC) was $1.3 \pm 0.1 \text{ \AA/cycle}$, as extracted from the film thicknesses, measured by X-ray reflectivity (XRR), and the number of applied MLD cycles (Figure 3.4, (b)). No growth was observed by neither QCM nor XRR if only one of the precursors was supplied.

We studied the reaction between TMA and ManNAc in-situ with a quartz crystal microbalance (QCM) (Figure 3.4, (c),(d)). For a properly self-saturating and repeatable MLD process, the minimum dosing requirements for each precursor must be identified. This is done by varying the pulse duration of one precursor, while the purge times and the pulse duration for the second precursor are fixed. For identifying the minimum pulse time of TMA, the time sequence for TMA/ N_2 -purge/ManNAc/ N_2 -purge was (X, 20, 5, 20), with X being the variable pulse time of TMA (in seconds). From the figure 3.4 (c) (orange) it can be seen that a 1 s dose of TMA was sufficient for saturation. In an analogue procedure, with the variable sequence (1, 20, X, 20), the minimum dosing time for ManNAc (Figure 3.4 (c) (blue)) was identified to be 5 s. The QCM measurements further confirmed a linear mass increase with the number of MLD cycles (over 40 reaction cycles) (Figure 3.4, (d)). From the inset in the same figure a mass gain per cycle of the hybrid film of $\sim 20 \text{ ng/cm}^2$ can be derived.

The topography analysis by AFM (Figure 3.4 (e)) showed that the surface of the 20 nm thick alumochitin film is very smooth. The RMS roughness was 0.18 nm.

HR-TEM images of coated ZrO₂ NPs (Figure 3.4, (g)) show that the films grew highly conformally. The color coded EDX maps in Figure 3.4, (h) show that C, Al, and O are uniformly distributed throughout the film.

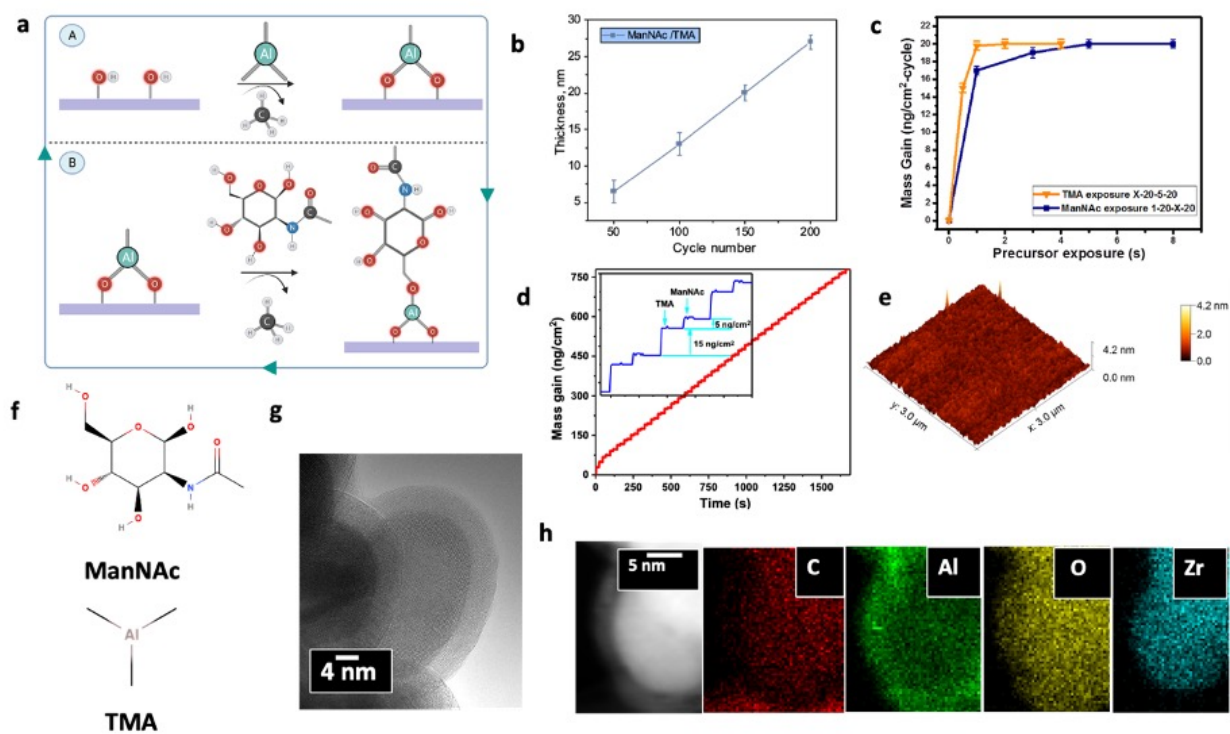


Figure 3.4: Alumochitin MLD growth and characterization. The film was grown at 115°C using ManNAc and TMA as precursors. (a) Idealized schematic of the surface chemistry for the alumochitin growth by MLD. (b) Thickness of alumochitin vs. cycle number, measured by XRR. (c) QCM mass gain per cycle of ManNAc (blue) or TMA (orange) vs. dosing times in a steady state regime at 115°C. (d) QCM mass gain versus time for the ManNAc/TMA MLD process on an ALD-Al₂O₃ pre-deposited surface at 115 °C. Inset: Expanded view of the mass gain during four reaction cycles. The growth was monitored over 40 reaction cycles using a pulse-purge timing sequence of 1s/20s/5s/20s for TMA/N₂/ManNAc/N₂, respectively. (e) Surface topography measured by AFM. The image shows the smooth surface of the as-deposited amorphous 20 nm thick alumochitin film with an RMS roughness of 0.18 nm. (f) Chemical structure of N-Acetyl-D-mannosamine (ManNAc) and trimethylaluminum (TMA). (g) High-resolution HR-TEM image of a 6 nm thick alumochitin film, conformally grown on ZrO₂ NPs. (h) TEM image of an alumochitin film deposited on a ZrO₂ nanoparticle and its corresponding color coded EDX maps of carbon, aluminum, oxygen and zirconium.

XPS confirmed the elementary composition of C, N, O and Al in the deposited film. The deconvolution of the signal around C1s and comparison to that of the organic chitinoid film (Figure 3.5 (a)) shows four main contributions with a slight difference in the bonding environment between both films.

Besides the presence of the chitin-characteristic C-C /C-H, C-N, C-O/C-O-C and C=O units, the decreased intensity of the C-O-C contribution in the alumochitin indicates the substitution of some C-O-C bonds with C-O-Al bonds. The N 1s XPS spectrum at the binding energy of ~ 400 eV (Figure 3.5, (b)) is assigned to C-N and N-H bonds of the acetamide group, characteristic of chitin. The Al 2p signal (Figure 3.4, (h)) confirmed the presence of Al-O bonds in hybrid films. Together with the above-mentioned decrease of the C-O-C peak in the C 1s spectrum, the Al 2p spectrum points towards the formation of C-O-Al bonds, indicated a successful incorporation of alumina into the chitinoid network.

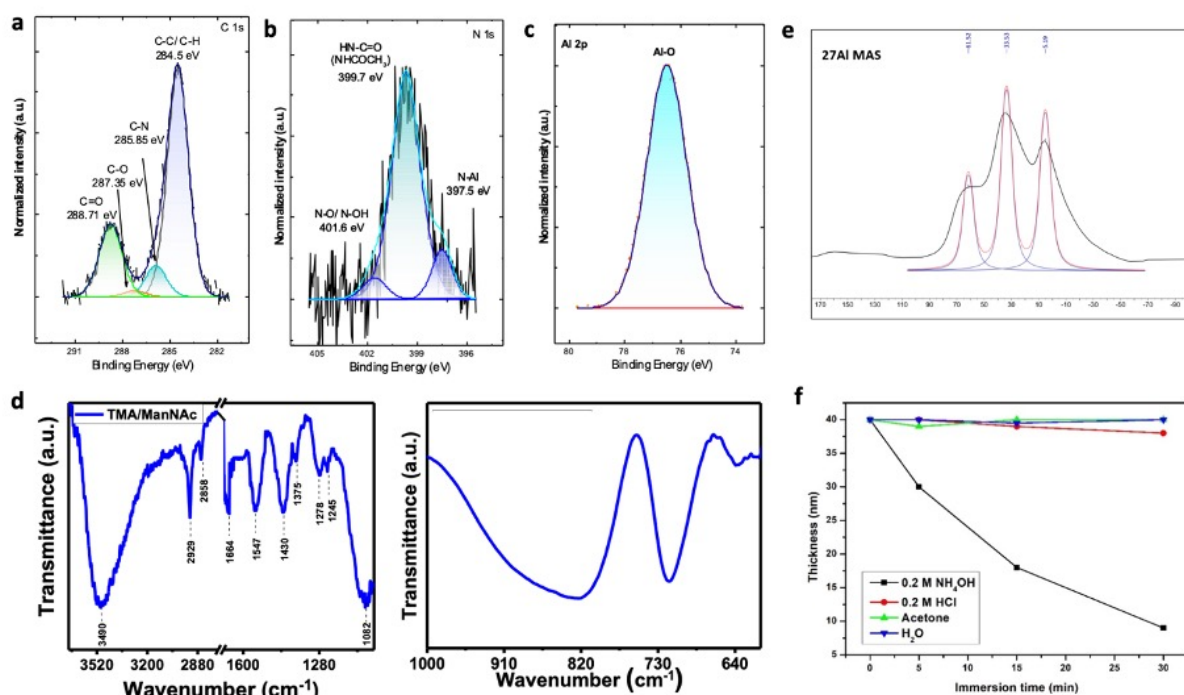


Figure 3.5: Alumochitin MLD growth and characterization. The film was grown at 115°C using ManNac and TMA as precursors. High-resolution (a) C 1s, (b) N 1s and (c) Al 2p core-level XPS spectrum of the alumochitin film. (d) ATR-FTIR spectrum of ManNac/TMA, after subtraction of the spectrum of the initial pressed ZrO_2 pellet. (e) ^{27}Al MAS NMR solid-state spectrum of a ManNac/TMA MLD film grown on ZrO_2 NPs at 115°C . (f) Alumochitin MLD film thickness changes as a function of time upon different chemical treatments.

An ATR-FTIR analysis of the film (Figure 3.5, (d)) verified the hybrid nature of the alumochitin, showing nearly identical signature as the organic chitinoid film and an additional broad band at $\sim 830\text{ cm}^{-1}$ which stems from Al-O species in the film.

The ^{27}Al MAS solid-state NMR spectrum of the alumochitin film (Figure 3.5, (e)) confirms three different Al bonding states with resonances at approximately 61, 33 and 5 ppm. Those are assigned to four-, five-, and six-fold coordinated Al, respectively.

The chemical stability of the alumochitin films was tested by exposing the films to three different solvents (Figure 3.5, (f)). Silicon wafers, coated with about 40 nm thick alumochitin films, were immersed into a strong base (0.2 M aqueous NH_4OH), a strong acid (0.2 M aqueous HCl), and an organic solvent (acetone) and water etching for 5, 15 and 30 min., followed by rinsing with deionized water. No film thickness change was observed after 30 min. treatment in water and acetone. Likewise, a 30 min. treatment with acid showed negligible changes in the film thickness. However, the treatment with the base caused a 77% reduction in film thickness, indicating considerable etching or dissolution of alumochitin in alkaline environment. Overall, this test showed great stability of the films at least in acidic, neutral, and some polar organic solvents.

3.3.3 Fabrication of hybrid titanochitin thin films by MLD

The successful growth of alumochitin raises the question whether further variations of metallochitins can be obtained. A very promising metalorganic candidate for testing was titanium isopropoxide (TTIP). It is a very common precursor in ALD for the growth of TiO_2 , but it chemically strongly differs to TMA. Its reactivity is lower, it has a less reactive ligand, it produces isopropanol as byproduct upon hydrolysis, has a higher charge state than aluminum, etc., which may have a very great impact on the metallochitin process and the resulting properties of the films. Titanium, or rather the oxidized finish of metallic titanium, is known to be biocompatible due to its resistance to corrosion by body fluids, which gives promise that a hybrid Ti-based material may have a positive impact in biomedical applications.

With this perspective, we developed a new process by substituting the previously used TMA with TTIP to hybridize the chitinoid film with titanium. Accordingly, the film was grown using TTIP and ManNAc as precursors. The process consisted of two steps, the initial binding of TTIP to the terminal hydroxyl groups of the substrate, and the subsequent binding of ManNAc to the titanium via the oxygen from the OH groups, thereby restoring the hydroxylated surface with the remaining hydroxyl functionalities of the saccharide (Figure 3.6, (a)).

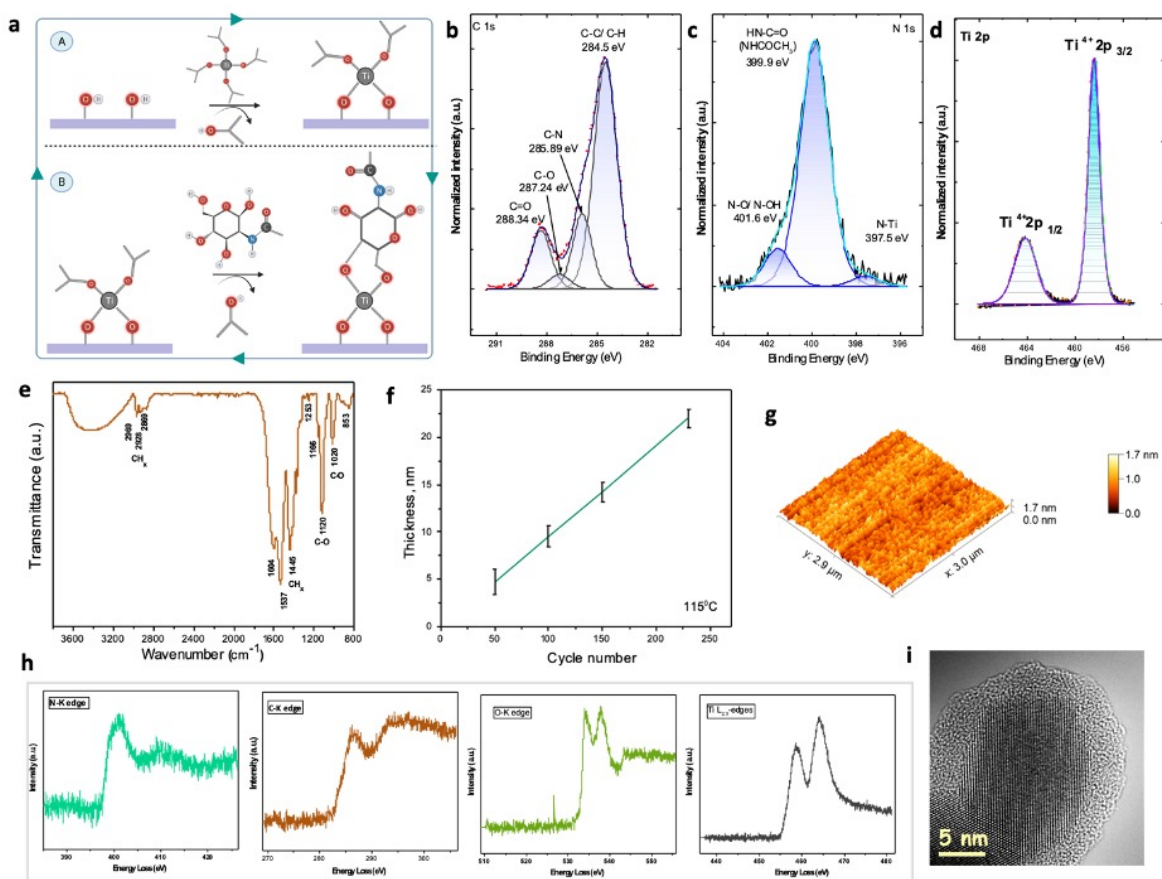


Figure 3.6: Titanochitin MLD film characterization. (a) Idealized schematic of the surface chemistry for growing a titanochitin thin film. High-resolution (b) C 1s, (c) N 1s and (d) Al 2p core-level XPS spectra. (e) ATR-FTIR spectrum of the titanochitin film, deposited at 115 °C, after subtraction of the spectrum of the neat pressed ZrO₂ pellet. (f) XRR measurements of the film thickness versus number cycles during titanochitin grown with a timing sequence of 1, 30, 6, 30 seconds for the pulse and purge of TTIP (1, 30) and ManNAc (6, 30), respectively, on Si (100) wafers at 115 °C. (g) Surface topography of the as-deposited 20 nm thick titanochitin film, measured by AFM. The RMS roughness was 0.32 nm. (h) STEM-EELS study of the titanochitin film: Spectra of the C-K, N-K, Ti-L, and O-K edges. The intensity is expressed in arbitrary units (a.u.) for better comparison. No smoothing was applied. (i) HR-TEM image of a thin titanochitin film, conformally wrapping a ZrO₂ NP.

The chemical composition of the titanochitin film was analyzed by XPS (Figure 3.6 a, b and c). The C 1s XPS spectrum shows several carbon species including C-C/C-H, C-N, C-O/C-O-C/C-OH, and C=O. The C-N peak in titanochitin is more intense than in alumochitin, which may result from the lower chemical reactivity of TTIP than TMA and consequently the lower probability of the metalorganic to attack the C-N bond of the ManNAc in a side reaction. The N1s spectrum shows the main peak at ~ 400 eV, which corresponds to the -NHCOCH₃ group in ManNAc and is characteristic to chitin. This confirms that the MLD process does not lead to cleavage of the acetyl group.

The Ti 2p spectrum shows a doublet with binding energies of 464.1 and 458.3 eV, corresponding to the core level binding energies of Ti2p_{3/2} and Ti2p_{1/2}, consistent with the Ti-O-type bonding scheme in TiO₂ (Ti⁴⁺).⁹²

FTIR Spectra of the film are shown in Figure 3.6 e. Peaks characteristic of chitin were detected at 1310–1320 cm⁻¹ (CN-stretching, amide III), 1253 cm⁻¹, (CH₂-stretching), 1540 cm⁻¹ (NH-bending, amide II), 1604 cm⁻¹ (CO-stretching, amide I), 2928 cm⁻¹ and 2869 cm⁻¹ (CH_x-stretching) and ~ 3400 cm⁻¹ (OH-stretching).⁹³ The strong features at 1020 cm⁻¹ and 1120 cm⁻¹ correspond to the symmetric and asymmetric C-O stretching modes of the ManNAc ring and the formed Ti-O-C bonds. The strong peak at 1166 cm⁻¹ can be linked to the C-C bonds in ManNAc and potentially some unreacted isopropoxy groups of TTIP.

X-ray Reflectivity (XRR) was used to characterize the titanochitin film growth. Figure 3.6 (f) shows a linear correlation between the XRR-measured film thickness and the number of growth cycles with a resulting average GPC of ~ 1.0 Å/cycle. From AFM measurements an average RMS surface roughness of the as-deposited 20 nm titanochitin film was calculated with 0.32 nm (Figure 3.6, (g)). The titanochitin layer, grown on ZrO₂ nanoparticles, was further analyzed by HR-TEM and electron energy loss spectroscopy (EELS). The STEM-EELS spectrum (Figure 3.6, (h)) of the C K-edge shows a peak at 286.3 eV and a weak hump at ~ 295 eV, reflecting the presence of amorphous organic carbon material.^{94,95} The N-K edge shows a π^* peak at ~ 401 eV and a σ^* -peak at around 410 eV, stemming from the amide bond in the ManNAc of the titanochitin.⁹⁶ The Ti-L spectrum shows two well-defined major L3 and L2 edges with a separation of 5.4 eV, on the same energy position as amorphous TiO₂, confirming the presence of Ti-O bonds.⁹⁷ The HR-TEM micrograph in Figure 3.6 (i) shows that the MLD process grows a highly conformal titanochitin layer on zirconia nanoparticles.

The barrier performance of hybrid alumochitin and titanochitin organic-inorganic thin films synthesized on PEN substrate was evaluated. The WVTRs were continuously measured for each sample over a number of tries using the mentioned above Gintronic method. Only the average of those 3 WVTR values that were measured in 3 consecutive

tries and were within 3 percent deviation from each other, are considered by the system to be true WVTR values.

For the formation of the thin film, the substrate plays a crucial role, as the functional groups in the polymer may enable or hinder thin film growth. For the deposition of a barrier layer on PEN, it could be useful to use a preconditioning of the surface to enable or enhance the growth. We performed a surface modification of PEN using an oxygen plasma treatment. Such surface oxidation results in the formation of various types of chemical bonds between the carbon and the oxygen, e.g., C=O, O-C-O, O-C=O and -C(=O)-O-C(=O)-.

The WVTR value for the 40 nm alumochitin film on a PEN substrate reached 0.24 g/(m² day), which is ~3 times lower than that of the uncoated PEN reference. The WVTR value for the 40 nm titanochitin film on a PEN substrate increased compared to the reference sample and reached 1.40 g/(m² day). This indicates that alumochitin possesses better water vapor barrier properties than titanochitin, which is most likely due to alumina counterpart of the hybrid film.

In conclusion, the analysis shows that smooth conformal alumochitin and titanochitin films can be grown by MLD. Both films contain organic chitinoids and an inorganic metal-O network, making the construct a chitin mimicking organic inorganic hybrid.

Although the developed MLD processes for alumochitin and titanochitin proved to work, understanding of the atomistic mechanism of the film growth from the thermodynamic perspective is necessary. For this purpose, first principles density functional theory (DFT) calculations were done for a detailed understanding of the growth mechanism of the hybrid metallochitin thin films. DFT modeling work presented in the chapter below has been done in collaboration with the Tyndall National Institute, by Arbresha Muriqi and Dr. Michael Nolan.

3.4 Mechanistic investigations. DFT analysis of the steric trends of the reaction

3.4.1 Alumochitin DFT studies

We performed density functional theory (DFT) calculations to study the energetic landscape of the surface reactions for a growth of alumochitin (Fig. 3.6, a). The starting point was a hydroxylated ZrO_2 surface, in analogy to the experiments. During the exposure TMA readily reacts with OH groups on the hydroxylated ZrO_2 surface where protons from the OH groups are transferred to the methyl ligands (CH_3) of TMA to form methane (CH_4) molecules. Al attaches to the surface through an O bridge by forming Lewis acid-base Al-O adducts (Fig. 3.7, a (1)). Since loss of one or two methyl groups from the TMA is possible, we examined two possible terminations of ZrO_2 surface after a TMA pulse, dimethyl ZrO_2 ($\text{Al}(\text{CH}_3)_2\text{-ZrO}_2$, DMA- ZrO_2) and monomethyl ZrO_2 ($\text{Al}(\text{CH}_3)\text{-ZrO}_2$, MMA- ZrO_2). In the MMA- ZrO_2 surface model, with the energy change of -1.8 eV, two methyl ligands from the adsorbed TMA react with two protons from the surface OH groups to form two CH_4 molecules, which subsequently desorb. Here, Al binds with two surface O with bonding lengths of 1.70 Å and 1.76 Å and the surface is left with one CH_3 ligand that can react with ManNAc during the following pulse. The MMA- ZrO_2 model was calculated to be energetically more favorable than the DMA- ZrO_2 model (-1.8 eV vs. -1.4 eV), which is why we continued the modelling with the MMA- ZrO_2 . During the ManNAc pulse (Fig. 3.7, a (2)), a proton from an OH group of ManNAc transfers to the CH_3 ligand to form a new CH_4 molecule while the remaining O binds to the Al of MMA with an Al-O distance of 1.69 Å. Thus, the second half reaction with the interaction energy of -0.91 eV leads to an exchange of a CH_3 ligand with ManNAc and a regeneration of the surface with OH groups of ManNAc, ready to react with TMA in the next cycle. Here, the Al atom is tri-coordinated, with Al-O distances of 1.69 Å and 1.74 Å to the surface oxygen sites and Al-O distance of 1.69 Å the ManNAc oxygen site.

The DFT calculations further suggest that in the second MLD cycle the mechanism proceeds through the same reaction pathway as in the first cycle. However, the interaction energies significantly change. Based on the exothermicity of the reactions, three different options were analyzed, two alternative unidentate reactions or a bidentate reaction of TMA with the surface bound ManNAc. The calculated interaction energies suggest that the bidentate, two-ligand elimination reaction is most likely to happen (Fig. 3.7, a (3)). In this case, after the reaction of TMA and ManNAc, one CH_3 remains for a

reaction in the following cycle. With the interaction energy of -4.96 eV, TMA binds to ManNAc through two oxygens leading to the formation of the two new Al-O bonds with distances 1.73 Å and 1.72 Å.

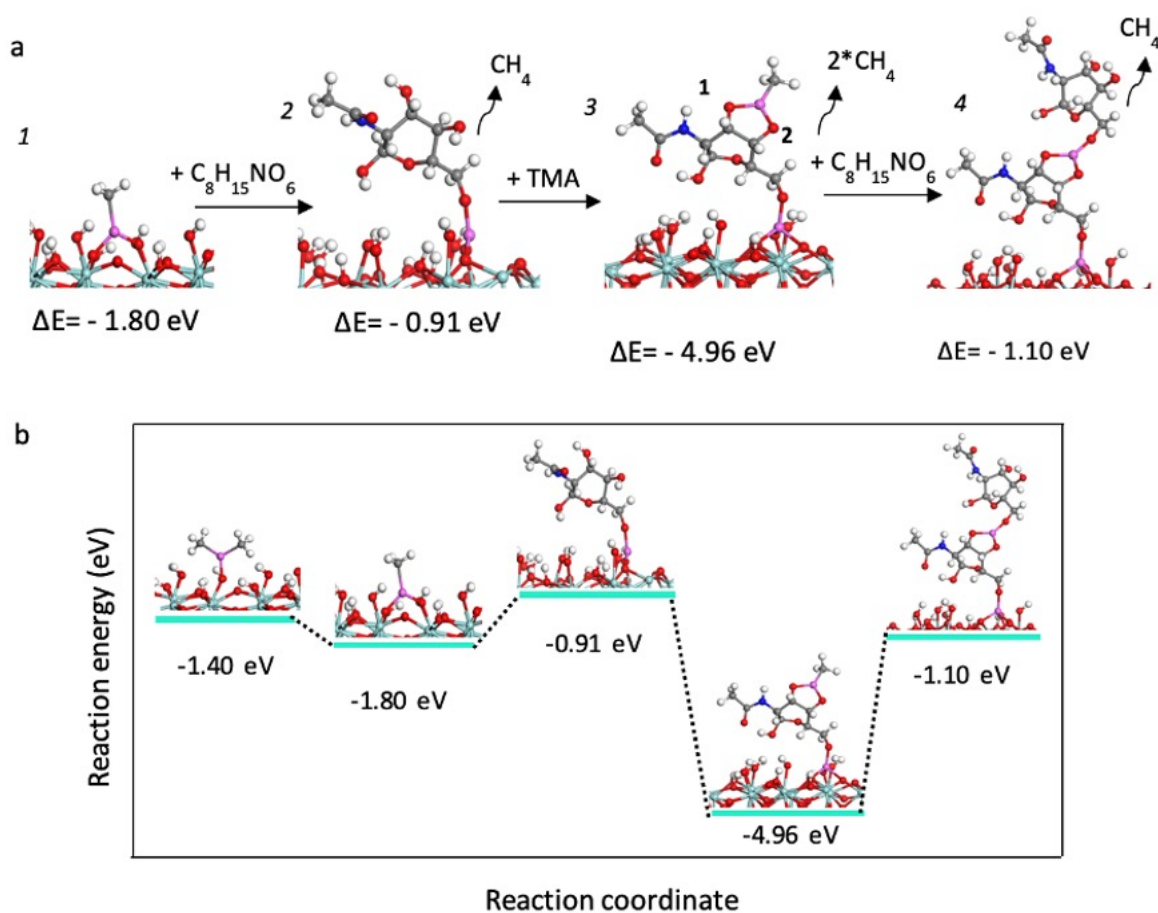


Figure 3.7: DFT calculation results: Stepwise investigation of the surface reaction mechanisms during metallochitin MLD. (a) Computed reaction energetics for the relevant reaction products during the alumochitin formation. Atomic structures of (1) monomethyl-Al-ZrO₂ (MMA-ZrO₂) (Al-CH₃-ZrO₂), (2) reaction product of MMA-ZrO₂ with ManNAc, (3) two-ligand elimination reaction after which one CH₃ ligand is left to react with ManNAc in the second half reaction of the following cycle, (4) reaction product of the MMA-terminated surface with ManNAc in the second cycle. (b) Calculated free-energy profile for 2 alumochitin growth cycles on a hydroxylated ZrO₂ surface.

During the interaction between TMA with ManNAc in the second cycle (Fig. 3.7, a (4)), the proton of the OH group of ManNAc transfers to the methyl ligand of TMA and form a CH₄ molecule, released later as a byproduct, while the remaining O of ManNAc binds to the Al atom of TMA with an Al-O distance of 1.65 Å. The interaction energy upon forming the Al-O bond is -1.10 eV. The calculated energetic landscape of 2 MLD cycles of alumochitin (Fig. 3.7, b) shows exothermic reactions with strong interactions

between TMA and ManNAc, confirming that the proposed reaction mechanism for the formation of hybrid alumochitin is energetically favorable.

3.4.2 Titanochitin DFT studies

Having characterized the alumochitin system, we proceeded to investigate its titanium analogue - titanochitin, aiming to expound the reaction mechanism and provide deeper insight into the surface chemistry (Fig. 3.8, (a), (b)).

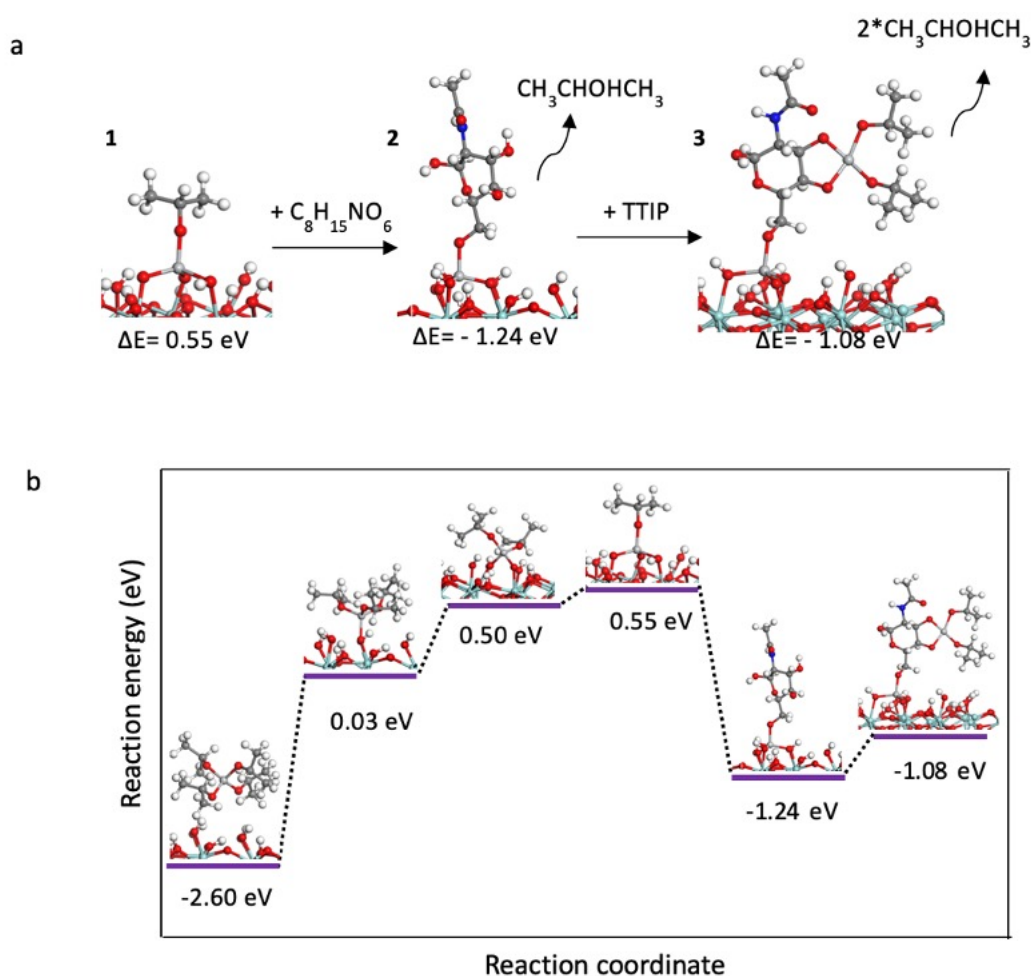


Figure 3.8: DFT calculation results: Stepwise investigation of the surface reaction mechanisms during metallochitin MLD. (a) Atomic structures of (1) the hydroxylated ZrO₂ surface after exposure to TTIP (after elimination of three ⁱPr-OH molecules), (2) the reaction products of ManNAc with the ⁱPr-OTi-ZrO₂ surface, (3) reaction of TTIP with the immobilized ManNAc. (b) Calculated free-energy profile of the surface reactions between ManNAc and TTIP at the hydroxylated ZrO₂ surface as a model system. Color code for the atomic structures: Cyan-Zirconium, Red-Oxygen, Purple-Aluminium, Light Gray- Titanium, Gray-Carbon, Blue-Nitrogen, White-Hydrogen.

The large exothermic gain in energy of -2.6 eV has been revealed when the TTIP interacts with the hydroxylated ZrO_2 model surface. There was no spontaneous proton transfer from the surface to the ${}^i\text{Pr-O}$ ligand and the energy cost for this H transfer process, that leads to the formation of a new Ti–O bond with a length of 1.83 Å and the loss of one ${}^i\text{Pr-OH}$ molecule, is 0.03 eV. The energy cost for the second ligand loss reaction, leading to the formation of two new Ti–O bonds with lengths of 1.88 Å and 1.80 Å and a release of two ${}^i\text{Pr-OH}$ molecules, is 0.5 eV.

During the third ligand loss reaction (Fig.3.8, a (1)), three new Ti–O bonds with lengths of 2.05 Å, 1.81 Å and 1.82 Å are formed and the third ${}^i\text{Pr-OH}$ molecule is released with the energy cost of 0.55 eV. After the TTIP pulse, the surface remains with one ${}^i\text{Pr-O}$ ligand and the consecutive pulse will result in an exchange of the ligand with a ManNAc molecule.

During the reaction of ManNAc with the ${}^i\text{Pr-OTi}$ terminated ZrO_2 surface (Fig.3.8, a (2)), a side proton from an OH group of ManNAc transfers to the ${}^i\text{Pr-O}$ ligand to form a new ${}^i\text{Pr-OH}$ molecule while the remaining O binding to the Ti site of TTIP with a Ti–O distance 1.84 Å. The calculated interaction energy is -1.24 eV, which confirms that this reaction is favorable. To examine the reactivity of ManNAc in the second cycle of the MLD process, we have built the model where the remaining hydroxyl groups of ManNAc react with TTIP (Fig.3.8, a (3)), and form two new Ti–O bonds ($\Delta E = -1.08$ eV) with distances of 2.0 Å.

The calculated energetic landscape of the titanochitin buildup (Fig.3 b) demonstrates that ManNAc reacts favorably with TTIP also in the second cycle of the MLD process and confirms that the proposed reaction mechanism for TTIP/ManNAc MLD is energetically feasible and can lead to the formation of the hybrid titanochitin.

3.5 Bactericidal activity of the alumochitin and titanochitin MLD films against Gram-positive (Staphylococcus aureus) and Gram-negative (Escherichia coli) bacteria

The primary reason for the development of the chitinoid films is the mimic of the antimicrobial activity of natural chitin,^{98,99} therefore the antibacterial properties of the MLD films were characterized in vitro. We chose the bacterial strains Staphylococcus aureus (S. aureus) and Escherichia coli (E. coli) as models for Gram-positive and Gram-negative bacteria, respectively. After 24h of culture, the cells were dyed with DAPI and CellMask Orange fluorescent dyes to label nuclear DNA and cellular plasma membranes, respectively, for an identification by fluorescence microscopy (Figure 3.9, (a), (b)). DAPI labels DNA-containing bacterial cells, regardless of their physiological status.^{100,101} CellMask Orange is used to uniformly label the plasma membrane of the bacterial cells. Both stains are cell-permeant, which allows to use them as stain for both intact (live) and damaged (dead) bacterial cells simultaneously.

An MLD-grown silicon-based hybrid aluminosilazane (SiAlCNH) film, synthesized with sequential surface reactions of trimethyltrivinylcyclotrisilazane (V_3N_3) with trimethylaluminum (TMA),¹⁰² has been used as positive control substrate for the growth of E. coli. Chemically pure cellulose nanocrystal (EnCNC)¹⁰³ films with the native cellulose structure served as a positive control substrate for the growth of S. aureus, due to its significant promotion of the growth of those bacteria. Glass substrates, coated with alumochitin or titanochitin and exposed to S. aureus and E. coli, have been analyzed by confocal microscopy to assess their ability to inhibit bacterial colonization and biofilm formation. We compared the bacterial adhesion to the metallochitins with the corresponding ceramic (TiO_2 and Al_2O_3) grown on the same substrates by ALD. The resulting confocal micrographs of stained S. aureus and E. coli bacterial biofilms are shown in Figure 3.9.

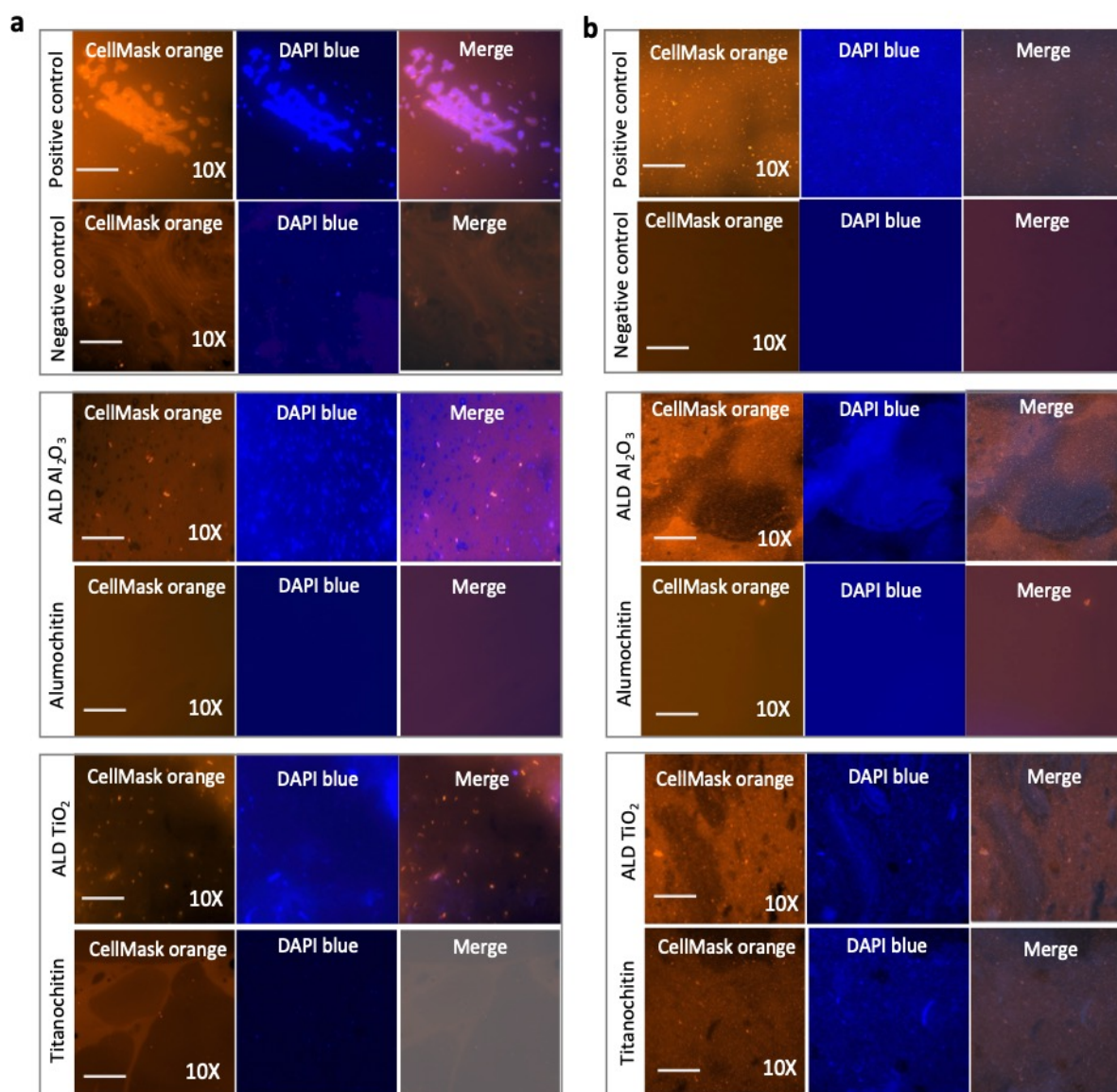


Figure 3.9: Antibacterial activity of alumochitin and titanochitin against Gram-positive (*S. aureus*) and Gram-negative (*E. coli*) bacteria. Confocal micrographs of (a) *E. coli* and (b) *S. aureus* bacterial biofilms on inorganic alumina and titania and hybrid alumochitin and titanochitin substrates after 24h of exposure with two different original magnifications, 10x (scale bar= 10 μ m). A 25 nm thick hybrid silicon-based alumosilazane (SiAlCNH) MLD film has been used as a positive control substrate for the growth of *E. coli*. A crystalline nanocellulose film served as a positive control substrate for the growth of *S. aureus*. No bacterial growth was observed on the negative control samples (samples exposed only to the media, but without bacteria), as expected. Both, Gram-negative and Gram-positive bacteria were stained with DAPI (blue) and CellMask orange to label the plasma membranes and nuclei, respec-

Both bacteria rapidly proliferated on the positive control samples with a crystalline nanocellulose film,¹⁰³ while coverslips coated with alumochitin prevented the attachment of both bacterial strains over 24 h, clearly demonstrating the efficient repellence. The corresponding inorganic alumina film, however, allowed proliferation of both types of bacteria with a uniform distribution on the substrate. This is not surprising as it is known that Al₂O₃ has no antibacterial effect,¹⁰⁴ neither on *E. coli*¹⁰⁵ nor on *S. aureus*.¹⁰⁶

As reference for chitin, we used a chitin-nanocrystal film obtained after enzymatic oxidative cleavage of natural α -Chitin.¹⁰⁷

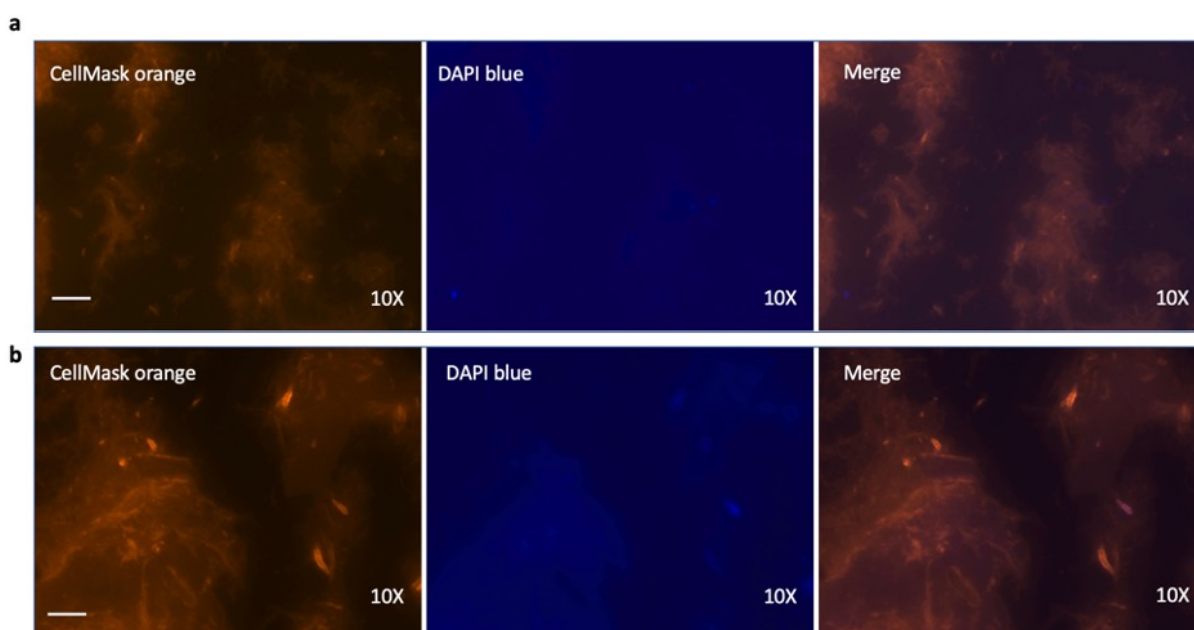


Figure 3.10: Antibacterial activity of natural nanochitin film against Gram-positive (*S. aureus*) and Gram-negative (*E. coli*) bacteria. Confocal micrographs of (a) *E. coli* and (b) *S. aureus* bacterial biofilms on nanochitin substrates after 24h of exposure, original magnifications 10x (scale bar= 10 μ m). As expected, no bacterial growth was observed on the negative control samples. Both *S. aureus* and *E. coli* were stained with DAPI (blue) and CellMask orange to label the plasma membranes and nuclei, respectively.

The results show that the natural chitin surface did not support neither *S. aureus* nor *E. coli* growth (Figure 3.10), in agreement with the previously reported antibacterial activity of chitin.^{98,99,107,108}

The titanochitin had a somewhat different behavior. It inhibited the formation of an *E. coli* biofilm, but not the formation of a *S. aureus* biofilm. Individual bacterial cells as well as small microcolonies were observed, suggesting a significant difference in the bacterial inhibition mechanisms of the two metallochitins. Like alumina, the corresponding inorganic titania surface promoted both *S. aureus* and *E. coli* attachment and proliferation.

Titania is known to be biocidal mostly based on its photocatalytic property that leads to disinfection upon irradiation with UV light.^{109, 110} In order to extend the light absorption into the visible region and improve the photo-generated charge-transfer process TiO_2 has been doped with various dopants.^{111,112}

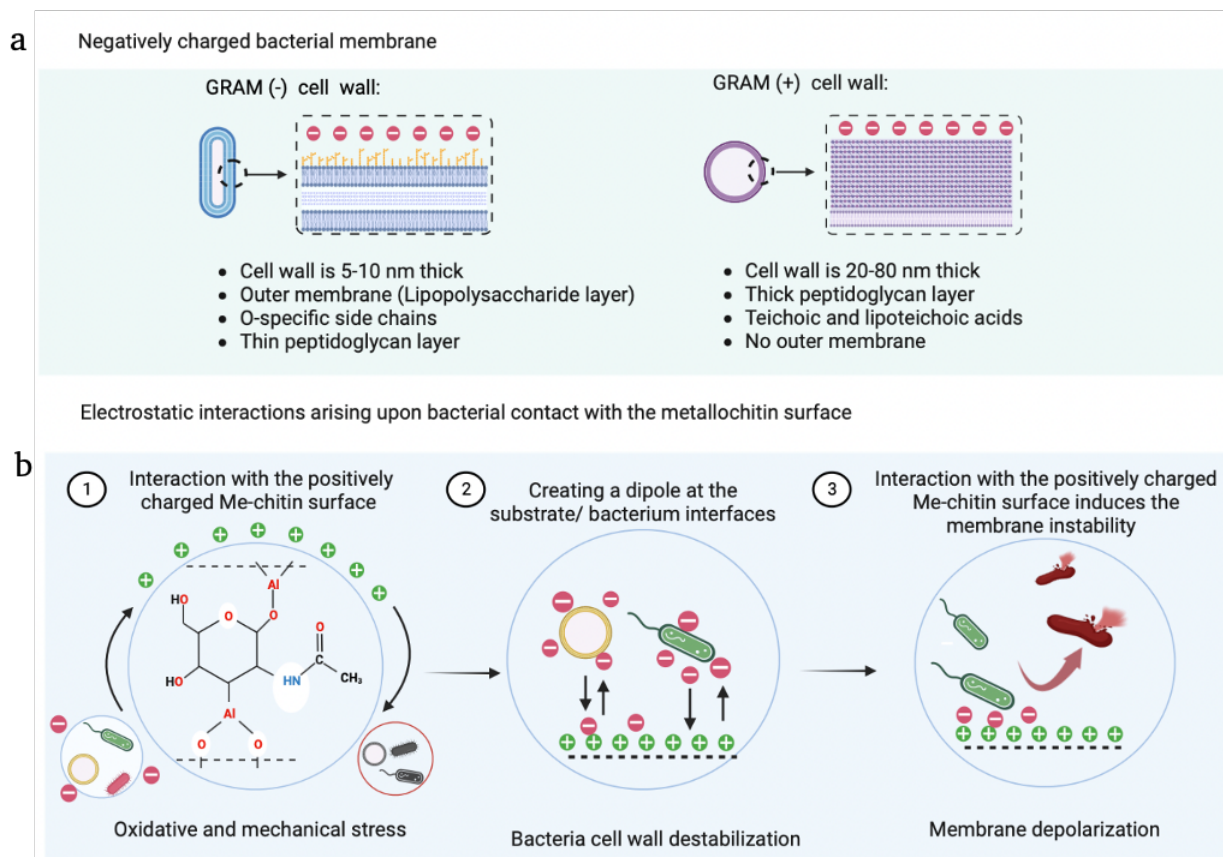


Figure 3.11: Mechanism of the antibacterial action of alumochitin and titanochitin against Gram-positive (*S. aureus*) and Gram-negative (*E. coli*) bacteria. (a) Main differences between the cell walls of Gram-negative and Gram-positive bacteria. (b) Schematic illustration of the electrostatic interactions between the positively charged metallochitin surfaces and the negatively charged bacterial surfaces, resulting in the physical disruption of the bacterial cell wall.

Bacterial adhesion is the initial step in colonization and biofilm formation. Therefore, it is important to understand and control the complex interface phenomena that

happen upon bacterial contact with the substrate. This complex process is based on a blend of van-der-Waals, electrostatic double-layer, acid–base, and/or hydrophobic interaction forces.^{113–116}

The main differences of Gram-positive and Gram-negative bacteria lie in their membrane construction, but generally most bacteria are negatively charged due to the presence of carboxyl, amino and phosphate groups on the surface of their cell walls (Figure 3.11, a).¹¹⁷ The Gram-negative cell wall is composed of an outer membrane, a peptidoglycan layer, and a periplasm, which is the space between the inner cytoplasmic membrane and outer surrounding membrane.¹¹⁸ The lipopolysaccharides (LPS), phospholipids, and proteins are the constituents of the outer cell membrane of gram-negative species. In Gram-positive bacteria, the outer membrane is missing, while the cell wall contains several peptidoglycan layers with covalently bound teichoic acids, unique to the Gram-positive cell wall, and proteins.¹¹⁹ The Gram-negative bacterial cell wall is thinner (5-10 nm) than the cell wall of Gram-positive bacteria (20-80 nm).¹²⁰ *E. coli* has more negatively charged surface sites than *S. aureus*, as determined by electrophoretic mobility measurements.¹²¹ Electrostatic attraction between a positively charged surface and negatively charged bacterial cells is an important aspect with regard to the antimicrobial activity of various materials.¹²² Due to its polycationic nature, chitosan and its derivatives are more efficiently acting against Gram-negative than against Gram-positive bacteria.¹²³ The positively charged NH₂ groups in chitosan have a strong attractive interaction with the negatively charged bacterial membrane, which causes its disruption. However, the antibacterial efficiency of chitosan is limited because amino groups are relatively weak positive charge centers. Therefore, extensive research has been carried out to increase the water solubility of chitosan to functionalize it with more positively charged groups.¹²⁴

Accurate characterization of substrates is essential to obtain reliable correlations between the material composition and bacterial adhesion. To gain further insights into the various mechanisms underlying the antibacterial selectivity and activity of both metallochitins, we analyzed the bacterial adhesion trends with respect to the surface chemistry and the important physicochemical variables.

The results of this studies regarding hydrophobicity, zeta potential and surface roughness are summarized in Table 4.

In the first instance the surface charge may play a role for the adhesion. The surface zeta potentials of the alumochitin and titanochitin films at pH=7 were measured to be $+ 40 \pm 3$ mV and $+ 18 \pm 3$ mV, respectively. Uncoated zirconia nanoparticles, which were used as a substrate for the measurements, had a zeta potential of $+ 30$ mV, which agrees with the literature-known values.^{125,126} A high absolute value of the zeta potential causes a strong electrostatic repulsion between suspended particles of the same surface charge, which results in their efficient dispersion.

If opposite, the strength of the surface charge can also have a decisive impact on the substrate-bacterial cell interaction.¹²⁷ For instance, surfaces with high positive zeta potential values can strongly act on negatively charged cell walls of *E. coli* and disintegrate them.¹²⁸

Table 4: Substrate parameters that influence the bacterial adhesion to the metallochitins and corresponding metal oxides.

Sample	Water contact angle [°]	Zeta potential [mV] (pH=7)	RMS roughness [nm]	Film thickness [nm]
Alumochitin	67 ± 2	40 ± 3	0.18	20 ± 0.5
Titanochitin	76 ± 2	18 ± 3	0.32	20 ± 0.5
ALD Al ₂ O ₃	50 ± 2	21 ± 3	0.46	20 ± 0.5
ALD TiO ₂	43 ± 2	-5 ± 3	0.49	20 ± 0.5

The negative charge on the cell surface of Gram-negative bacteria is higher than that on Gram-positive bacteria due to the presence of LPS at the external surface.^{121,129} The positive zeta potential of alumochitin is more than twice as high as that of titanochitin, which may be the reason for the stronger electrostatic attraction between alumochitin and the negatively charged bacterial cell wall. This may lead to mechanical stress and deformation of the cell membrane, as schematically shown in Figure 3.11 (b). The bactericidal effect of titanochitin against gram-negative *E. coli* and the ineffectiveness against gram-positive *S. aureus* can be explained by the fact that *S. aureus* has a thicker cell wall than *E. coli* and lacks an outer surface membrane.

The surface roughness and micro/nano topography are further factors that play a critical role in bacterial attachment. As the roughness increases, the available surface area for bacteria to attach also increases. The bacteria will adhere preferentially to topographic irregularities for maximizing the bacteria-surface area, resulting in promotion of biofilm formation.¹³⁰ The very low surface roughness of the metallochitin films can limit the number of interaction events and in this way reduce bacterial adhesion and growth. Namely, on a flat film the bacterium can only interact with its bottom surface while there are no lateral binding points which are present in corrugated surfaces. *S. aureus* bacteria did not attach to the alumochitin films with an RMS roughness of 0.18

nm but had a tendency to attach to the rougher (RMS roughness of 0.32 nm) titanochitin films.⁷⁶

From experimental, kinetic, and thermodynamic studies it was found that strongly hydrophilic surfaces with high negative zeta potential values minimize the adhesion of *S. aureus* and *E. coli*.¹²⁸ Acetamide, Metal-O-C and other functional groups are localized and immobile due to the chemisorptive nature of the MLD reactions during the alumochitin and titanochitin synthesis. Such electrostatic interactions can form dipoles at substrate/bacteria interfaces, which can be sufficient to disrupt the cellular membranes of the bacteria.¹³¹

3.6 Biocompatibility of the metallochitin films

3.6.1 Human Embryonic Kidney (HEK293T)

cells growth

The biocompatibilities of the alumochitin and titanochitin films were investigated with the proliferative behaviors of Human Embryonic Kidney HEK293T cells cultured on the substrates in vitro. Similar to the bacterial growth, the growths were compared to those on the corresponding inorganic films and uncoated cover slips (control samples). The HEK293T cell attachment and proliferation on the different substrates were analyzed after 1, 3 and 6 days. A selection of fluorescence images from different substrates is shown in Figure 3.12 (a-e). All coatings promoted HEK293T cells attachment and proliferation during 1 to 6 days of incubation. The proliferations of HEK293T cells cultured for 6 days on titanochitin and TiO₂ were significantly higher than on coverslips without coating, confirming an excellent promotion of the films for cell proliferation (Fig. 3.12, f). The number of cells grown on alumochitin after 6 days is comparable to that on Al₂O₃ and demonstrates a similar proliferation as on uncoated glass coverslips, which served as positive control. Thus, the MLD substrates are highly biocompatible and suitable for the growth of HEK293T cells, even though slight differences between the titanochitin and alumochitin behaviors and their tendencies in comparison to their

parent ceramics exist. The titanochitin shows the best performance, even outperforming TiO_2 , which is known to be highly biocompatible. These results are in line with the biocompatibility experiments, reported for natural crystalline nanochitin, suitable for the controlled HEK293T cell growth and proliferation.¹⁰⁷

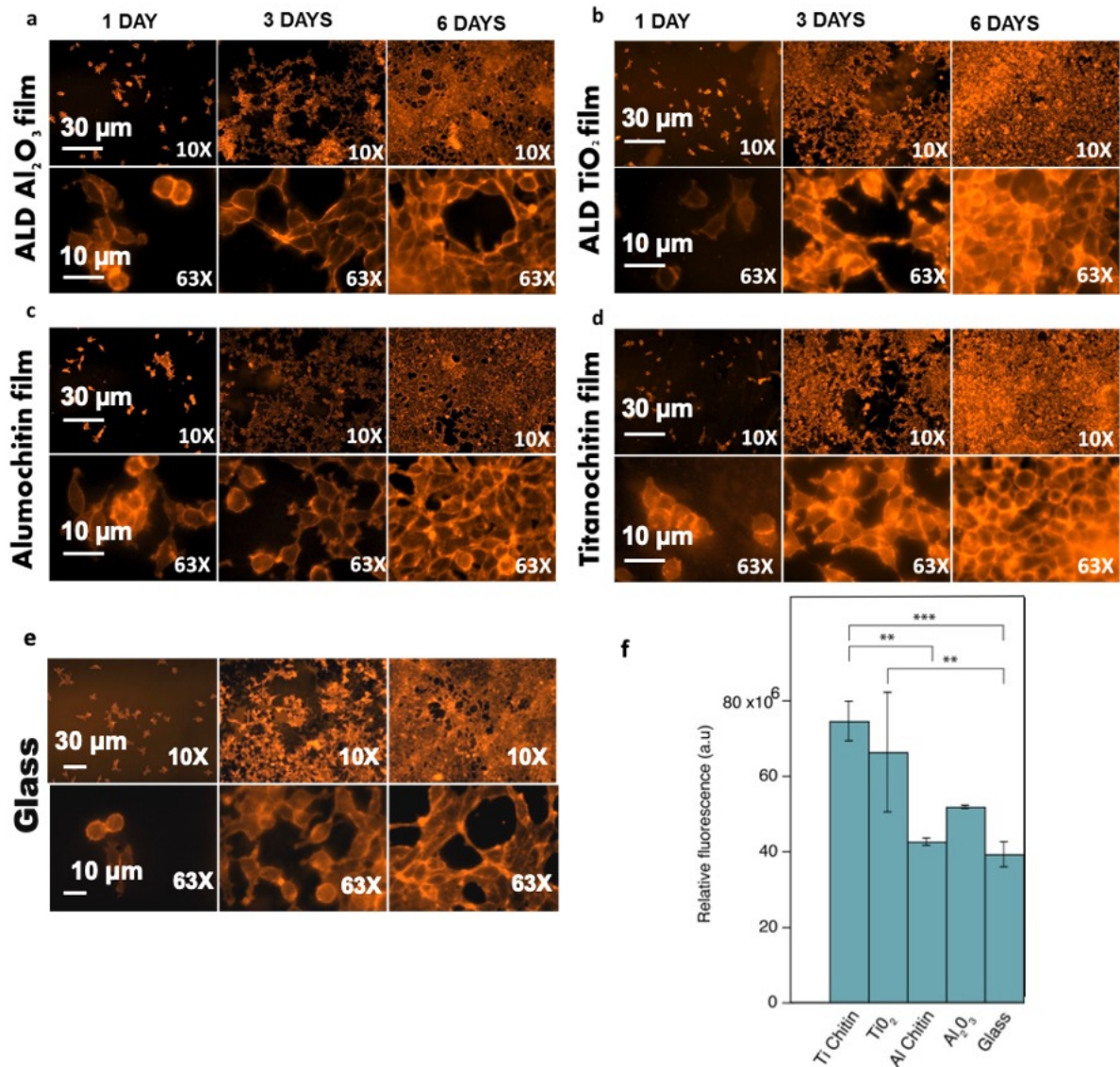


Figure 3.13: Immunostaining and confocal fluorescence microscopy of fibroblast cells on inorganic and hybrid scaffolds. Confocal micrographs of fibroblast cells grown on: (a) inorganic alumina, (b) hybrid alumochitin, (c) a control glass coverslip, (d) inorganic titania, and (e) hybrid titanochitin. (f) Fluorescence intensity calculated from the confocal images of the fibroblast cell proliferation assayed after 3 days of culturing on coverslips coated with the nanofilms. The fibroblasts were seeded on the scaffolds and allowed to grow for 3 days on the respective substrates. Images were taken in original magnification 10x (scale bar= 15 μm) and 63x (scale bar= 4 μm). The cells were stained with CellMask Orange Plasma. All experiments were performed in triplicate (n=3).

This confirms that from the biocompatibility point of view, both metallochitins mimic the biocompatible natural chitin.

3.6.2 Fibroblast cells growth

Cell proliferation assays were also done in vitro with fibroblast cells plated on the surface of alumochitin and titanochitin and compared to the respective alumina and titania surfaces (Figure 3.13, a-e). Glass slides were used as control substrates.

An incubation time of 72 hours was used to calculate the mean fluorescence intensity shown in Figure 3.13 (f).

After 3 days of culturing, inorganic alumina and hybrid alumochitin appeared to be the most favorable surfaces for the adhesion of fibroblast cells. Interestingly, while it is known that ceramic materials, such as alumina and titania, are biocompatible and support fibroblast cell proliferation,¹³²⁻¹³⁴ titanochitin showed even higher biocompatibility than inorganic titania and the control samples.

Fibroblasts do not adhere to rigid hydrophobic or hydrophilic yield surfaces.¹³⁵ Flexible adaptive materials provide better cell adhesion by dynamically tuning their local mechanics, topography, and ligand presentation to adapt to intracellular force generation.¹³⁶ In addition, increased surface stiffness permits increased cell spreading and formation of focal adhesions on flexible, planar surfaces.¹³⁷

The morphology of cells attached to the surface of all test samples throughout the experiment was similar. On all samples the cells have flattened, had a lamellar appearance, were elongated, had a spindle and flat morphology with slender extensions, all being characteristic of fibroblast cells adhered to planar surfaces.¹³⁸⁻¹⁴¹ Moreover, the cells were spread and well attached to all surfaces.

With higher surface roughness the contact area of the cell with the substrate increases and promotes the formation of adhesion points, ensuring healthy cell interaction and stable adhesion and hence higher cell growth and proliferation.¹⁴²⁻¹⁴⁴ The RMS roughness of alumina is twice as high as that of alumochitin, which may be one of the reasons for the slightly higher cell growth on its surface. All test samples possess a contact angle of less than 80 degrees. Since most cells are hydrophilic or superhydrophilic, they tend to spread on a high-energy surface due to the energy gradient between cells surface and substrate.

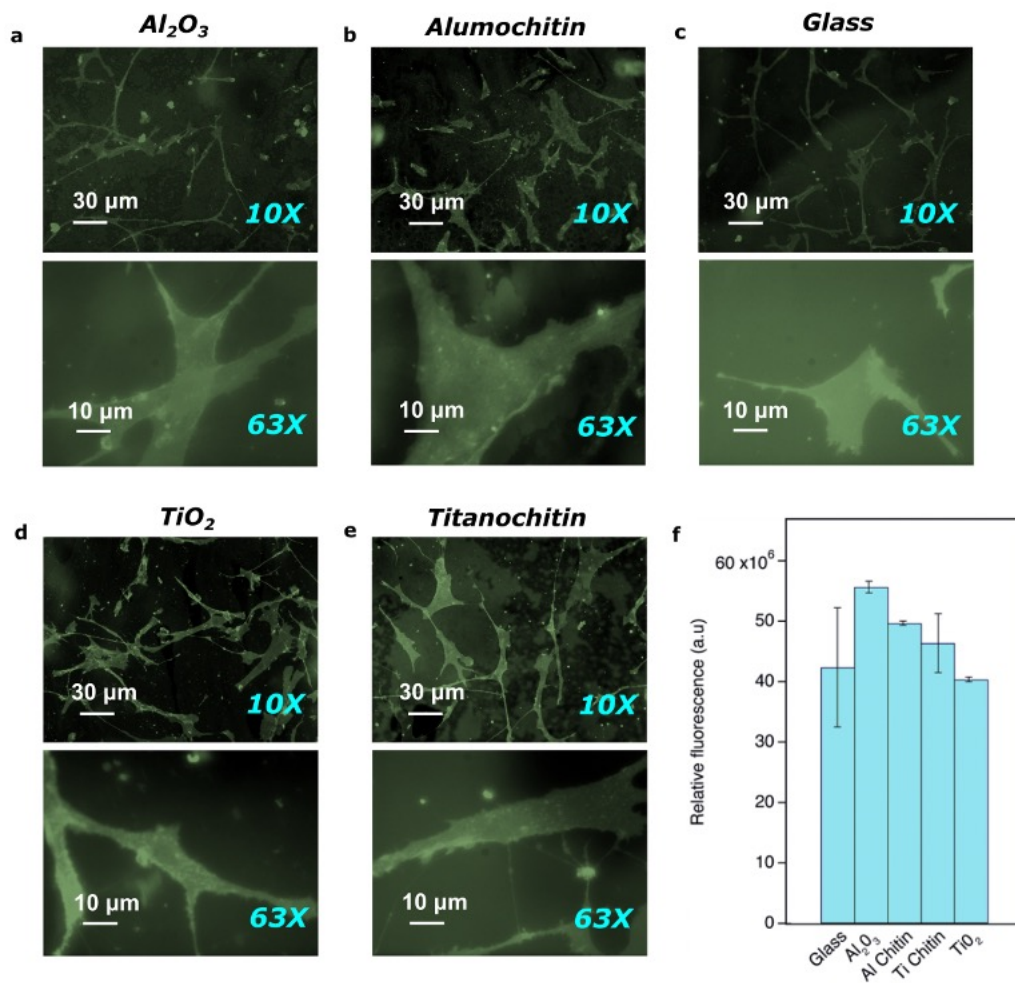


Figure 3.12: Immunostaining and confocal fluorescence microscopy of HEK293T cells: growth and proliferation on inorganic and hybrid scaffolds. Confocal microscopy images of HEK293T cells cultured for 1, 3 and 6 days on (a) inorganic alumina, (b) inorganic titania, (c) hybrid alumochitin, (d) hybrid titanochitin, and (e) glass coverslip as control. The cells are stained with CellMask Orange Plasma. The original magnification was 10x (scale bar= 15 μm) and 63x (scale bar= 4 μm). (f) Calculated fluorescence intensity from the confocal images of the HEK293T cell proliferation, assayed after 6 days of culturing on uncoated glass coverslips (control), on titanochitin and alumochitin or TiO_2 and Al_2O_3 . All experiments were performed in triplicate (n = 3).

The experiments show that alumochitin promotes the proliferation of the fibroblast cell line better than titanochitin, which becomes inverted for the HEK293T cell proliferation.

Thus, the two metallochitins show a certain selectivity/preference depending on the type of seeded cells, which gives opportunities to selectively tune or boost proliferation of certain cells.

Overall, through in vitro investigations of the biocompatibility for HEK293T and human fibroblast cell line, the metallochitins demonstrate a more pronounced ability for simulating the cell proliferation than the positive control samples, which confirms their great biocompatibility.

3.7 Conclusions

In this study, we established a new family of materials, called metallochitins or more generally metallosaccharides, which beneficially combine the characteristics of organic chitinoid polymers and inorganic metal oxides. We have developed a facile, solvent-free vapor phase deposition process based on molecular layer deposition (MLD) to grow the metallochitin films by simply coupling n-acetyl-d-mannosamine (ManNAc) with trimethylaluminum (TMA) or titanium isopropoxide (TTIP). The successful deposition of the alumochitin and titanochitin films was experimentally confirmed. The analysis of the chemical structure of the films showed the formation of C-O-Me bonds for both metallochitins and the presence of C-O-C bonds in the case of the organic chitinoid film. This confirms that the aluminum and titanium are interstitial with the polysaccharide backbone, resulting in a hybrid (poly)metallosaccharide network. The process parameter set for a self-saturating and self-limiting nature of the ManNAc/TMA and ManNAc/TTIP MLD type surface reactions was identified. The very uniform metallochitin films showed great conformality, which allows them to be grown on substrates with complex topologies or high-aspect-ratio structures. The proposed reaction mechanisms for alumochitin and titanochitin growth is also evaluated from the thermodynamic perspective. DFT calculations reveal a detailed understanding of the growth mechanism for this new materials family and confirmed that the proposed reaction mechanism for the ManNAc/TMA and ManNAc/TTIP systems is favorable. Overall, the theoretical data confirm the possibility to grow metallochitin films through a low temperature two-step MLD process from the gas-phase, avoiding the use of any solvents. This first documented use of a saccharide as vapor phase reactant is a showcase for the expansion of the toolbox of processes and materials that can be grown by MLD and is also a foundation for the fabrication of various saccharide-based thin films, which turns out to be a materials family with enormous potential in plenty application fields.

The *in vitro* evaluation of the antimicrobial activity of the metallochitin films against gram-positive (*Staphylococcus aureus*, *S. aureus*) and gram-negative (*Escherichia coli*, *E. coli*) bacteria was assessed. Alumochitin acted antimicrobially by inhibiting the adhesion of both types of bacteria, which ultimately suppresses biofilm formation. Interestingly, titanochitin had a selective antimicrobial activity against gram-negative bacteria, but allowing the formation of gram-positive bacterial biofilms. The origin of the antimicrobial activities may lie in the surface charge, roughness, wettability, and substrate chemistry, all of which can have impact on the attachment and interaction of the bacterial strains with the substrate. The different behavior of both metallochitins against both types of bacteria is likely caused by the more positive zeta potential and thus surface charge of alumochitin in comparison to titanochitin and the more negative charge of gram-negative bacteria in comparison to the gram-positive bacteria, which suggests a weaker electrostatic interaction of titanochitin with *S. aureus* bacteria and consequently a lower tendency of physical disruption of the cell wall. Furthermore, the thicker cell wall and the absence of an outer cell membrane in *S. aureus* contribute to its stabilization. Eventually, the antibacterial activity of the two tested metallochitins differs to each other, which is a very intriguing point as it grants enormous application potential for the design and development of selective antimicrobial surfaces. Importantly, the functional groups thought to be responsible for the antimicrobial activity were conserved during the MLD synthesis.

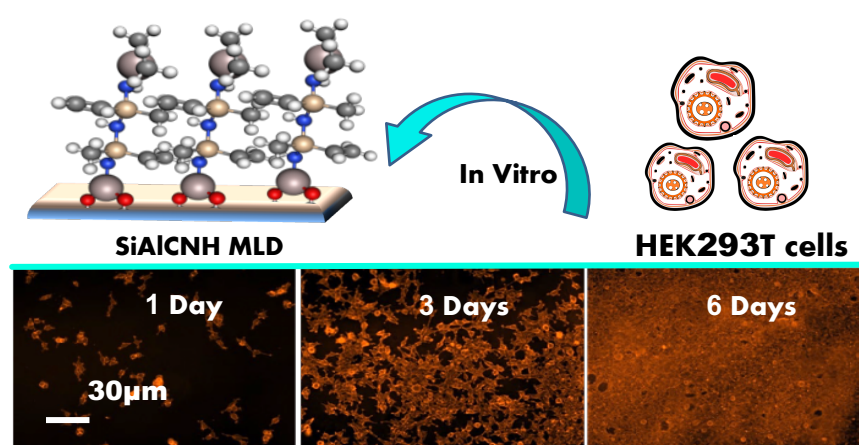
The biocompatibility of metallochitins was characterized *in vitro* by culturing human embryonic kidney (HEK293T) and human fibroblast cells on the metallochitin films, focusing mainly on their attachment and proliferation. The concerted effect of surface roughness, wettability and chemistry on the cellular behavior was examined. Both metallochitins showed higher cell proliferation than the uncoated coverslips that were used as reference samples and in both cell investigations. Titanochitin showed an even higher biocompatibility than the corresponding titania, which is well known for being extraordinarily biocompatible. This effect may stem from a synergy between chitin and titania which are both simultaneously present in the titanochitin hybrid film.

In summary, our results demonstrate that the developed hybrid metallochitins act as versatile biomaterial, being an excellent mimic of natural chitin, stimulating the cell growth and proliferation while simultaneously preventing the adhesion of bacteria, even selectively for gram-positive or gram-negative strains. Metallochitins are a new class of materials and offer a pathway for the design of future multifunctional biomaterials with selectivity in prevention of bacterial attachment and cell proliferation. Together with the fact that the metallochitins are composed of natural saccharides and not based on fossil sources and they are biodegradable, this makes them uniquely suitable as sustainable and functional materials attractive for biomedical applications such as tissue engineering, biomedical devices, implants, filtration units, and other applications.

Chapter 4

Biocompatible Silicon-Based Hybrid Nanolayers for Functionalization of Complex Surface Morphologies

Silicon-based polymers show great promise for various applications in biomedicine, nanotechnology, tissue targeting and drug delivery. The use of such materials as functional coatings on surfaces requires the development of strongly adhering and flexible conformal films, which is challenging for conventional wet-chemical coating techniques. We have developed a facile, solvent-free Molecular Layer Deposition (MLD) process to grow environmentally stable hybrid aluminosilazane thin films. Exceptionally good biocompatibility is testified with significantly higher proliferation of Human Embryonic Kidney (HEK293T) cells than that on glass, which was used as reference. Such highly biocompatible and conformal films show great promise as functional coatings for scaffolds or implantable devices with complex topologies or high-aspect-ratio structures.



The work described in the present chapter is published in the journal Applied Nano Materials from the American Chemical Society (ACS). Graphs, figures and parts of the text of the publication are reused in this thesis with permission of the publisher. ¹⁰²

Article:

Biocompatible Silicon-Based Hybrid Nanolayers for Functionalization of Complex Surface Morphologies. Ka. Ashurbekova, Kr. Ashurbekova, B. Alonso-Lerma, I. Šarić, L. Barandiaran, E. Modin, M. Petravić, R. Perez-Jimenez and M. Knez. ACS Applied Nano Materials 2022 5 (2), 2762-2768.

4.1 Introduction

For tissue engineering, scaffolds are needed which fulfill various criteria. Those include biocompatibility, facile processing to obtain desired shapes, non-toxicity, tailoring of wetting properties, etc., all of which important pre-requisites for promoting tissue growth. Organosilicon-based hybrid polymers, such as polysiloxanes and polysilazanes, combine the typical properties of polymers and ceramics in a remarkable way and are therefore frequently discussed in the context of applied biomaterials. Most of them are chemically inactive, insoluble, largely corrosion-resistant, mechanically rigid, and thermally stable, while being non-toxic. All these attributes are crucial for applications in medicine and biomedical MEMS (BioMEMS) technology, which is why those materials found their home in a wide range of electrical, optical, and biomedical applications.^{145, 146, 147}

For most applications the surface functionality of a material is of critical importance, as this is the fraction of a material that interacts with the surrounding. Therefore, tailoring the surface functionality of a material for an appropriate interaction with the surrounding environment is a key factor. As scaffolds for tissue engineering can be flexible and shaped to micro- and nanostructures, a high degree of flexibility for a surface functionalization of scaffolds is demanded. However, despite a considerable effort in ongoing research, the tailoring of surface functionalities of a material, that improve cell attachment and cell proliferation while at the same time showing a wide range of variable physicochemical and mechanical properties, still poses a great challenge for the researchers.¹⁴⁸

ALD is a technique based on self-limiting surface chemistry which allows depositing a variety of inorganic thin film materials from the vapor phase. Typically, ALD films are grown from two or more vaporized inorganic precursors.¹⁴⁹ When the inorganic precursors are replaced with vaporized organic molecules, the resulting films will be polymers or, in the case of a mixed use of organic and inorganic precursors, hybrid organic-inorganic materials, with often unexpected characteristics. The variant of ALD which includes organic precursors is commonly known as MLD.^{150, 151} Similar to ALD, MLD offers exceptional conformality on high aspect ratio structures and enables a good control over the composition and the thickness even down to monolayers. Such films are lately intensely explored and can be used in a wide variety of applications as summarized in several review articles.^{152, 6}

The chemistry of organic reactions is often more complex and variable than that of inorganic reactions and therefore concepts for a polymer coating by MLD must be carefully evaluated. Among the reaction schemes the ring-opening reaction is very

promising for enabling the growth of new MLD films. Ashurbekova et al recently reported the first example of a ring opening vapor to solid polymerization of cyclotrisiloxane (V_3D_3) and N-methyl-aza-2,2,4-trimethylsilacyclopentane by MLD.¹⁵³ After this polymer growth, the authors demonstrated the ring-opening MLD of an organic–inorganic hybrid alumosiloxane thin film from 2,4,6,8-tetramethyl-2,4,6,8-tetravinylcyclotetrasiloxane (V_4D_4) and trimethylaluminum (TMA).¹⁵⁴ Those alumosiloxane films showed an extremely low leakage current density (lower than $5.1 \times 10^{-8} \text{ A cm}^{-2}$ at $\pm 2.5 \text{ MV cm}^{-1}$), a dielectric constant (k) of 4.7, and a good thermal stability upon calcination at 1100 °C. A radical-initiated cross-linking of the hybrid alumosiloxane thin film in a layer-by-layer manner enhanced the stability of the film.

155

As mentioned earlier, functional thin films have a high application potential in biomedicine and tissue engineering, if they are rendered bioactive. Bioactive organic–inorganic hybrid MLD films have been reported in few studies, mostly by the group of Ola Nilsen.^{156,157} They fabricated organic–inorganic hybrid coatings by linking titanium with the nucleobases thymine, uracil or adenine, and successfully tested the bioactivity of these films by analyzing the immunofluorescence, cell attachment, proliferation, and viability of rat conjunctival epithelial goblet cells.

In the present work, we introduce hybrid alumosilazane thin films as a new materials group that can be grown by MLD. The developed process is based on a sequential surface reaction between trimethyl-trivinylcyclotrisilazane (V_3N_3) and TMA. We analyzed the growth and characterized the resulting hybrid polymer film. The biocompatibility of the film was assessed by growing HEK293T cells atop and comparing with the growth on glass. We further compared the cell growth on the hybrid silazane film with that on the corresponding hybrid siloxane film, which was also grown by MLD.

4.2 Experimental details

Sample fabrication

The MLD was performed in a commercial ALD reactor (Savannah S100, Cambridge NanoTech Inc.). The MLD experiments were carried out at reactor temperatures ranging from 150 to 220 °C. The deposition was carried out at 200 °C under a constant nitrogen gas flow of 20 standard cubic centimeters per minute (sccm). 2,4,6-trimethyl-2,4,6-trivinylcyclotrisilazane (V_3N_3) (95% purity) and trimethylaluminum (TMA) (97% purity) used as received from Sigma-Aldrich. TMA was kept at room temperature throughout the deposition. 2,4,6-trimethyl-2,4,6-trivinylcyclotrisilazane (V_3N_3) was

heated to 80 °C to increase the vapor pressure. The two-step process had a sequence of 7/25/2/25 (in seconds), where 7 and 2 s were V₃N₃ and TMA dose times, respectively. Excess precursor was removed by purging the chamber with nitrogen flow for 25 s. Silicon wafers with dimensions of 1 × 1 cm were used as the substrates for the ex-situ analysis of films grown at different conditions.

Testing of the film's stability

The stability of the deposited films in the cell medium was tested by measuring the thickness of the deposited film before and after an immersion into the medium. For that, a film was grown on a silicon substrate and its thickness was measured by x-ray reflectivity (XRR) before and after immersion for 1 day, 3 days and 6 days. After 6 days of immersion, the samples were thoroughly rinsed with water, dried with compressed air, and the thickness and composition of the films was determined. ATR-FTIR analysis of the films, deposited on ZrO₂ nanoparticles before and after exposure to the cell medium solution, was performed to reveal changes in the film composition.

Characterization of the films

In-situ quartz crystal microbalance (QCM) measurements were performed as described previously.¹⁵⁴

The morphologies of the deposited MLD films were studied using High-resolution transmission electron microscopy (HRTEM) using a Cs-corrected microscope FEI Titan (ThermoFisher, U.S.A.) in monochromated mode at 80 kV.

X-ray Reflectivity (XRR) was performed using PANalytical X'Pert Pro diffractometer with Cu K α radiation.

Fourier transform infrared (FTIR) spectroscopy was performed in attenuated total reflectance mode with a diamond plate using a PerkinElmer Frontier spectrometer. MLD films were deposited onto pressed nanopowder of ZrO₂ (Sigma-Aldrich, particle size <100 nm). Spectra were taken using 20 scans at 4 cm⁻¹ resolution in the range from 600 to 4000 cm⁻¹.

X-ray photoelectron spectroscopy (XPS) analysis of the MLD films deposited onto a Si (100) substrate was performed using a SPECS instrument, equipped with a hemispherical electron analyzer and a monochromatized source of Al K α X-rays. The XPS spectra were deconvoluted into several sets of mixed Gaussian–Lorentzian functions with Shirley background subtraction.

In vitro biocompatibility tests

HEK293T cells culture experiments were performed as described previously.¹⁰³ The cells were dyed with CellMask Orange Plasma membrane stain, diluted in PBS, after washing each sample three times with PBS. After 5 min of incubation, the cells were observed by confocal microscopy.

4.3 Results and discussion

4.3.1. Fabrication and Characterization of the MLD Films

The scheme of the sequential chemical reactions of the MLD process is shown in Figure 4.1 (a). The process is based on sequential surface reactions between V_3N_3 and TMA. In step (A), an aluminum-methylated surface is being exposed to V_3N_3 vapor which leads to the opening of the V_3N_3 ring with the formation of an Al-NH-Si bond.

The dosing of TMA vapors in stage (B) of the process leads to a rupture of some of the Si-NH-Si bonds, regenerating the aluminum-methylated surface groups. In principle, any of the Si-N bonds can be attacked by TMA, thus the scheme shows an idealized scenario. With a high density of the V_3N_3 on the surface, it is likely from the sterical point of view that the topmost, better accessible bonds will be attacked. Repetition of the MLD cycle, consisting of V_3N_3 and TMA surface reactions, will build up an organic/inorganic SiAlCNH film.

To understand the growth process, we performed in-situ Quartz Crystal Microbalance (QCM) studies of the film growth at 200°C. The QCM results, showing the mass gain versus V_3N_3 and TMA exposure, are displayed in Figure 4.1, b. The timing sequence (in seconds) for the V_3N_3 exposure was (X, 25, 2, 25), where 2 s is the fixed TMA dosing time, 25 s is the purge time, and X is the variable V_3N_3 dosing time. The timing sequence used for the TMA saturation experiment was (7, 25, X, 25), where 7 s is the fixed V_3N_3 dosing time. At 200 °C, the mass gain per cycle (MGPC) reaches a saturation of 18 ng/cm² at 7 seconds of V_3N_3 and 2 seconds of TMA dosing times, showing that both surface reactions are self-limiting. Consequently, the timing sequence of (7/25/2/25) was used for further experiments to fulfill the self-saturation condition for the studied MLD processes.

The QCM mass change vs. time of the SiAlCNH film growth during 18 MLD cycles is shown in Fig. 4.1 (c). In-situ monitoring of the process showed a reproducible and linear increase of the film mass with an increasing cycle number. An enlarged view of

the QCM signal in the linear growth regime is shown in the inset of Figure 4.1 (c). The V_3N_3 dose leads to a mass gain of 7 ng/cm^2 , and the TMA dose to 11 ng/cm^2 . Figure 4.1, d shows the temperature dependence of the MLD growth of V_3N_3 /TMA, studied in-situ with a QCM in a temperature range between 150°C and 220°C . The highest mass gain per cycle (MGPC) was 18 ng cm^{-2} at 200°C and the lowest was 15 ng cm^{-2} at 150°C .

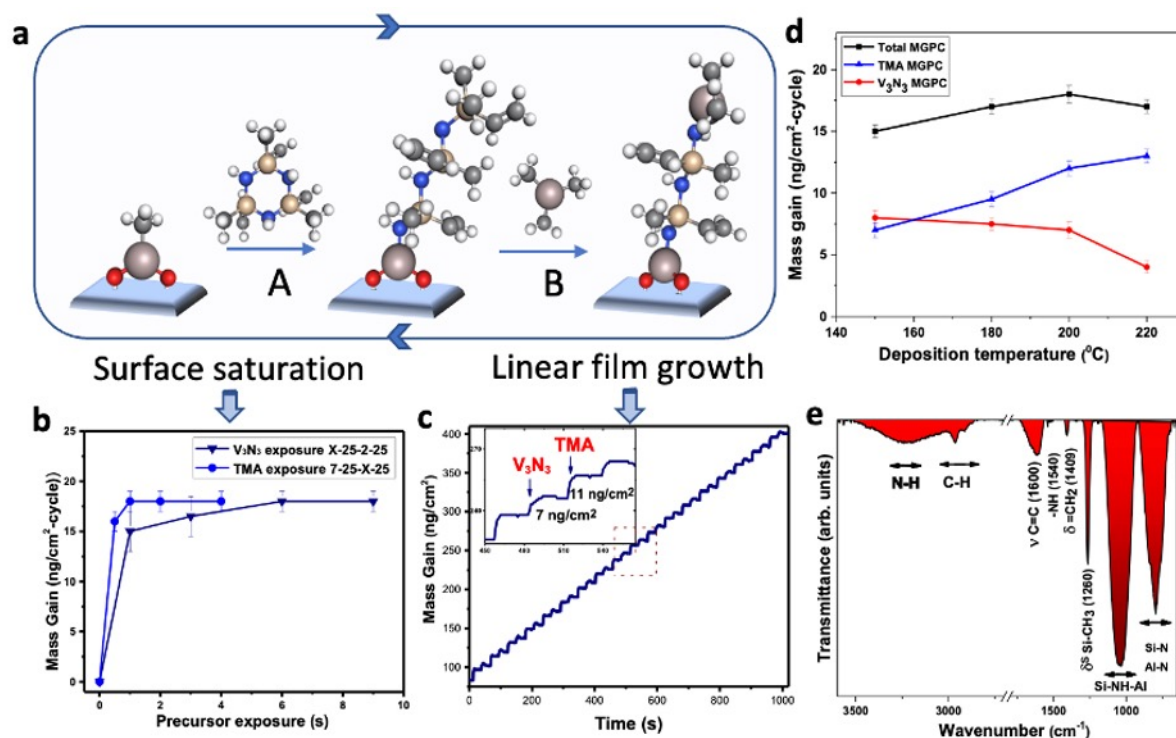


Figure 4.1: Thin film fabrication and process characterization. (a) Idealized schematic of the surface chemistry of a SiAlCNH thin film growth by MLD. (b) QCM mass gain per cycle vs. V_3N_3 (dark blue) or TMA (light blue) dosing times in a steady state regime at 200°C . (c) QCM measurements of the mass gain vs. time for the V_3N_3 /TMA MLD process on a pre-deposited Al_2O_3 ALD surface at 200°C . Inset: Expanded view of the growth during four reaction cycles in a steady state at 200°C . The growth was monitored over 40 reaction cycles using a pulse-purge timing sequence of 7/25/2/25 (in seconds) for $V_3N_3/N_2/TMA/N_2$, respectively. (d) Mass gain per cycle (MGPC) vs. deposition temperature of the alumosilazane MLD process. (e) ATR-FTIR spectrum of the V_3N_3 /TMA MLD film.

Figure 4.1 (e) shows the ATR-FTIR spectrum of a 27 nm thick SiAlCNH MLD film, deposited at 200°C . The strongest peak at 1025 cm^{-1} is attributed to Si-NH-Al stretching vibrations.¹⁵⁸ The presence of NH groups is confirmed with the N-H bending

vibration at 1540 cm^{-1} and the symmetric stretching vibration of the secondary amino group at 3270 cm^{-1} .¹⁵⁸ The signals at 1260 cm^{-1} , 1409 cm^{-1} , and 1600 cm^{-1} are assigned to symmetric Si-CH₃ bending, planar CH bending in =CH₂, and C=C stretching vibrations, respectively.^{159,160} This indicates that the functional vinyl and methyl groups in the cyclosilazane molecule do not undergo changes during the film growth, which is consistent with the proposed MLD scheme. The detailed assignment of all IR signals in the spectrum of the SiAlCNH film and references are shown in Table 5.

The thicknesses of the films were measured by XRR of films deposited on Si (100) wafers with a native SiO₂ layer. The resulting growth rate of the SiAlCNH film at 200 °C was 1.3 Å /cycle. High-resolution TEM imaging was performed for determination of the structure and conformality of the SiAlCNH films. Figure 4.2 (a,b) shows TEM images of ZrO₂ nanoparticles coated with a 5 nm SiAlCNH MLD film in two different magnifications.

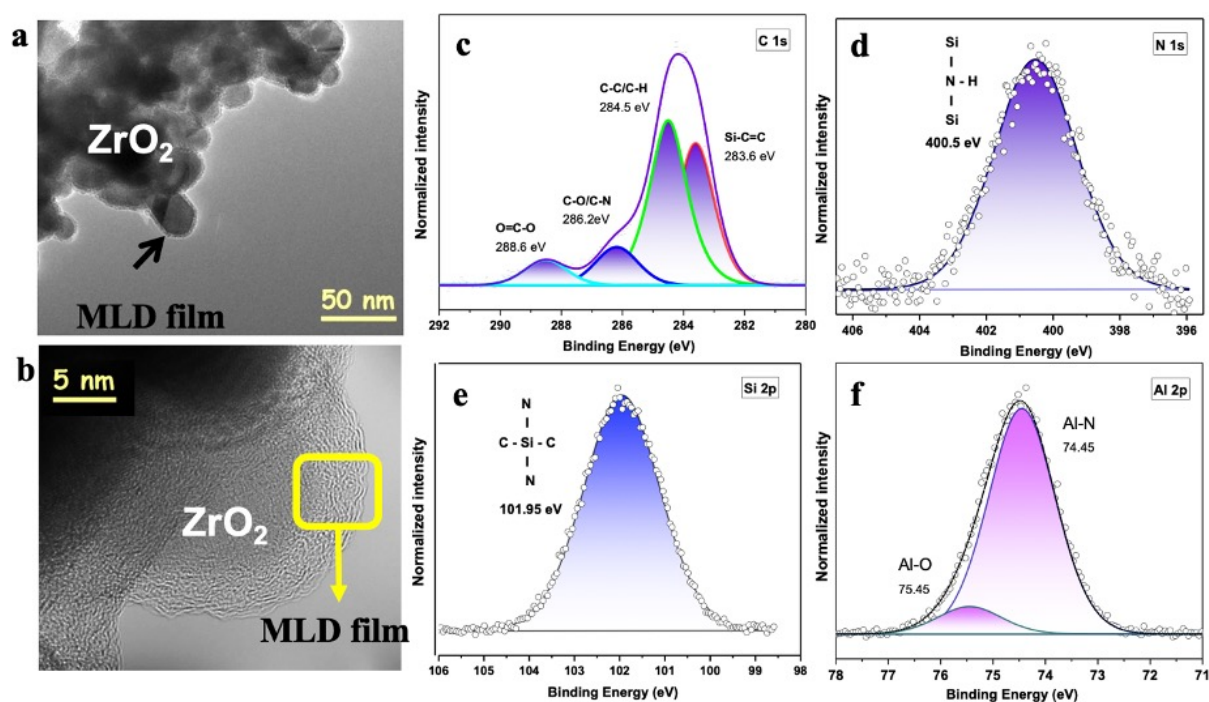


Figure 4.2: Analysis of the film conformality and structural changes. (a) TEM image of ZrO₂ NPs coated with a 5 nm thick MLD film, grown from V₃N₃/TMA by MLD at 200 °C. (b) Magnified image of the same sample. (c), (d), (e), (f), High-resolution XPS spectra, obtained from a 27 nm thick MLD film, of C 1s, N1s, Si 2p and Al 2p core levels, respectively. The spectra were recorded on a Si (100) substrate, after MLD at 200 °C.

The micrographs show a highly conformal and homogeneous SiAlCNH film wrapping the zirconia surface. The micrograph with a higher magnification in Fig. 4.2, (b) shows the amorphous nature of the film.

For evaluating the bonding situation, we performed high-resolution XPS on a 27 nm thick SiAlCNH film, deposited at 200 ° C on a Si (100) substrate with a native SiO₂ layer, and the obtained spectra of C 1s, N 1s, Si 2p and Al 2p core levels are shown in the Fig. 4.2.

Sets of mixed Gaussian and Lorentzian functions were used for fitting the XPS spectra. Background subtraction was carried out according to the Shirley method. The C 1s spectrum in Fig. 4.2 (c) was deconvoluted into four components, corresponding to the binding energies of 283.6 eV, 284.5 eV, 286.2 eV and 288.4 eV and are assigned to Si-C = C, C-C / C-H, C-O/CN and O-C = O (surface contamination) chemical states of carbon in the film. The N 1s spectrum in Fig. 4.2 (d) shows a single component at the energy of 400.5 eV which is associated with the Si-NH-Si chemical state of nitrogen in the film. This also stands in agreement with the proposed deposition scheme in Fig. 4.1 (a) and shows that the state of the N in the film is not altered with the MLD process. The Si 2p spectral region in Fig. 4.2 (e) is also characterized by a single peak at 101.96 eV which is assigned to the SiN₂C₂ bonding state of Si within the MLD film. Two components in the Al 2p spectrum in Fig. 4.2 (f) are assigned to the presence of Al-N and Al-O bonds. Given that the sample was exposed to air after the growth process and before XPS measurement, presence of some Al-O species on the surface can't be excluded due to the oxidation of some of the Al-N bonds on the surface of the film.¹⁶¹

4.3.2 Stability of Alumosilazane and Alumosiloxane MLD films

Stability is a critical issue for many MLD-grown films. We studied the stability of the synthesized hybrid alumosilazane and alumosiloxane MLD samples which we grew 2 years earlier, and which were exposed to ambient air since. The resulting high-resolution XPS spectra of the alumosiloxane MLD film (around the C 1s, Si 2p, and Al 2p core-level regions) and a 24 nm alumosilazane MLD film (C 1s, N 1s, Si 2p, and Al 2p core-level regions) after 2 years of exposure to air, are shown in Figure 4.3 and Figure 4.4, respectively.

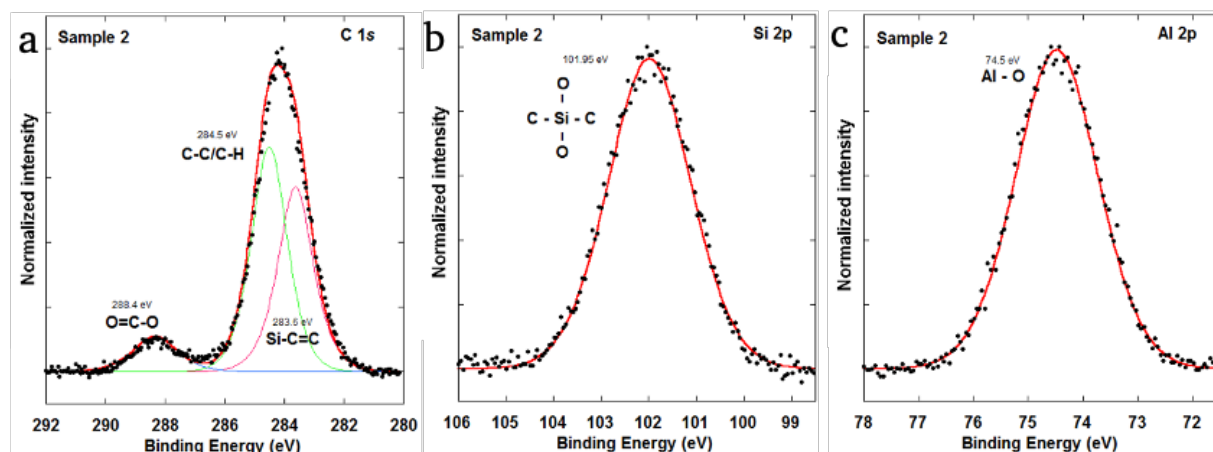


Figure 4.3: High-resolution XPS spectra of (a) C 1s, (b) Si 2p, and (c) Al 2p core levels of an alumosiloxane MLD film after 2 years of exposure to air. The film was deposited at 200 °C on a Si (100) substrate.

The XPS spectra measured before exposure to air (Figure 4.2, c-f) look nearly identical with the newer spectra and confirm a very high stability of both investigated MLD films in air over long periods of time.

We observed only a slight increase of the full width at half maximum (FWHM) values in Al 2p, Si 2p and N1s for both MLD samples after 2 years of exposure to air (Tables 5 and 6). The broader peaks indicate an expected continued oxidation of the Al, Si, and N over time, which is, however, not affecting the integrity of the hybrid layer.

Table 5: FWHM values of the Al 2p, N1s and Si 2p core levels measured from the high-resolution XPS spectra of the alumosilazane MLD film.

V_3N_3 sample	Measurement 2020: FWHM (eV)	Measurement 2022: FWHM (eV)
Al 2p	1.8	1.9
Si 2p	2.1	2.2
N 1s	3.0	3.1

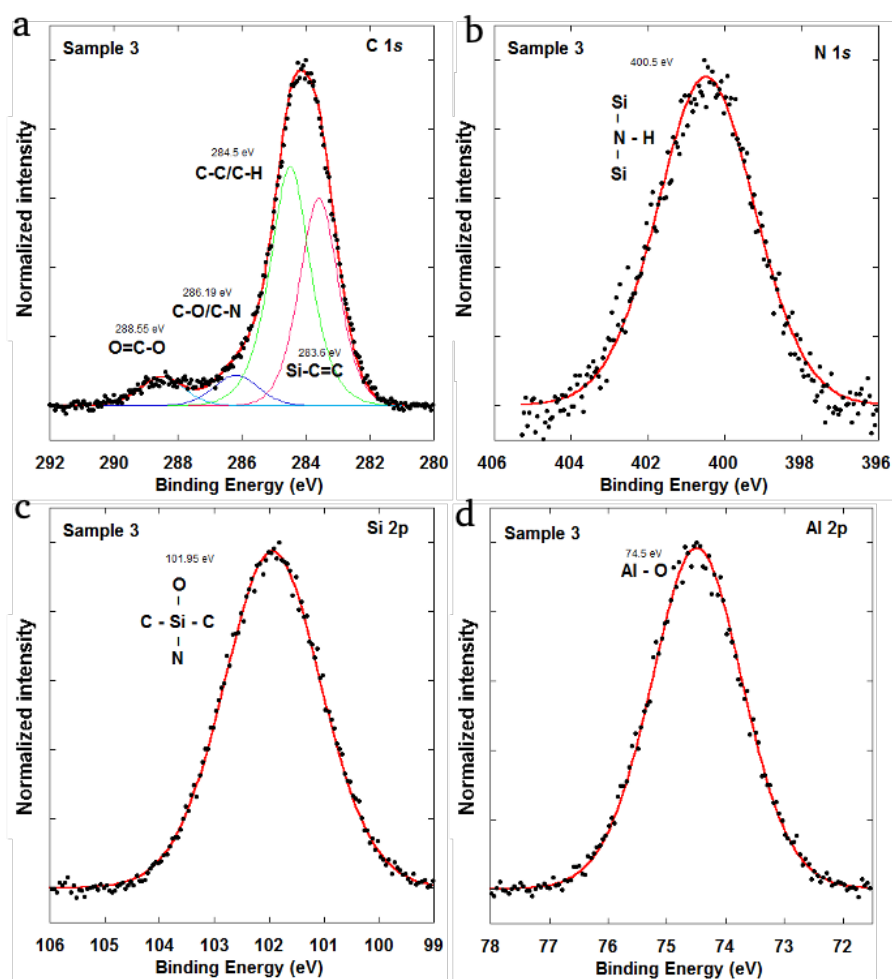


Figure 4.4: High-resolution XPS spectra of an alumosilazane MLD film of (a) C 1s, (b) N 1s, (c) Si 2p, and (d) Al 2p core levels after 2 years of exposure to air. The film was deposited at 200 °C on a Si (100) substrate.

Table 6: FWHM values of the Al 2p and Si 2p core levels measured from the high-resolution XPS spectra of the alumosiloxane MLD film.

V ₄ D ₄ sample	Measurement 2020:	Measurement 2022:
	FWHM (eV)	FWHM (eV)
Al 2p	1.8	1.9
Si 2p	2.0	2.1

Prior to the biocompatibility evaluation of the alumosilazane and alumosiloxane MLD films, we tested their stability in the cell medium solution.

We immersed the samples into the medium for 1, 3 and 6 days, thereby keeping the conditions identical as for the in vitro biocompatibility testing. Subsequently, the film composition and thickness were studied. XRR measurements were conducted to determine the film thicknesses before, during and after immersion.

Figure 4.5 shows the plot of the measured thickness values versus the sample immersion time in the cell medium solution.

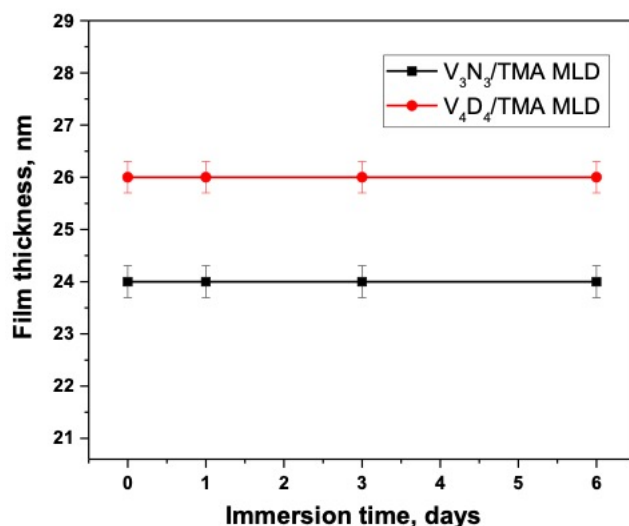


Figure 4.5: XRR film thickness of alumosilazane and alumosiloxane MLD films versus immersion time in the cell medium solution.

The plot shows that no change in the film thickness occurred even after 6 days of exposure to the medium, which strongly suggests great stability of the tested films in the immersed solution. XRR measurements confirm that there is no change in the SiAlCNH and SiAlCOH MLD films thickness even after 6 days of immersion into the medium, which strongly suggests great stability of the tested films in the medium.

ATR-FTIR spectra of the alumosilazane MLD film before and after exposure to the cell medium solution for 3 and 6 days are shown in Figure 4.6. The spectra show no significant changes in the MLD film after immersion into the cell medium. All characteristic peaks remained present even after 6 days of immersion, additionally confirming its good stability even in solution.

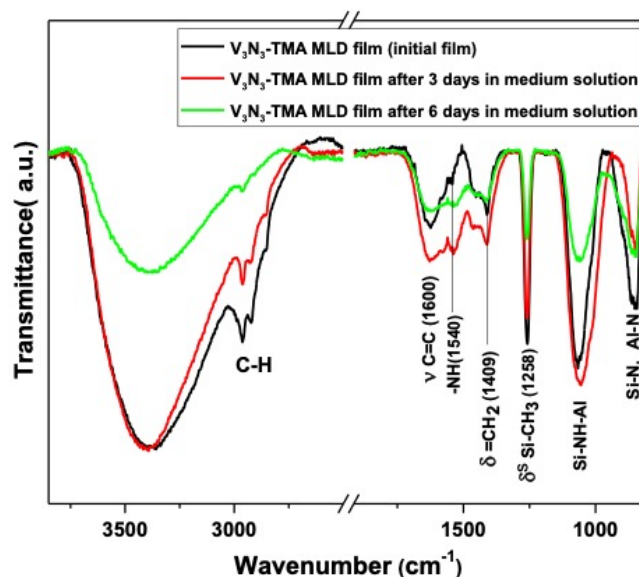


Figure 4.6: ATR-FTIR spectra of the V₃N₃/TMA MLD film after deposition (in black), after 3 days (red) and after 6 days (green) of immersion into the cell medium solution. The 24 nm thick film was deposited at 200°C on pressed ZrO₂ particles.

The detailed assignment of all IR signals in the spectrum of the SiAlCNH film and references are shown in Table 7.

Table 7: ATR-FTIR peak assignments for the SiAlCNH MLD film.

ν , (cm ⁻¹)	Chemical bond/ vibration modes	Reference
800	Si-C, CH ₃	159,160,162
841	Si-N / Al-N stretching, CH ₃ deformation	159,160,162
1025	Si-NH-Si stretching vibrations	158,159
1260	Symmetric Si-CH ₃ bending	159,160,162, 158
1409	Planar CH bending in =CH ₂	159
1540	N-H bending vibration	158
1600	C=C asymmetric stretching vibrations in vinyl	158,159

2913	CH ₃ , symmetric	158~160,162
2964	CH ₃ asymmetric stretch	159
3270	Symmetric stretching vibration of the NH	158

Furthermore, the density of the alumosilazane hybrid film lies between those of alumina and polydimethylsiloxane (PDMS), which could be one of the reasons for the observed exceptional stability. The density and root mean square (RMS) roughness of the alumosilazane film, deposited at 200 ° C, were 2.2 g / cm³, and 5.2 Å, respectively. For comparison, Al₂O₃, grown by ALD at similar processing temperatures, has a density of about 3.0 g / cm³, while the density of PDMS is 1.1 g / cm³.

In conclusion, both XRR and ATR-FTIR data show that the films are exceptionally stable in the cell medium, confirming the reliability of the obtained results on their biocompatibility.

The barrier performance of siloxane-alumina hybrid organic-inorganic thin films synthesized on Polyethylene naphthalate (PEN) substrate by MLD with tetramethyl-tetra-vinylcyclotetrasiloxane (V₄D₄) and trimethylaluminum (TMA) as precursors, was evaluated. The WVTRs were measured using the mentioned above Gintronic method. For the formation of the thin film, the substrate plays a crucial role, as the functional groups in the polymer may enable or hinder thin film growth. For the deposition of a barrier layer on PEN, it could be useful to use a preconditioning of the surface to enable or enhance the growth. We performed a surface modification of PEN using an oxygen plasma treatment. Regarding the studies in the literature, the surface oxidation results in the formation of various types of chemical bonds between the carbon and the oxygen, e.g., C=O, O-C-O, O-C=O and -C(=O)-O-C(=O)-. For a 23 nm thick SiAlCOH film on a PEN substrate we obtained a WVTR of 0.32 g/(m² day), which is more than 2 times lower than the WVTR of uncoated PEN.

4.3.3 Analysis of In-Vitro Biocompatibility

Assessment for Human Embryonic Kidney

(Hek293T) Cells

For testing the biocompatibility of the coatings, we grew Human Embryonic Kidney (HEK293T) cells on SiAlCNH and on the corresponding hybrid organosilicon alumosiloxane (SiAlCOH) MLD film for comparison.

The confocal micrographs in Fig.4.7 show that the HEK293T cells adhered to both MLD substrates and proliferated well.

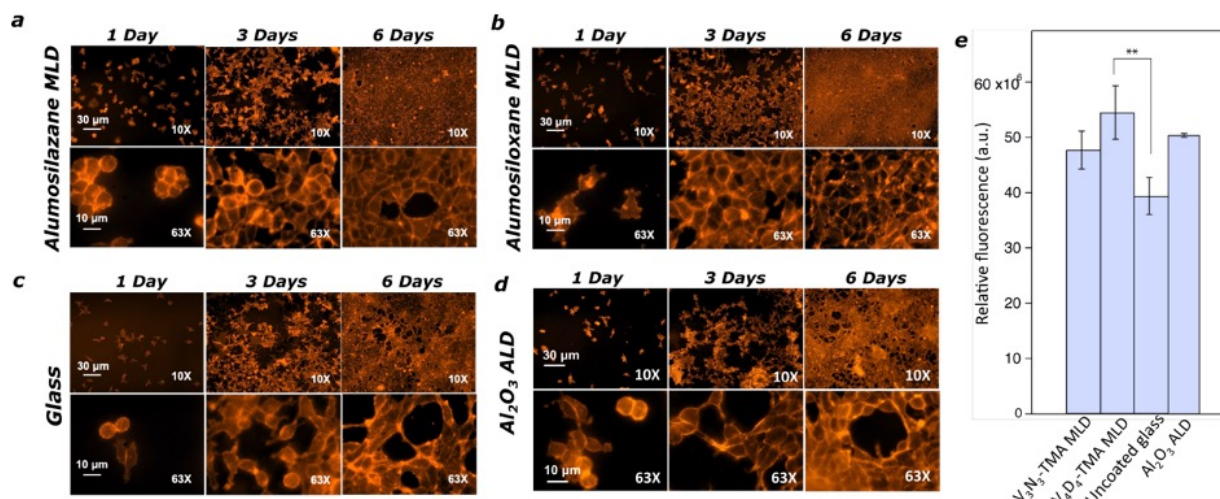


Figure 4.7: Biocompatibility evaluation. Confocal microscopy images of HEK (Human Embryonic Kidney) 93 cells, cultured for 1, 3 and 6 days on (a) MLD V₃N₃-TMA (SiAlCNH), (b) MLD V₄D₄-TMA (SiAlCOH), (c) control uncoated glass coverslips, and (d) ALD-Al₂O₃. The cells were stained with CellMask Orange Plasma. The magnification is 10x (scale bar = 30 μm) and 63x (scale bar = 10 μm). (e) Fluorescence intensity calculated from the confocal images of the HEK293T cell proliferation assayed after 6 days of culturing on uncoated glass coverslips (control), alumosilazane (V₃N₃), alumosiloxane (V₄D₄), and ALD-Al₂O₃ substrates.

A uniform and coherent biofilm formed on both substrates after 6 days of seeding. The observed shapes and dimensions are characteristic of the HEK293T cell line.

In essence, both MLD substrates enhanced the proliferation of HEK293T cells compared to uncoated coverslips which served as positive control (Fig. 4.7, c). The fluorescence intensities were calculated after 6 days of culturing on alumosilazane and alumosiloxane MLD-coated substrates and are shown in Fig. 4.7 (e).

The number of cells grown on both MLD films is higher than that on neat coverslips, confirming an excellent support of the MLD films for HEK293T cells proliferation. The number of cells grown on ALD-Al₂O₃ is comparable to that on MLD alumosilazane, whereas the proliferation of HEK293T cells on MLD alumosiloxane is higher, suggesting some advantage of the oxide-based hybrid film over inorganic alumina for cell proliferation. The calculated fluorescence intensity in Fig. 4.7 (e) shows a higher concentration of cells on the alumosiloxane SiAlCOH than on the alumosilazane SiAlCNH MLD film after 6 days of culturing. To examine the difference in cellular

response between the tested two MLD films, we compared several physicochemical properties that can affect cell adhesion, growth, and proliferation. Commonly the most importance is assigned to the surface chemistry, wetting properties, contact angle hysteresis, and roughness of the substrate, which all can alter a material's biocompatibility.^{163,164}

The two materials investigated in this work have a different chemical composition and, accordingly, different surface functionalities. The hybrid alumosiloxane MLD substrates contain inorganic Al-O. The biocompatibility of inorganic alumina (Al_2O_3) ceramic is well known, and the material is widely used for medical devices.¹⁶⁵ The alumosilazane films contain Al-N. Pure inorganic AlN is biocompatible and therefore has been used in implantable biomedical devices.^{166,167}

The surface roughness is another factor that may affect adhesion and regulate the function and behavior of cells and proteins.^{168,169,164} However, both MLD films were ultrasmooth with an RMS roughness below 1 nm, which excludes any impact of the surface roughness on the observed difference in the proliferation.

The wetting properties can also significantly affect cell attachment and spreading. Interestingly, the wettability affects the adhesion of different types of cells to the surface differently.^{170 168} For fibroblast cells, for example, it has been shown that hydrophilicity leads to strong cell adhesion whereas hydrophobicity leads to the weaker cell adhesion, which can be further impacted by the surface charge.¹⁷¹ Osteoblast cells showed a similar trend.¹⁷² In extreme circumstances, that is, super-hydrophilic (with a contact angle of less than 5°) and super-hydrophobic surfaces (with a contact angle of more than 150°), no cell attachment and growth occurs.¹⁷³ It was also observed that cells spread much more widely on hydrophilic surfaces than on hydrophobic surfaces.¹⁷² In our study, both films had a low contact angle hysteresis. The alumosiloxane (SiAlCOH) MLD film had a water contact angle of $95^\circ \pm 2^\circ$, while the alumosilazane (SiAlCNH) was more hydrophilic with $80^\circ \pm 2^\circ$. The water contact angle of the glass cover slip was $55^\circ \pm 2^\circ$. The stronger hydrophobicity of the V_4D_4 -TMA film than that of the V_3N_3 -TMA film can be attributed to a larger number of the vinyl groups Si-CH=CH_2 per surface unit, since the vinyl-containing building blocks were four in V_4D_4 vs. three in V_3N_3 . In this study, we observed enhanced HEK293T cell adhesion with increasing surface hydrophobicity.

Despite the small differences between both MLD films, the observations confirm a great biocompatibility of both alumosilazane and alumosiloxane hybrid films.

4.3.4 In-Vitro Analysis of Bactericidal activity of the MLD films against Gram-negative (*Escherichia coli*) bacteria.

Preventing both effective bacterial adhesion and deactivation of bacterial growth upon contact with functionalized implant surfaces is of great interest and challenge in practical bioimplantation. Along with the high biocompatibility of these newly developed materials, obtained by the all-dry solventless deposition process demonstrated above, another interesting aspect is to study how bacteria behave when in contact with these materials. For the similar materials studied here, it has been reported, that silicon-based polymeric thin films, deposited by initiated chemical vapor deposition (i-CVD), show great utility as biocompatible and electrically insulating materials, and therefore could be useful as biocompatible coatings.¹⁴⁷ However, neither the biocompatibility of such organosilicon, hybrid organosilicon- alumosiloxane or alumosilazane materials has been previously reported, nor data on antibacterial testing of such materials.

The evaluation of the antimicrobial activity of the hybrid silicon-based polymer MLD films against Gram-negative bacteria *Escherichia coli* (*E. coli*) was assessed. The attachment of the bacteria and their proliferation on SiAlCNH and SiAlCOH -covered glass substrates were analyzed by confocal microscopy.

After 24h of culture, cells were dyed with DAPI and CellMask Orange fluorescent dyes to mark nuclear DNA and cellular plasma membranes, respectively. DAPI is a non-specific dye that provides fluorescence upon binding to DNA. DAPI stains all cells, not differentiating between live and dead cells. CellMask Orange dye is used to uniformly label the plasma membrane of live or fixed bacterial cells. DAPI and CellMask Orange dyes are able to penetrate living cells, which makes it possible to simultaneously track both intact (live) and damaged (dead) cells. Representative images of the crystalline nanocellulose film¹⁰³ served as a positive control. Figure 4.8 shows a well-developed *E. coli* biofilm in which bacterial cells are uniformly distributed over a nanocellulose substrate.

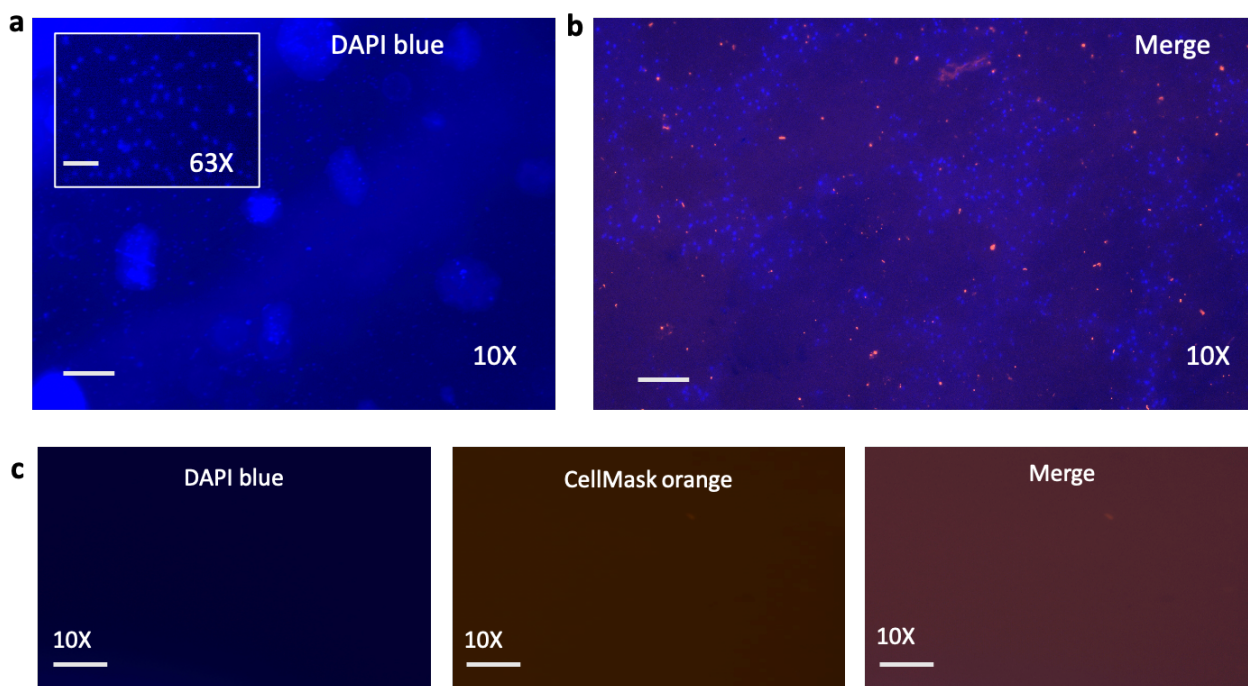


Figure 4.8: Nanocellulose film. Positive and negative control during evaluation of bactericidal activity of alumosilazane SiAlCNH and alumosiloxane SiAlCOH MLD films against Gram-negative (*E. coli*) bacteria. Confocal imaging of *E. coli* bacterial biofilms after 24h of exposure to nanocellulose substrates. (a) DAPI (blue) was used as a nuclear counterstain. (b) a merged image after dual staining with DAPI /CellMask orange plasma membrane marker. Original magnification 10x (scale bar= 10 μ m) and 63x (scale bar=4 μ m) (c) Negative control- samples exposed only to media solution without any bacteria. No response was observed from the negative control samples, as expected.

Figure 4.9 shows results of antimicrobial testing of 25 nm thick SiAlCNH and SiAlCOH MLD films after 24 h of incubation in bacterial medium. Interestingly, a large number of bacteria were observed proliferating and attaching to both tested surfaces. Both substrates are found to be ineffective against Gram-negative *E. coli*, apparently supporting the growth and proliferation of the bacterial biofilm. Moreover, on both films we observe the colonial character of bacterial growth.

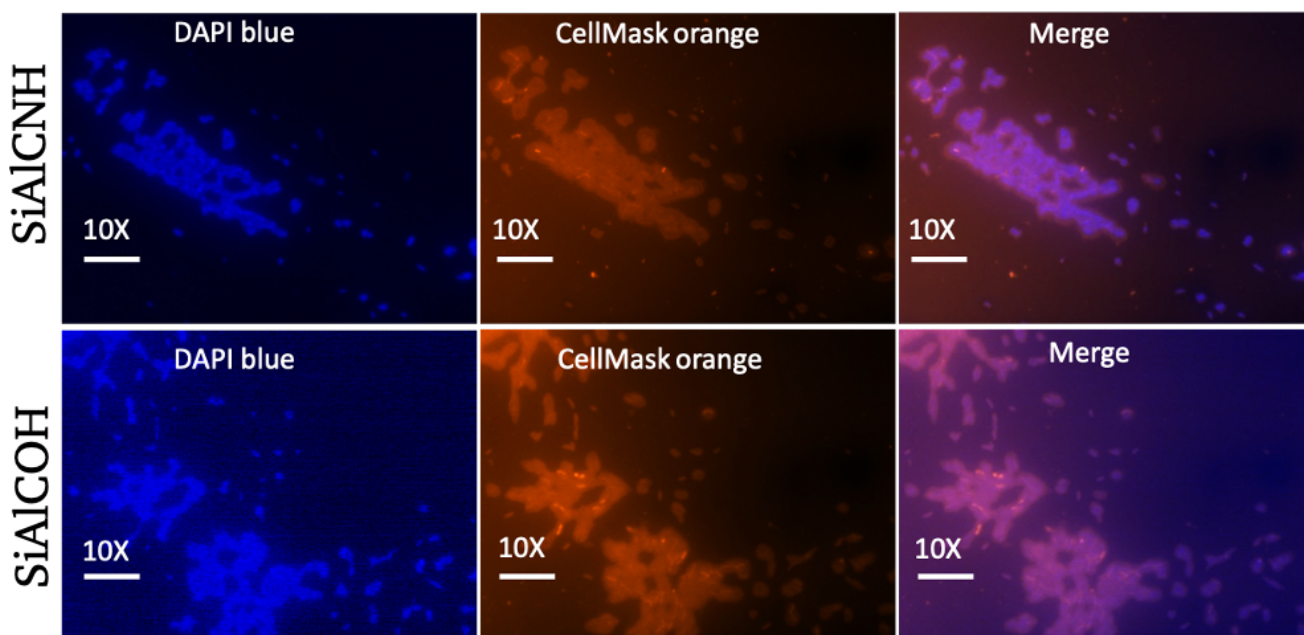


Figure 4.9: Evaluation of bactericidal activity of alumosilazane SiAlCNH and alumosiloxane SiAlCOH MLD films against Gram-negative (*E. coli*) bacteria. Confocal microscopy images of *E. coli* bacterial biofilms after 24h of exposure to hybrid MLD substrates. Original magnification 10x (scale bar= 10 μm). Bacteria were stained with DAPI (blue) and CellMask orange to label the plasma membrane and nucleus, respectively.

Such surfaces, despite their high biocompatibility, are not suitable for implantable devices due to their unfavorable bactericidal reaction. Therefore, future work will focus on optimizing these materials in terms of functionality, as well as further testing of antimicrobial efficacy against various types of microbes.

4.4 Conclusions

We applied MLD to grow ultrathin and biocompatible hybrid materials that meet the requirements for the development of stable and biocompatible surfaces. We introduced a new and facile MLD process to grow hybrid organic–inorganic alumosilazane films, making use of ring opening reactions of 2,4,6-trimethyl-2,4,6-trivinylcyclotrisilazane (V_3N_3) and coupling the molecules to TMA. The linear growth and a self-limiting behavior of the surface reactions were shown by in-situ QCM, while X-ray reflectometry determined a growth of 1.3 $\text{\AA}/\text{cycle}$. Both FTIR and XPS analyses of the film confirmed

presence of Si-NH-Si bonds, while HRTEM imaging confirmed the great conformality of the film growth on nanoparticles.

We evaluated the stability of the alumosilazane and the corresponding alumosiloxane film by XPS of aged samples, which confirmed a great stability of both investigated MLD films in air even after 2 years of exposure. Also medium solutions for cell growth did not degrade the films.

We further evaluated the biocompatibility of the films. After 6 days of culturing a continuous and uniform layer of HEK293T cells formed on the alumosilazane and alumosiloxane-coated substrates. The calculated fluorescence intensity showed a higher concentration of cells on both hybrid films in comparison to the reference sample, with a slight preference for the alumosiloxane film. The reason for the difference in cellular response is likely related to the surface chemistry and the wetting properties. The more hydrophobic alumosiloxane led to better cell adhesion. Thus, by varying the organosilicon block length by using different siloxane or silazane monomers, the hydrophobicity and the cells attachment is likely to become tunable.

MLD allows an outstanding conformality, thickness control and strong adhesion of the coatings to most substrates, due to the chemisorptive nature of the surface reactions. The developed process has proven to be stable, and its growth is easy to control, while the used materials are not critical to handle. This makes the process very valuable for a broad variety of applications. Furthermore, it can be equally well applied to particles, flat surfaces, or corrugated surfaces without loss in conformality or shadowing effects, and can also be easily upscaled, even to the industrial level. Thus, both hybrid MLD films can provide ultrathin, flexible and biocompatible coatings for scaffolds or other applications and devices where biocompatibility is needed.

Chapter 5

Bioinspired Peptidomimetic Poly(2-oxazoline)s via Vapor Phase Living Cationic Ring- Opening Polymerization

The present study reports on the first vapor phase growth of polyoxazolines (POx) via living cationic ring-opening polymerization (CROP). A tosyl-functionalized substrate is utilized as initiator for the living CROP of three substituted oxazolines, namely 2-methyl-2-oxazoline, 2-phenyl-2-oxazoline and 2-isopropenyl-2-oxazoline. The living nature of the polymerization has been confirmed by in situ QCM studies. The composition, morphology, and thermal stability of the POx have been evaluated by ATR-FTIR and XPS spectroscopies and thermogravimetric analysis (TGA).

5.1 Introduction.

5.1.1 Biomedical applications of Poly(2-oxazolines)

Biocompatible polymeric materials are intensely studied, and the suitable ones are vividly used in modern medicine. Herein the attention of researchers is strongly attracted by so-called "smart" polymers, which are polymeric materials with the ability to reversibly react to minor external triggers such as changes in the properties of the medium including temperature, acidity, ionic strength, illumination, and the presence of certain substances. One of the enablers of the concept of "smart" polymeric materials is the so-called living polymerization, which allows to design objects with a complex architecture and combine this with the sensitivity of polymers to various environmental influences.

Poly(2-oxazolines) (POx) belong to the family of pseudopeptides, i.e., bioinspired polymers or peptide mimics, due to their structural relationship to naturally occurring polypeptides.¹⁷⁴ Such polymers provide an unusual platform with highly customizable properties and excellent biocompatibility, making them interesting for a broad range of applications. POx have been tagged "smart polymers" due to their ability to exhibit switchable solubility, meaning that depending on environmental conditions, e.g., temperature, pH, or other additives, they can undergo solubility/insolubility transitions. POx also meet specific requirements needed for the development of next-generation polymer therapeutics, such as, biocompatibility, high modulation of solubility, variable length of the side chains, architecture, as well as chemical functionality,¹⁷⁵ and therefore gain increasing attention in a wide range of applications, especially in the field of biomedicine.¹⁷⁶⁻¹⁷⁹

Among the POx, the poly(2-alkyl-2-oxazoline)s are biocompatible peptidomimetic polymers with polypeptide-isomeric structures, making them important for the design

of protein-repellent surface layers and for the creation of immunoresistant, so called "stealth" nanocarriers. It was reported that block copolymers of 2-methyl-2-oxazoline and ethylene glycol, deposited on a glass substrate, reduce the adhesion of blood platelets and fibrinogen.¹⁸⁰ Chung et al. found that a thin layer of poly(2-ethyl-2-oxazoline) applied to a polyurethane film reduced platelet adhesion with the same efficiency as a polyethylene glycol (PEG) layer, which commonly serves as reference bioinert material.¹⁸¹ In addition, it has been shown that poly(2-ethyl-2-oxazoline) in hydrogels increases the viability of the cells introduced into those.¹⁸² Thus, water-soluble poly(2-alkyl-2-oxazolines) do not cause immune response in the body and are similarly biocompatible as PEG, which is one of the most studied biocompatible polymers approved for use in medicine at the present.¹⁸³ Moreover, water-soluble poly(2-methyl-2-oxazoline) retains desirable characteristics such as hydrophilicity, biocompatibility, stealth behaviour, size and structural variability, responsiveness, tunable solubility, and possibility of straightforward chemical functionalization.^{175,184}

Among the most promising applications of biocompatible polymers is their use for controlled drug delivery and recovery systems in the human body. Their conjugation with drugs and other functional objects (luminescent and radioactive labels, genetic material) is an approach that allows to increase the solubility of a drug, reduce its toxicity, extend its in-vivo circulation time, and reduce the immune response. POx are exceptionally suitable for a use as polymer-drug and polymer-protein conjugates, self-assembled carriers for drug delivery, solid dispersions, hydrogels, antibiofouling and antimicrobial surfaces, and wound healing.¹⁷⁹ The first attempt to obtain a poly(2-oxazoline)-peptide conjugate was reported by Miyamoto and Saegusa already in 1990.¹⁸⁵ They linked catalase to poly(2-methyl-2-oxazoline) and poly(2-ethyl-2-oxazoline) via an amide bond. As a result, the enzymatic activity of the conjugate was preserved in both aqueous medium and organic solvents.

Due to their biocompatibility and architectural and functional diversity, POx have been explored as polymer platforms in all areas of polymer therapeutics.¹⁷⁷ Several studies are devoted to the use of polyoxazoline-functionalized liposomes and micellar aggregates based on 2-oxazoline block copolymers for drug delivery and recovery. It has been shown that the modification of distearylphosphatidylethanolamine-based liposomes with linear poly(2-alkyl-2-oxazolines) increases their circulation time in the circulatory system and protects the liposomes against a recognition by the immune system.¹⁸⁶

In further works the use of poly(2-alkyl-2-oxazolines) as components of carriers of genetic material and as bactericidal polymers was considered.¹⁸⁷⁻¹⁸⁹ The great synthetic potential of the chemistry of POx made their application in various fields of chemical technology possible. For example, polymeric non-ionic surfactants based on block copolymers of 2-oxazolines, chemically cross-linked hydrogels, stabilizers of polymer

mixtures, and inorganic polymer hybrids were used to obtain porous silica gels. Also, liquid crystal polymers based on sterically loaded 2-substituted 2-oxazolines were shown.^{190–192} Those examples show the great potential in the use of POx, however, the main interest in the chemistry of polyoxazolines is still correlated with their biocompatibility and thermal sensitivity.

5.1.2 Cationic ring-opening polymerization of 2-oxazolines

The term living polymerization defines first-order chain reactions of monomers or active species that proceed without inter-chain bridging or chain termination.¹⁹³ Of great importance is the quantitative and, compared to a chain growth during the propagation step, very fast initiation of the polymerization, which ensures a simultaneous and uniform chain growth. The number of active chains, determined by the ratio of the monomer to initiator concentrations, remains constant throughout the reaction. If all monomers are consumed during the polymerization, the chain ends remain “living”, since no termination reaction occurred. The living nature of this polymerization method allows for the preparation of well-defined block copolymers by the addition of a second monomer when the first monomer is completely consumed.¹⁹⁴ In the mid-1960s, the first publications on living CROP reactions of 2-oxazolines and cyclic imino ethers were published independently by four groups.^{195–197}

Kobayashi and Saegusa were the first to synthesize block copolymers by copolymerizing various 2-oxazolines. They showed that the cationic polymerization of 2-oxazolines can be reinitiated by adding a second monomer to the reaction mixture after complete consumption of the first. This method of “post-polymerization” made it easy to synthesize block copolymers with controllable lengths and with different amounts and qualities of the contained blocks.¹⁹⁴

Oxazolines are five-membered ring systems with one oxygen and one nitrogen atom in the 1 and 3 positions, respectively. Electrophiles can attach to the nitrogen atom of a five-membered ring, initiate subsequent ring opening by forming an oxazolinium ion, and polymerize with an excess of the monomer. Figure 5.1 schematically describes the mechanism for the CROP of 2-oxazolines using methyl tosylate as initiator and H₂O as terminating agent.

The CROP mechanism consists of three steps: initiation, propagation, and termination. In the first step, the polymerization is initiated by an electrophile. In principle any sufficiently electrophilic compound can be used as initiator. Alkyl sulfonates, such as methyl p-toluenesulfonate, p-nitro benzenesulfonates and trifluoromethanesulfonates are most common, but alkyl-, benzyl-, and acetyl halides, oxazolinium salts, and Lewis acids are also used.^{198,199} The nucleophilic attack of the lone electron pair of the nitrogen of in the 2-oxazoline monomer results in ring opening and the formation of a cationic oxazolinium propagating species.

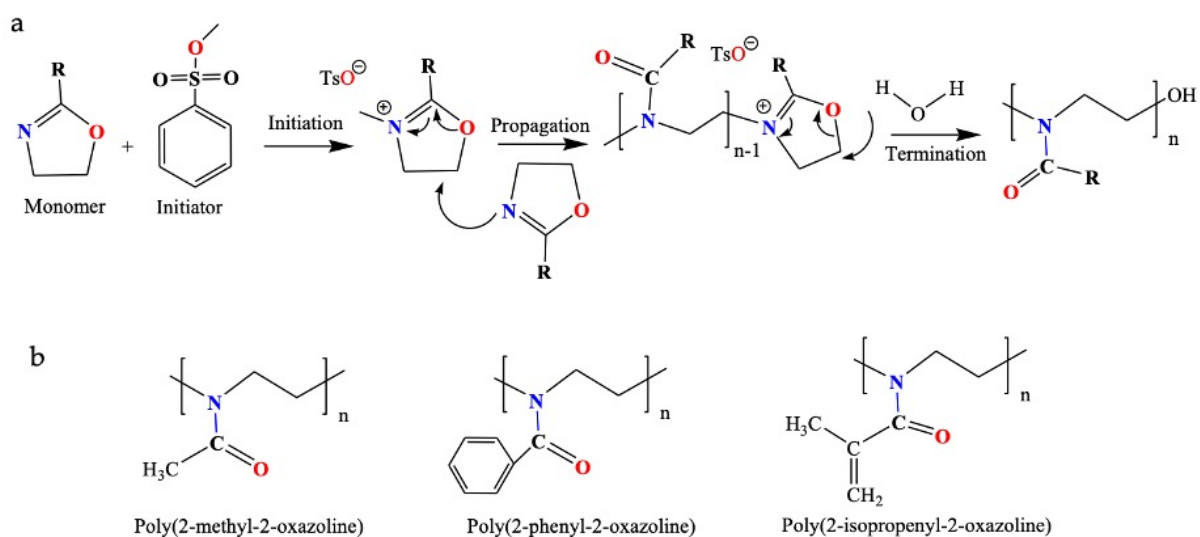


Figure 5.1: (a) Schematic representation of the cationic ring opening polymerization mechanism of poly(oxazolines), initiated by p-toluenesulfonate, and quenched with water. R stands for a side-group that can be varied. (b) Chemical structures of polymers used in this work: poly(2-methyl-2-oxazoline), poly(2-phenyl-2-oxazoline) and poly(2-isopropenyl-2-oxazoline).

The driving force behind the ring-opening polymerization is, on the one hand, the isomerization of the imino group to an amide group and, on the other hand, the release of the ring strain of the five-membered ring.²⁰⁰

In the subsequent propagation step, the carbon atom of the weakened C-O bond will undergo a nucleophilic attack by the next monomer, resulting in ring-opening and the formation of a new amide, while preserving the living oxazolinium chain-end. Due to the living nature of the polymerization, the chain growth continues steadily and only

stops when the monomer is consumed but can be continued by further monomer addition. In an ideal case, no chain coupling, transfer, or termination reaction takes place during the CROP of 2-oxazolines, which ensures the living nature of the polymerization.

Finally, the termination of the CROP of the POx chain occurs via a nucleophilic attack of an added termination agent which forms a stable bond with the cationic chain end and prevents further attacks by monomers. Nuyken studied the mechanism and kinetics of the chain termination reaction in the cationic polymerization of 2-oxazolines in detail and identified two possible pathways for the chain termination. Mild termination agents, such as water, preferentially attach to the 2-position of the oxazolinium ion (see Fig.5.1, a), leading to the formation of a secondary amino group and an ester fragment at the end of the polymer chain. In contrast, strong nucleophiles, such as N-nucleophiles and carboxylates, will attach to the 5-position of the oxazolinium ion. In practice, piperidine, morpholine, piperazine, or alcoholic solutions of alkali (NaOH, KOH) are most often used for chain termination since these reagents provide fast and complete chain termination by adding to the 5-position of the oxazolinium ion.

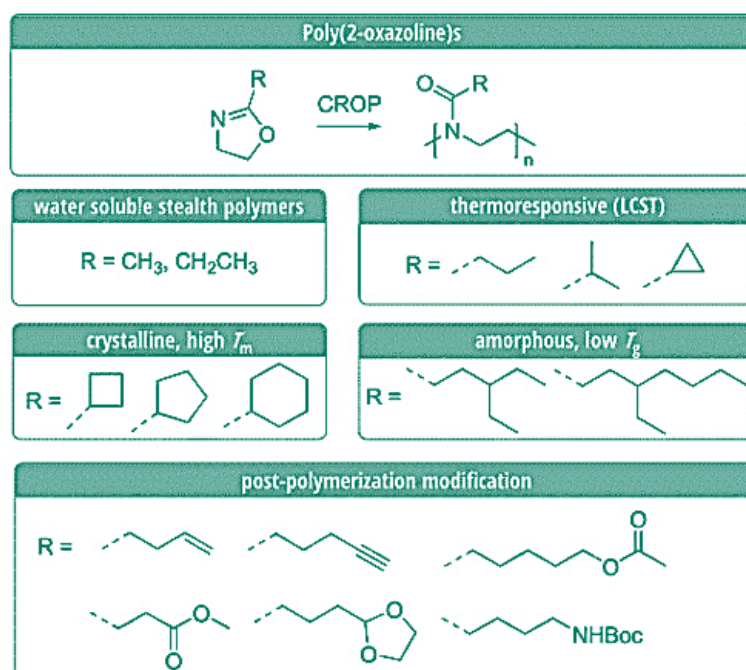


Figure 5.2: Various functionalities of POx obtained by varying the substituents in the side chain of the oxazoline.

The composition and the properties of the resulting polymer depend on many factors. The amide group which forms upon ring opening makes the polymeric backbone intrinsically very polar. Due to the facile synthesis, mostly 2-substituted oxazolines are used for polymerization reactions.

By varying the substituents in the 2-position, the characteristics of the polymer can be varied (Figure 5.2). Finally, the termination reaction also provides a means for direct functionalization of the polymer end groups.

Among the mentioned ways to manipulate the functionalities of the POx, the selection of the 2-oxazoline monomers with the desired physical properties and/or chemical functionality for a particular application,^{201,202} including antimicrobial properties,^{188,189} is the preferred route. For example, unsubstituted 2-oxazoline and 2-methyl-, 2-ethyl-, 2-propyl-, 2-isopropyl-2-oxazolines polymerize to form water-soluble poly(2-alkyl-2-oxazolines).²⁰³ Hydrophobic POx can be obtained by polymerization of 2-phenyl-, 2-perfluoroalkyl-2-oxazolines and monomers with long alkyl substituents (C4-C9). The polymer resulting from the polymerization of 2-nonyl-2-oxazolines is highly hydrophobic and water-insoluble.^{203,204} Given the enormous combination possibilities, by now already a great number of functional 2-substituted 2-oxazolines has been synthesized and used for polymerization reactions.

The living polymerization fabricates linear polymer chains with a defined structure and length. The probability of side reactions increases with increasing polymer length and causes a broadening of the molar mass distribution. Due to the comparably low polymerization rates, which is intrinsic to the CROP of 2-oxazoline monomers, the use of microwave (MW) reactors for chemical syntheses is beneficial for obtaining higher molar masses and better-defined molar mass distributions.²⁰⁴⁻²⁰⁶

The biocompatibility of POx makes them ideal platforms for the development of polymeric therapeutics and biomaterials. Some of the envisioned applications include nanotechnology-based smart devices, tissue targeting, drug delivery, and biocompatible packaging of implantable medical devices. However, many such applications rely on the conformal growth of such polymers as thin films with proper adhesion to various functional substrates, even with complex shapes. But the production of these polymers in the form of conformal thin-film coatings is difficult with conventional multicomponent solution-based strategies. Furthermore, the purity of the final polymer can be easily hampered by the use of multiple components for their synthesis, which is needed for the wet-chemical approach.

In response to the mentioned shortcomings of the wet-chemical living polymerization, in this work we propose a novel approach, namely a solvent-free vapor phase synthesis of POx films. The developed process is stable and easy to control, while the used materials are not critical to handle. The polymerization process is performed in a vacuum reactor commonly used for the atomic or molecular layer deposition (ALD/MLD) of nanoscale inorganic or organic films. The two-step process includes a pulsed supply of a vaporized initiator to a reactor space, which functionalizes a substrate by adsorbing

as a molecular layer. This is followed by the chain propagation after the monomer is supplied and interacts with the layer of the chemisorbed initiator. After exposing the substrate to the monomer vapors for several seconds, the chamber is purged, and another portion of the vaporized monomer is introduced. With each monomer pulse, the thickness of the polymer layer increases until the monomer is consumed, which makes it possible to control the final thickness of the coating with the dose and by the number of cycles. The supply of water vapor to the reactor causes the growth to terminate. This growth is suitable for the development of new poly(2-oxazoline) materials with controlled composition, thickness, and, therefore, well-defined parameters.

The main advantages of this vapor-based approach are including very high conformality of the grown film, absence of impurities, thickness control, and strong adhesion of the films to most substrates due to chemisorptive nature of the involved vapor-solid surface reactions.

5.2 Results and discussion

5.2.1 Living Cationic Ring-Opening

Polymerization mechanism of 2-oxazolines

For the vapor-phase synthesis of poly(2-oxazolines) we used P-Toluenesulfonyl chloride (TosCl) as initiator and 2-methyl-2-oxazoline, 2-phenyl-2-oxazoline, and 2-isopropenyl-2-oxazoline as monomers. A schematic of the idealized reaction mechanism for the vapor-phase living CROP of 2-oxazolines is depicted in Figure 5.3.

The tosyl-functionalized surface, obtained after the first step (Fig. 5.3, (a-c) (A)), is utilized as starting point for the propagation process during the living CROP. In the first step, the TosCl vapors are supplied to the chamber with 5 seconds of exposure time were allowed to ensure that the surface is completely saturated, generating a chemisorbed tosyl-functionalized (sub)monolayer. Nitrogen is used as the carrier gas for the precursor supply and purge of the byproducts. After the step A, the reactor is purged with the inert gas to remove the byproduct HCl and unreacted TosCl.

The subsequent step (B), equivalent to the propagation step in the wet-chemical approach, includes alternating pulses of monomer vapors into the chamber. The monomer itself reacts with the chemisorbed initiator species to form the poly(2-methyl-2-oxazoline) (Fig. 5.3 (a)) backbone by ring-opening and amide bond formation, while the oxazolinium chain-end remains living. After few seconds of exposure, the chamber is purged, and another dose of the vaporized monomer is supplied.

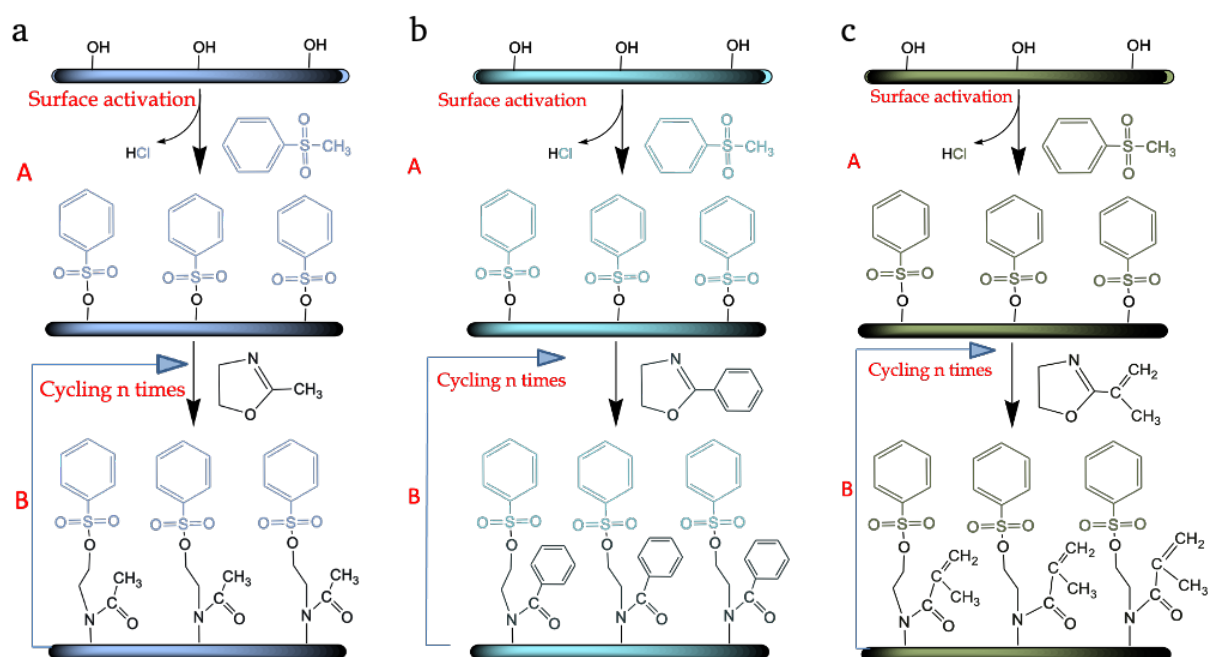


Figure 5.3: Schematic illustration of the gas-phase living CROP mechanism of (a) 2-methyl-2-oxazoline, (b) 2-phenyl-2-oxazoline and (c) 2-isopropenyl-2-oxazoline from the vapor phase in a two-step process: A: Substrate is exposed to p-toluenesulfonyl chloride (TosCl), which reacts with the surface OH groups resulting in a tosyl-functionalized chemisorbed monolayer. B: Repetitive dosing of 2-oxazoline vapors, precursor exposure for several seconds, and purging with N_2 . The living polymer chains can be directly terminated with various reagents e.g., by pulsing water vapor into the reactor (not shown).

During the polymerization, the reactions in the propagation step are not self-limiting, but once the provided vaporized monomer is consumed, the polymerization stops, while the chain is still living. Assuming that the monomer is completely consumed in each pulse, by controlling the dosing time for different supplied monomers, one can control the lengths of the polymer chains. Although in this work we show only the growth of POx homopolymers, copolymerization via sequential monomer addition is also possible. In this case the process parameters will allow the control of the lengths

of the alternating segments of different polymers within the copolymer or the ratio of the sub chains in the resulting copolymer. By varying the nature of introduced monomers, one can control the length and composition of the polymer chains.

The growth behavior during the process was examined by in-situ Quartz Crystal Microbalance (QCM) studies at 130°C.

Figure 5.4 (a) shows the QCM mass change vs. time during the supply of the initiator and the following 31 doses of 2-methyl-2-oxazoline at 130 °C to alumina, which was used as substrate.

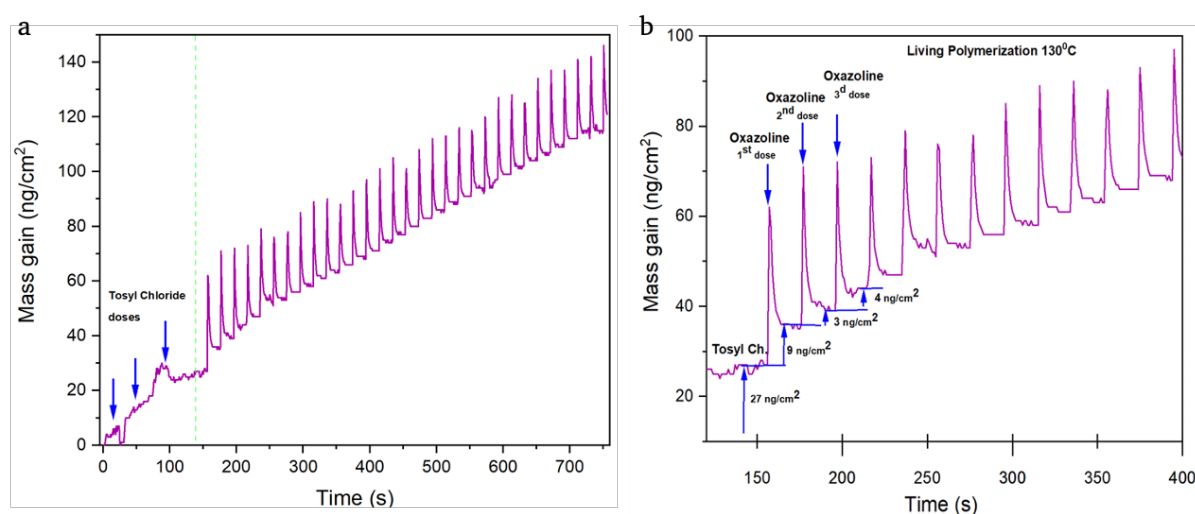


Figure 5.4: QCM measurements. (a) QCM mass gain versus time for the living CROP of 2-methyl-2-oxazoline on an ALD-Al₂O₃ pre-deposited surface at 130 °C. The growth was monitored over 31 doses of 2-methyl-2-oxazoline on a tosyl-functionalized surface. The pulse and purge time sequence used in the surface activation step was 1 s/20 s for TosCl/N₂. For 2-methyl-2-oxazoline/N₂, a pulse purge time sequence of 1 s/20 s was used. (b) Expanded view of the mass gain during 13 pulses of 2-methyl-2-oxazoline.

The alumina was pre-deposited by ALD at the same temperature prior to the polymerization experiment to have a clean starting surface.

An expanded view of the QCM signal with 13 doses of 2-methyl-2-oxazoline is shown in Figure 5.4 (b). A dose of the initiator TosCl results in a mass increase of 27 ng/cm², indicating its successful binding to the surface. After each dose of 2-methyl-2-oxazoline, we observed an average mass gain of about 5 ng cm⁻². The slight variations in the mass gain after several pulses of the monomer were caused by initial process instabilities and a linear and reproducible mass increase was observed after ~10 cycles. Overall, the QCM data confirm a linear mass increase with the number of monomer pulses, indicating a living nature of the polymerization.

Insight into the structure of the obtained polymer layers was provided by FTIR spectroscopy.

The FTIR spectrum of poly(2-methyl-2-oxazoline) (Figure 5.5) shows absorption bands at 2969 cm^{-1} and 2932 cm^{-1} corresponding to CH_2 - stretching vibrations.

The bands at 1629 cm^{-1} and 1420 cm^{-1} , which are characteristic to poly(2-methyl-2-oxazoline), are assigned to $\text{C}=\text{O}$ stretching (amide I) and CH_3 bending modes, respectively, and indicate a successful ring opening polymerization.^{207,208}

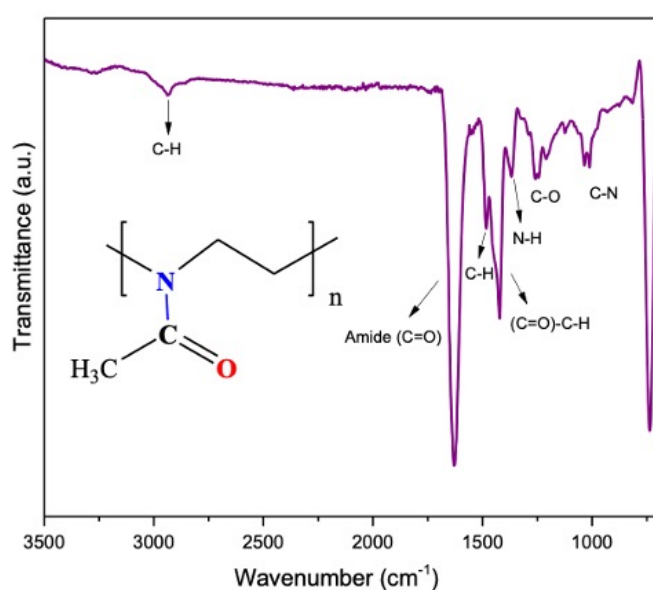


Figure 5.5: ATR-FTIR spectrum of the poly(2-methyl-2-oxazoline) film, deposited on a pellet of pressed ZrO_2 nanoparticles at $130\text{ }^\circ\text{C}$, after subtraction of the spectrum of the neat pressed ZrO_2 pellet.

The absorption bands at 1480 and 1366 cm^{-1} (CH bending) as well as those at 1247 , 1189 and 1021 cm^{-1} (C-C stretching) are in good agreement with the literature-known FTIR data of poly(2-methyl-2-oxazoline).^{207–209}

The surface chemical composition of the polymer was studied with XPS. Figure 5.6 shows XPS spectra around the C 1s and N 1s core-level regions of the poly(2-methyl-2-oxazoline) film deposited at $130\text{ }^\circ\text{C}$.

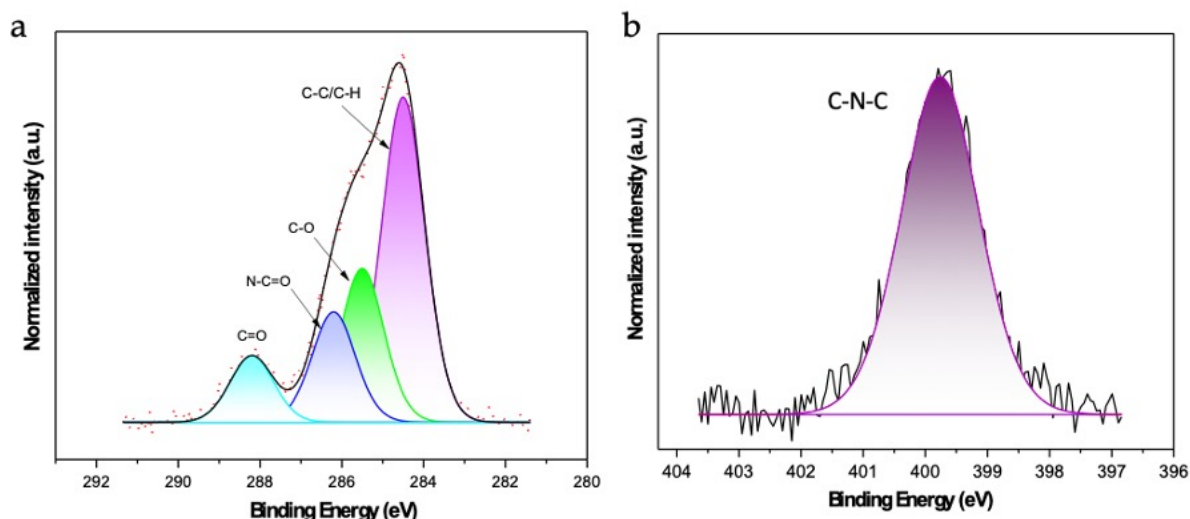


Figure 5.6: High-resolution (a) C 1s and (b) N 1s core-level XPS spectra of the poly(2-methyl-2-oxazoline) film, deposited at 130 °C.

The peak around C 1s can be deconvoluted into four components and shows contributions at 284.5, 285.5, 286.2 and 288.2 eV.

Those are mainly attributed to C–C/C–H, C–N, C–O and N–C=O groups, as indicated in the figure.²¹⁰ The N 1s XPS spectrum at the binding energy of 401.26 eV is assigned to C-N-C, originating from the polymer backbone.²¹¹ Both spectra confirm the successful ring opening polymerization of 2-methyl-2-oxazoline with the presence of the N-C=O signal.

The FTIR spectrum of the poly (2-phenyl-2-oxazoline) film is shown in Figure 5.7. The spectrum shows bands at 1629 cm^{-1} , which are characteristic to POx and are assigned to C=O stretching modes (amide I). The bands confirm the successful ring opening reaction.

The peaks at 1010 cm^{-1} originate from the C-N bond. The peaks at 2950-3100, 1400–1500, and 1640 cm^{-1} are correlated with the (asymmetric and symmetric) vibrations of the CH_2 group, and C-C (in aromatic rings) and C=C stretching vibrations, respectively.²¹² Multiple C=C ring vibrations around 2000 cm^{-1} , associated with the aromatic ring, were also observed.

Thus, the FTIR analysis confirms the presence of the phenyl ring and the backbone of poly(2-phenyl-2-oxazoline), which formed after the ring opening reaction.

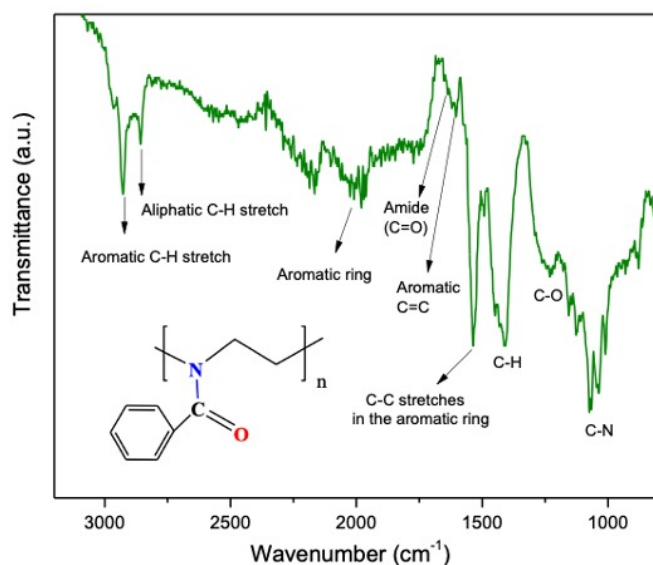


Figure 5.7: ATR-FTIR spectrum of a poly(2-phenyl-2-oxazoline) film, deposited onto a compressed pellet of ZrO_2 nanoparticles at 130°C , after subtraction of the spectrum of the neat pressed ZrO_2 pellet.

The C 1s XPS spectrum in Figure 5.8 (a) reveals several components originating from differently bound carbon within the polymer film.

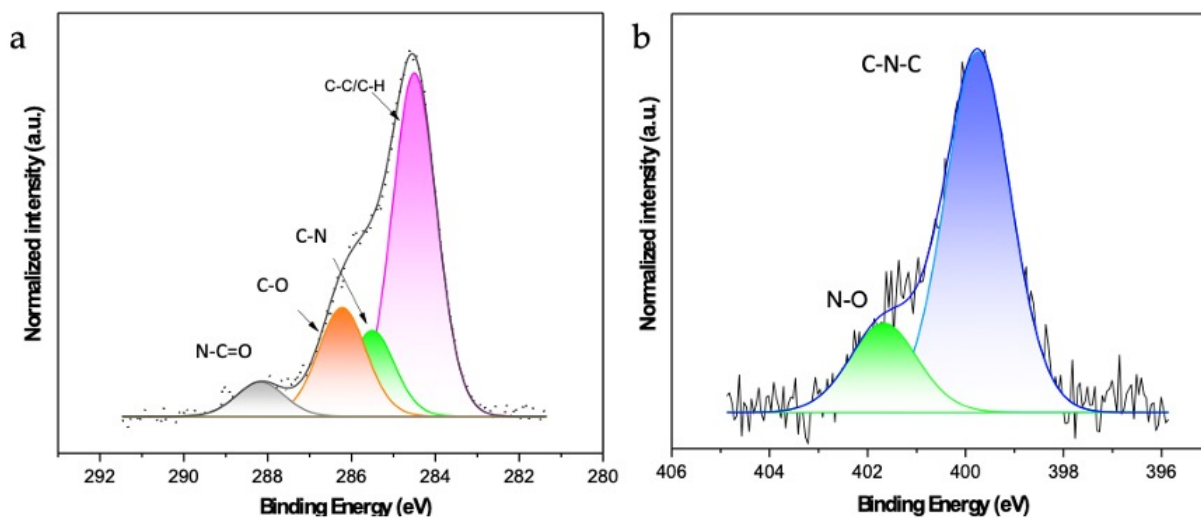


Figure 5.8: High-resolution (a) C 1s and (b) N 1s core-level XPS spectra of the poly(2-phenyl-2-oxazoline) film, deposited at 130°C .

The spectrum was deconvoluted into four components, showing contributions from C–C/C–H (284.5 eV), C–N (285.5 eV), C–O (286.2 eV) and N–C=O (288.2 eV) groups.²¹⁰ In contrast to poly(2-methyl-2-oxazoline), an additional peak in the N 1s

spectrum was observed (Fig.8 (b)). The additional peak at 401.67 eV, assigned to N-O bonding, most likely originates from surface contamination.

Poly(2-isopropenyl-2-oxazoline) (PIPOx) is a functional polymer with a demonstrated high potential for drug delivery, tissue engineering, and immunomodulation.²¹³

The FTIR spectra of the synthesized polymer film are shown in Figure 5.9.

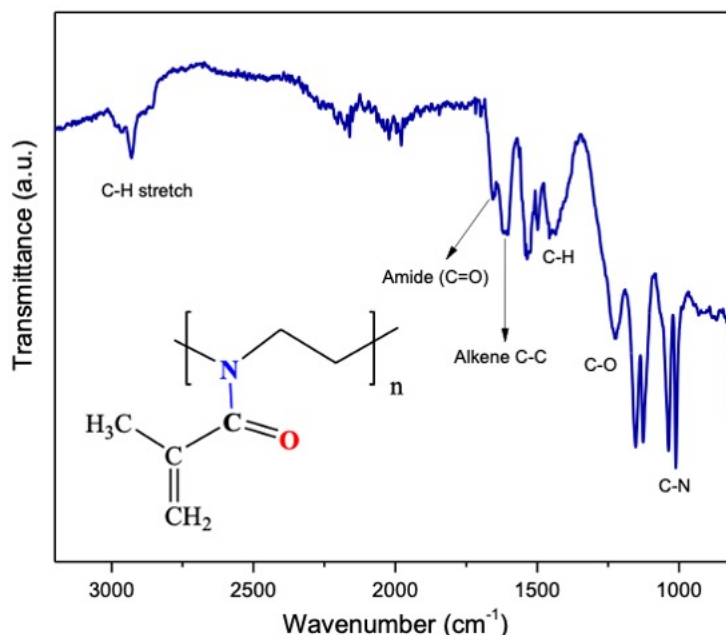


Figure 5.9: ATR-FTIR spectrum of a poly(2-isopropenyl-2-oxazoline) film, deposited onto a pressed pellets of ZrO₂ nanoparticles at 130 °C, after subtraction of the spectrum of the neat pressed ZrO₂ pellet.

The observed bands at 1650 cm⁻¹ and 1490-1440 cm⁻¹ are characteristic of poly(2-oxazoline) and can be assigned to C=O stretching (amide I) and CH bending, respectively. Few additional =C-H and alkene C-C stretching bands from alkene groups were detected at 2950-3100 and 1600–1530 cm⁻¹, confirming the presence of isopropenyl moieties.²¹³

The XPS analysis of the polymeric films showed the chemical environment around the C 1s and N 1s core level regions (figure 5.10.)

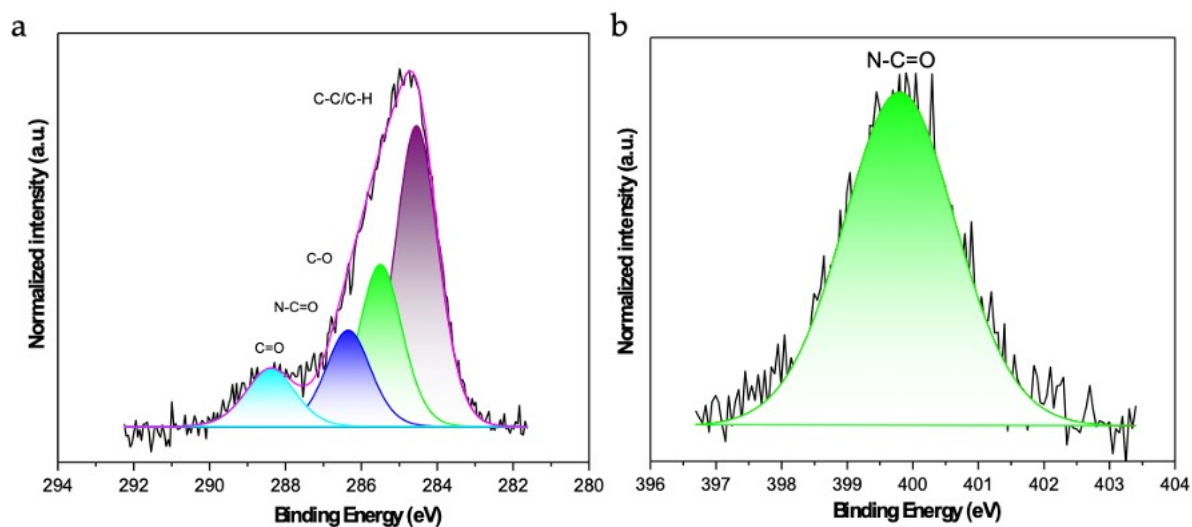


Figure 5.10: High-resolution (a) C 1s and (b) N 1s core-level XPS spectra of poly(2-isopropenyl-2-oxazoline), deposited at 130 °C.

Similar to the previously described polymers, the C1s peak can be deconvoluted into four components. The peaks at 284.5, 285.5, 286.3 and 288.3 eV are attributed to C–C/C–H, C–N, C–O and N–C=O groups, respectively,²¹⁰ pointing towards a ring opening step in the polymerization mechanism. The N 1s peak at the binding energy of 399.8 eV is assigned to C-N-C and is in agreement with the literature-known data on poly(2-oxazolines).^{184,210,211}

5.2.2 Thermogravimetric analysis of the obtained from the gas-phase Polyoxazoline (POx) polymeric films.

The thermal stability of the POx polymers has been investigated by TGA with a heating rate of 10 °C/min in a nitrogen atmosphere. The analysis was done in the range of 25–800 °C. Figure 5.11 shows the TGA plots of poly(2-methyl-2-oxazoline), poly(2-phenyl-2-oxazoline) and poly(2-isopropenyl-2-oxazoline) films, grown at 130 °C.

The TGA thermograms of all three POx showed decomposition in several stages, at ambient to 115 °C, 200–300 °C, and >330 °C. According to reported data, poly(2-methyl-2-oxazoline) is thermally stable up to 200-250 °C.^{214–216} Thus, the observed first stage (ambient to 115 °C, weight loss \approx 20%) likely corresponds to the desorption of physically absorbed water due to the exposure of the samples to air.

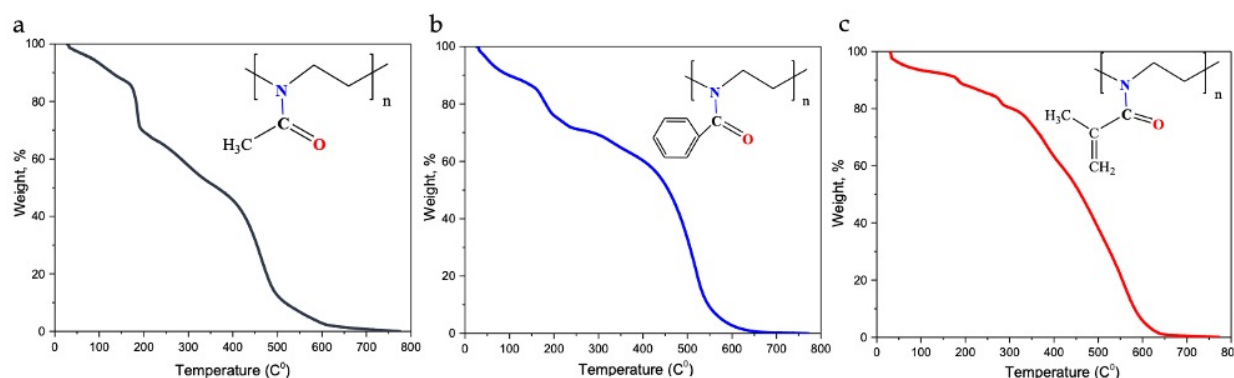


Figure 5.11: Thermogravimetric analysis (TGA) of (a) poly(2-methyl-2-oxazoline), (b) poly(2-phenyl-2-oxazoline), and (c) poly(2-isopropenyl-2-oxazoline), all grown at 130 °C.

The second stage (above 200 °C) marks the onset of the polymer degradation. The TGA thermograms of the POx showed that all three polymers start to decompose in that thermal range. The major degradation of all three POx took place in the third stage, i.e., above 300 °C. Poly(2-methyl-2-oxazoline), poly(2-phenyl-2-oxazoline) and poly(2-isopropenyl-2-oxazoline) maintained about 50 % of their weight at 350, 430 and 450 °C, respectively. All vapor-phase grown polymers show a similar thermal stability as their corresponding polymers obtained from solution. Poly(2-isopropenyl-2-oxazoline) showed the best thermal stability among all three tested polymers.

5.3 Conclusions

This work demonstrates a novel approach to the solvent-free vapor phase fabrication of polymer films, which is leaned on the living polymerization process. The developed two-step process is stable and easy to control. After the supply of an initiator, the growth of the polymer can be controlled with the supply of a suitable monomer. Being a non-line-of-sight vapor phase process, it allows a conformal POx film growth even on high aspect ratio structures. Moreover, the methodology also allows for the

incorporation of terminal groups, thereby enlarging the toolbox for the manipulation of the functionalities of the resulting polymer.

In-situ QCM data showed a mass gain after the self-limiting reaction of TosCl with the substrate during the initiation step, confirming successful surface functionalization. Those functional sites restrict the subsequent propagation to this area only since propagation can only take place where the initiator is present. A linear QCM mass increase during alternating monomer supply on the propagation step, confirming the living nature of the vapor phase POx polymerization.

FTIR confirmed the presence of C=O stretching (amide I) and CH chemical bonds, characteristic to POx, which indicates that the ring opening polymerization occurs as anticipated. XPS data further confirm successful ring opening reactions with all three investigated monomers upon their binding to the tosyl-functionalized surface, which forms the backbone of the three substituted poly(2-oxazoline)s. The thermogravimetric analysis of the polymers showed their good thermal stability, which is in good agreement with their wet-chemically grown counterparts.

Future work will focus on the process optimization and the properties of the POx, especially their bioactivity as such materials have a great application potential in the biomedical field and could be applied in nanotechnology-based smart devices, tissue targeting, or drug delivery. Since the propagation of the polymer growth can only take place where the initiator is present, surface patterning with the initiator allows for an area-selective polymer growth, which is a further aspect that will be investigated in future work. Thus, the present development is a starting point for a new way of surface functionalization with functional polymeric materials.

Chapter 6

Summary and Outlook

This thesis presents three different strategies for a Molecular Layer Deposition (MLD)-enabled creation of new bioinspired materials, which include:

1) the conformal growth of chitin and new biomimetic chitin-based antibacterial and biocompatible hybrid functional films, that is, metallochitins.

2) the ring-opening reaction for biocompatible organic–inorganic hybrid aluminosilazane thin films as a new materials group, using sequential surface reactions between Trimethyl-trivinylcyclotrisilazane (V_3N_3) and trimethylaluminum (TMA).

3) the first gas-phase living cationic ring-opening polymerization (CROP) of Poly-oxazolines (POx)s: poly(2-methyl-2-oxazoline), poly(2-phenyl-2-oxazoline) and poly(2-isopropenyl-2-oxazoline).

In the first part, a novel solvent-free vapor phase process for growing nanoscale coatings of chitin-based materials was developed. Besides the growth of organic chitin, a new class of organic–inorganic hybrid polymers, which we coin “metallochitins” or more generally “metallo-saccharides”, which beneficially combine the characteristics of organic chitinoid polymers and inorganic metal oxides, are introduced. The organic chitin was grown by coupling the monosaccharide N-Acetyl-D-mannosamine (ManNAc) after activation with thionyl chloride. For the controlled growth of the hybrid metallochitins, we coupled ManNAc with trimethylaluminum (TMA) or Titanium tetraisopropoxide (TTIP) to obtain the respective biomimetic alumochitin or titanochitin thin films. In addition, the composition, structure, and growth of the metallochitin films have been investigated through various experimental and theoretical (DFT) studies, which confirmed that metallochitins grow according to the proposed mechanism.

After successful film growth, the potential of the metallochitin films to mimic the antimicrobial behavior of chitin was assessed. We evaluated the attachment and proliferation of Gram-positive and Gram-negative bacteria on substrates coated with alumochitin and titanochitin. The mechanisms underlying the antibacterial selectivity and activity of metallochitins, bacterial adhesion tendencies with respect to surface chemistry, hydrophobicity, zeta potential, and surface roughness were explained. The differences in the behavior of both metallochitins against the two types of bacteria is likely caused by the more positive zeta potential and thus surface charge of alumochitin in comparison to titanochitin and the more negative charge of gram-negative bacteria in comparison to the gram-positive bacteria. This suggests a weaker electrostatic interaction of titanochitin with *S. aureus* bacteria and consequently a lower tendency of physical disruption of the cell wall. Moreover, the thicker cell wall and the absence of an outer cell membrane in *S. aureus* contribute to its stabilization.

The results of the in vitro proliferative behavior of human embryonic kidney cells (HEK293T) and human fibroblasts cultured on the nanolayers confirmed even better

cell attachment and proliferation on metallochitins than on the positive control. In conclusion, the results on the biological activity of metallochitins confirmed their ability to mimic the natural functionality of chitin, demonstrating excellent biocompatibility while inhibiting bacterial attachment and growth.

In the second part, a new materials group of hybrid aluminosilazane (SiAlCNH) films is introduced. A readily applicable MLD process for growing a silazane-alumina hybrid material, using the ring-opening reaction of 2,4,6-trimethyl-2,4,6-trivinylcyclotrisilazane (V3N3) and its combination with trimethylaluminum (TMA), was described.

The exceptionally good biocompatibility of the resulting SiAlCNH MLD films was evidenced by a significantly higher proliferation of human embryonic kidney cells (HEK293T) than on glass, which was used as a positive control. Such highly biocompatible and conformal films hold great promise as functional coatings for scaffolds or implantable devices with complex topologies or high aspect ratio structures.

The third part reports on the first solvent-free gas-phase synthesis of polyoxazolines (POx) via living cationic ring-opening polymerization (CROP). A two-stage mechanism was developed for the polymerization of 2-methyl-2-oxazoline, 2-phenyl-2-oxazoline, and 2-isopropenyl-2-oxazoline, using P-toluenesulfonyl chloride (TosCl) as initiator. Opening of the 2-oxazoline ring during the polymerization was confirmed by the presence of a characteristic C=O bond (amide I), which was further supported by FTIR and XPS data. The living nature of the polymerization was confirmed by in situ QCM studies.

The proposed solvent-free approach towards the synthesis of POx from the vapor phase is beneficial for the development of new poly(2-oxazoline) films with controlled composition, thickness, and absence of impurities. In addition, the conformality of the grown film and strong adhesion of coatings to the substrate can be achieved due to the chemisorptive nature of the involved surface reactions.

In conclusion, in this thesis several radically new MLD processes were developed, which allow the synthesis of various materials with intriguing biological properties, which were not accessible by vapor phase processing before. Not only this work expands the set of processes and materials that can be grown with MLD, but also it provides a solid foundation for the fabrication of various thin films with great relevance in the biomedical and biological research area.

These results extend the horizon of the current applicability range of thin films and will contribute to the further development of conformal bioactive hybrid polymeric thin films deposition processes. The employed strategies serve as first steps for growing databases of new hybrid films and considerable future work is required to fully exploit the seeds which were planted with the present work. A variety of further sugar molecules and their functionalization with various metals can be combined to not only

achieve passive antimicrobial properties, but potentially also introduce active, i.e., bactericide functionalities.

The demonstrated living polymerization of oxazolines on three different monomers serves only as proof of principle and given the vast amount of demonstrated wet-chemical processes, this approach offers plenty of space for further investigation and adaptation of materials for specific applications. Therefore, the present thesis is only the first step into the exciting field of MLD-enabled biomimetic functional thin film growth.

Acknowledgments

Undertaking this PhD has been a great experience for me and it would not have been possible to do without the support and guidance that I received from many people.

First of all, I want to express my gratitude to my supervisor Prof. Mato Knez, who gave me the opportunity to perform my doctoral project in the group of nanomaterials. Thanks for your patience, invaluable advice, feedback on my research and for always being so supportive.

I would like to acknowledge and give my warmest thanks to Prof. Ilmutdin Abdulagatov and Dr. Aziz Abdulagatov. Thank you for supporting, inspiring and sharing professional knowledge about ALD/MLD from the very beginning of this journey.

I would like to acknowledge funding through European Union's Horizon 2020 research and innovation program under the Marie Skłodowska-Curie (grant agreement No. 765378).

I would like to thank the whole HYCOAT team, especially Jolien Dendooven and Christophe Detavernier for their guidance through this project.

I would like to acknowledge the members of my dissertation committee: Prof. Jolien Dendooven, Prof. Miguel Manso Silván and Prof. Thomas Schäfer. I appreciate your kind assistance and the time you have spent to examine and evaluate my work.

This PhD study would not have been possible without all the technical assistance in the lab I received from the former and present technicians, Mikel Beltrán Hernández and Raydel Pérez Menéndez. It was a pleasure to work with you and I appreciate your help, ideas and humor.

I appreciate the support received through joint work with the University of Rijeka, Dr. Iva Šarić and Prof. Mladen Petravić. Thank you for providing us help with XPS measurements, data analysis and for your hospitality during our visits to Rijeka.

This work is done in collaboration with Nanobiotechnology group and I would like to sincerely thank Dr. Borja Alonso-Lerma, Dr. Leire Barandiaran and Prof. Raul Perez-Jimenez for helping me with in vitro cell culturing and bacterial testing.

I express my gratitude to Dr. Evgenii Modin and Prof. Andrey Chuvilin for their help in conducting TEM/SEM studies.

I would like to acknowledge the collaborative work with Tyndall National Institute, University College Cork. I am especially grateful to Arbresha Muriqi and Prof. Michael Nolan for providing theoretical insights to this work.

Special thanks to Moritz Remmers, a master student, who has been extremely helpful in the grafting work outlined in Chapter 5.

Agradezco especialmente a todos mis amigos en Rusia y España por estar siempre ahí en mis buenos y malos momentos y que siempre me ayudaron de muchas maneras.

Un agradecimiento especial a Andrey Bylinkin, Momo (Natalia), Valentina, Miriam, Fede, Djuro, Gabriele, Kristina, Oksana, Viktor, Olga, Kate, Jorge, y aquellos a quienes olvidé mencionar, por el gran tiempo que pasamos juntos. Ha sido un placer trabajar y disfrutar de la vida con todos vosotros.

Quiero agradecer al grupo de Nanomateriales ya todo el personal de nanoGUNE por compartir un gran momento en nuestros group-meeting, nano-diners and nano-sidre-rias.

Finally, a gratitude that is especially close to my heart goes to my Mum and Dad. Thank you for unconditional support and love. Special thanks to Dr. Kristina Ashurbekova for her comprehensive assistance as a sister and colleague at the same time.

References

1. Malygin, A., Drozd, V., Malkov, A. & Smirnov, V. From V. B. Aleskovskii's "Framework" Hypothesis to the Method of Molecular Layering/Atomic Layer Deposition. *Chemical Vapor Deposition* 21, 216–240 (2015).
2. Puurunen, R. L. Surface chemistry of atomic layer deposition: A case study for the trimethylaluminum/water process. *Journal of Applied Physics* vol. 97 Preprint at <https://doi.org/10.1063/1.1940727> (2005).
3. Dasgupta, N., Meng, X. (Henry), Elam, J. & Martinson, A. Atomic Layer Deposition of Metal Sulfide Materials. *Acc Chem Res* 48, (2015).
4. George, S. M., Dameron, A. A. & Yoon, B. Surface chemistry for molecular layer deposition of organic and hybrid organic-inorganic polymers. *Acc Chem Res* 42, 498–508 (2009).
5. Gregorczyk, K. & Knez, M. Hybrid nanomaterials through molecular and atomic layer deposition: Top down, bottom up, and in-between approaches to new materials. *Progress in Materials Science* vol. 75 1–37 Preprint at <https://doi.org/10.1016/j.pmatsci.2015.06.004> (2016).
6. Meng, X. (Henry). An Overview of Molecular Layer Deposition for Organic and Organic-Inorganic Hybrid Materials: Mechanisms, Growth Characteristics, and Promising Applications. *J. Mater. Chem. A* 5, (2017).
7. Yoshimura, T., Tatsuura, S. & Sotoyama, W. Polymer films formed with monolayer growth steps by molecular layer deposition. *Appl Phys Lett* 59, 482–484 (1991).
8. Loscutoff, P. W., Lee, H.-B.-R. & Bent, S. F. Deposition of Ultrathin Polythiourea Films by Molecular Layer Deposition. *Chemistry of Materials* 22, 5563–5569 (2010).
9. Ivanova, T. v, Maydannik, P. S. & Cameron, D. C. Molecular layer deposition of polyethylene terephthalate thin films. *Journal of Vacuum Science & Technology A* 30, 01A121 (2011).

10. Adamczyk, N., Dameron, A. & George, S. M. Molecular Layer Deposition of Poly(p - phenylene terephthalamide) Films Using Terephthaloyl Chloride and p - Phenylenediamine. *Langmuir* 24, 2081–2089 (2008).
11. Du, Y. & George, S. M. Molecular Layer Deposition of Nylon 66 Films Examined Using in Situ FTIR Spectroscopy. *The Journal of Physical Chemistry C* 111, 8509–8517 (2007).
12. George, S. M., Yoon, B. & Dameron, A. A. Surface Chemistry for Molecular Layer Deposition of Organic and Hybrid Organic–Inorganic Polymers. *Acc Chem Res* 42, 498–508 (2009).
13. Kerckhove, K. et al. On the Transformation Behaviour of “Alucones”, deposited by Molecular Layer Deposition, into nanoporous Al₂O₃ layers. *Dalton Transactions* 47, (2018).
14. Kerckhove, K. et al. Molecular Layer Deposition of “titanicone”, a titanium-based hybrid material, as an electrode for lithium-ion batteries. *Dalton Trans.* 45, (2015).
15. Sundberg, P. & Karppinen, M. Organic and inorganic-organic thin film structures by molecular layer deposition: A review. *Beilstein journal of nanotechnology* 5, 1104–1136 (2014).
16. Dameron, A. A. et al. Molecular layer deposition of alucone polymer films using trimethylaluminum and ethylene glycol. *Chemistry of Materials* 20, 3315–3326 (2008).
17. Peng, Q., Gong, B., VanGundy, R. M. & Parsons, G. N. ‘Zincone’ zinc oxide - Organic hybrid polymer thin films formed by molecular layer deposition. *Chemistry of Materials* 21, 820–830 (2009).
18. Yoon, B., O’Patches, J. L., Seghete, D., Cavanagh, A. S. & George, S. M. Molecular layer deposition of hybrid organic-inorganic polymer films using diethylzinc and ethylene glycol. *Chemical Vapor Deposition* 15, 112–121 (2009).
19. Abdulagatov, A. I. et al. Molecular layer deposition of titanicone films using TiCl₄ and ethylene glycol or glycerol: Growth and properties. *Chemistry of Materials* 24, 2854–2863 (2012).

20. Abdulagatov, A. I. et al. Molecular Layer Deposition and Thermal Transformations of Titanium(Aluminum)-Vanadium Hybrid Organic-Inorganic Films. *Russian Journal of Applied Chemistry* 91, 347–359 (2018).
21. Molina Piper, D. et al. Reversible High Capacity Si Nanocomposite Anodes Enabled By Molecular Layer Deposition. (2013).
22. Klepper, K., Nilsen, O. & Fjellvåg, H. Deposition of thin films of organic–inorganic hybrid materials based on aromatic carboxylic acids by atomic layer deposition. *Dalton Trans* 39, 11628–11635 (2010).
23. Sood, A., Sundberg, P., Malm, J. & Karppinen, M. Layer-by-layer deposition of Ti–4,4'-oxydianiline hybrid thin films. *Applied Surface Science - APPL SURF SCI* 257, 6435–6439 (2011).
24. Sundberg, P. & Karppinen, M. Organic–Inorganic Thin Films from TiCl₄ and 4-Aminophenol Precursors: A Model Case of ALD/MLD Hybrid-Material Growth? *Eur J Inorg Chem* 2014, (2014).
25. Sood, A., Sundberg, P. & Karppinen, M. ALD/MLD of novel layer-engineered Zn-based inorganic-organic hybrid thin films using heterobifunctional 4-aminophenol as an organic precursor. *Dalton Trans* 42, (2013).
26. Lee, Y., Yoon, B., Cavanagh, A. & George, S. M. Molecular Layer Deposition of Aluminum Alkoxide Polymer Films Using Trimethylaluminum and Glycidol. *Langmuir* 27, 15155–15164 (2011).
27. Gong, B. & Parsons, G. Caprolactone Ring-Opening Molecular Layer Deposition of Organic-Aluminum Oxide Polymer Films. *ECS Journal of Solid State Science and Technology* 1, P210–P215 (2012).
28. Chen, C. et al. Nanoporous Nitrogen-Doped Titanium Dioxide with Excellent Photocatalytic Activity under Visible Light Irradiation Produced by Molecular Layer Deposition. *Angew Chem Int Ed Engl* 52, (2013).
29. Lee, B. H., Anderson, V. R. & George, S. M. Molecular layer deposition of zirconia and ZrO₂/zirconia alloy films: Growth and properties. *Chemical Vapor Deposition* 19, 204–212 (2013).

30. Momtazi, L., Sønsteby, H. H., Dartt, D. A., Eidet, J. R. & Nilsen, O. Bioactive titaminates from molecular layer deposition. *RSC Adv* 7, 20900–20907 (2017).
31. Momtazi, L., Dartt, D. A., Nilsen, O. & Eidet, J. R. Molecular layer deposition builds biocompatible substrates for epithelial cells. *J Biomed Mater Res A* 106, 3090–3098 (2018).
32. Momtazi, L., Sønsteby, H. H. & Nilsen, O. Biocompatible organic-inorganic hybrid materials based on nucleobases and titanium developed by molecular layer deposition. *Beilstein Journal of Nanotechnology* 9, 399–411 (2019).
33. Putkonen, M. et al. Atomic layer deposition and characterization of biocompatible hydroxyapatite thin films. *Thin Solid Films* 517, 5819–5824 (2009).
34. Puvvada, R. U. et al. Bacterial Growth and Death on Cotton Fabrics Conformally Coated with ZnO Thin Films of Varying Thicknesses via Atomic Layer Deposition (ALD). *JOM* 71, 178–184 (2019).
35. Liang, X., Lynn, A. D., King, D. M., Bryant, S. J. & Weimer, A. W. Biocompatible interface films deposited within porous polymers by atomic layer deposition (ALD). *ACS Appl Mater Interfaces* 1, 1988–1995 (2009).
36. Panchawagh, H. V. et al. A flip-chip encapsulation method for packaging of MEMS actuators using surface micromachined polysilicon caps for BioMEMS applications. *Sens Actuators A Phys* 134, 11–19 (2007).
37. Yan, N. & Chen, X. Sustainability: Don't waste seafood waste. *Nature* 524, 155–157 (2015).
38. Jayakumar, R., Nair, A., Rejinold, N. S., Maya, S. & Nair, S. v. Doxorubicin-loaded pH-responsive chitin nanogels for drug delivery to cancer cells. *Carbohydr Polym* 87, 2352–2356 (2012).
39. Khor, E. & Lim, L. Y. Implantable applications of chitin and chitosan. *Biomaterials* 24, 2339–2349 (2003).

40. Giuseppe, A. di, Crucianelli, M., Passacantando, M., Nisi, S. & Saladino, R. Chitin- and chitosan-anchored methyltrioxorhenium: An innovative approach for selective heterogeneous catalytic epoxidations of olefins. *J Catal* 276, 412–422 (2010).
41. Muskovich, M. & Bettinger, C. J. Biomaterials-Based electronics: Polymers and interfaces for biology and medicine. *Adv Healthc Mater* 1, 248–266 (2012).
42. Parker, A., Lenau, T. & Saito, A. Biomimetics of Optical Nanostructures. in 55–116 (2012). doi:10.1201/b13067-4.
43. Nguyen, T. D. & Maclachlan, M. J. Biomimetic Chiral Nematic Mesoporous Materials from Crab Cuticles. *Adv Opt Mater* 2, 1031–1037 (2014).
44. Leila Binte Muhammad Yusof, N., Wee, A., Yong Lim, L. & Khor, E. Flexible chitin films as potential wound-dressing materials: wound model studies. (2003).
45. Montiel-González, Z., Luna-Bárceñas, G. & Mendoza-Galván, A. Thermal behaviour of chitosan and chitin thin films studied by spectroscopic ellipsometry. in *Physica Status Solidi (C) Current Topics in Solid State Physics* vol. 5 1434–1437 (2008).
46. Kikkawa, Y. et al. Interaction force of chitin-binding domains onto chitin surface. *Biomacromolecules* 9, 2126–2131 (2008).
47. Kittle, J. D. et al. Ultrathin chitin films for nanocomposites and biosensors. *Biomacromolecules* 13, 714–718 (2012).
48. Wang, C. & Esker, A. R. Nanocrystalline chitin thin films. *Carbohydr Polym* 102, 151–158 (2014).
49. Duan, B. et al. High strength films with gas-barrier fabricated from chitin solution dissolved at low temperature. *J Mater Chem A Mater* 1, 1867–1874 (2013).
50. Lee, L. et al. Ultra Gas-Proof Polymer Hybrid Thin Layer. *Nano Lett* 18, 5461–5466 (2018).
51. Park, J., Yoon, H. R., Khan, M. A., Cho, S. & Sung, M. M. Selective Infiltration in Polymer Hybrid Thin Films as a Gas-Encapsulation Layer for Stretchable Electronics. *ACS Appl Mater Interfaces* 12, 8817–8825 (2020).

52. Jen, S. H., Lee, B. H., George, S. M., McLean, R. S. & Carcia, P. F. Critical tensile strain and water vapor transmission rate for nanolaminate films grown using Al₂O₃ atomic layer deposition and alucone molecular layer deposition. *Appl Phys Lett* 101, 2010–2013 (2012).
53. Chen, G. et al. Low-temperature atomic layer deposition of Al₂O₃/alucone nanolaminates for OLED encapsulation. *RSC Adv* 9, 20884–20891 (2019).
54. Zhang, H. et al. Thin film encapsulation for organic light-emitting diodes using inorganic/organic hybrid layers by atomic layer deposition. *Nanoscale Res Lett* 10, (2015).
55. Shi, Y., Lee, Y. T. & Kim, A. Knudsen Diffusion Through Cylindrical Tubes of Varying Radii: Theory and Monte Carlo Simulations. *Transp Porous Media* 93, (2012).
56. Sauerbrey, G. Verwendung Von Schwingquarzen Zur Wagung Dunner Schichten Und Zur Mikrowagung. *European Physical Journal A* 155, 206–222 (1959).
57. Nomura, T., Watanabe, M. & West, T. S. Behaviour of piezoelectric quartz crystals in solutions with application to the determination of iodide. *Anal Chim Acta* 175, 107–116 (1985).
58. Thompson, M., Kipling, A., Duncan, W., Rajakovic, L. & Čavić-Vlasak, B. Thickness-shear-mode acoustic wave sensors in the liquid phase. A review. *Analyst* 116, 881–890 (1991).
59. Wong, T.-S. et al. Bioinspired self-repairing slippery surfaces with pressure-stable omniphobicity. *Nature* 477, 443–447 (2011).
60. Schroeder, T. B. H. et al. An electric-eel-inspired soft power source from stacked hydrogels. *Nature* 552, 214–218 (2017).
61. Siéfert, E., Reyssat, E., Bico, J. & Roman, B. Bio-inspired pneumatic shape-morphing elastomers. *Nat Mater* 18, 24–28 (2019).
62. Yeom, B. et al. Abiotic tooth enamel. *Nature* 543, 95–98 (2017).

63. Wu, S. et al. Long-lasting renewable antibacterial porous polymeric coatings enable titanium biomaterials to prevent and treat peri-implant infection. *Nat Commun* 12, 3303 (2021).
64. Wang, Z. et al. Advances and Prospects in Antibacterial-Osteogenic Multifunctional Dental Implant Surface. *Frontiers in Bioengineering and Biotechnology* vol. 10 Preprint at <https://doi.org/10.3389/fbioe.2022.921338> (2022).
65. Sui, J., Liu, S., Chen, M. & Zhang, H. Surface Bio-Functionalization of Anti-Bacterial Titanium Implants: A Review. *Coatings* 12, 1125 (2022).
66. Lew, D. P. & Waldvogel, F. A. Osteomyelitis. *The Lancet* 364, 369–379 (2004).
67. Meister, T. L. et al. Nanoscale copper and silver thin film systems display differences in antiviral and antibacterial properties. *Sci Rep* 12, 7193 (2022).
68. Wang, H. et al. Multi-target mode of action of silver against *Staphylococcus aureus* endows it with capability to combat antibiotic resistance. *Nat Commun* 12, 3331 (2021).
69. Li, X. et al. Recent developments in smart antibacterial surfaces to inhibit biofilm formation and bacterial infections. *J. Mater. Chem. B* 6, 4274–4292 (2018).
70. Ahmed, W., Zhai, Z. & Gao, C. Adaptive antibacterial biomaterial surfaces and their applications. *Mater Today Bio* 2, 100017 (2019).
71. Unepetty, A. et al. Strategies applied to modify structured and smooth surfaces: A step closer to reduce bacterial adhesion and biofilm formation. *Colloid Interface Sci Commun* 46, 100560 (2022).
72. Al-Sawalmih, A. et al. Microtexture and Chitin/Calcite Orientation Relationship in the Mineralized Exoskeleton of the American Lobster. *Adv Funct Mater* 18, 3307–3314 (2008).
73. Shamshina, J. L., Berton, P. & Rogers, R. D. Advances in Functional Chitin Materials: A Review. *ACS Sustain Chem Eng* 7, 6444–6457 (2019).
74. Verma, M. L., Kumar, S., Das, A., Randhawa, J. S. & Chamundeeswari, M. Chitin and chitosan-based support materials for enzyme immobilization and biotechnological applications. *Environ Chem Lett* 18, 315–323 (2020).

75. Lee, S., Hao, L., Park, J., Oh, D. & Hwang, D. Nanochitin and Nanochitosan: Chitin Nanostructure Engineering with Multiscale Properties for Biomedical and Environmental Applications. *Advanced Materials* (2022) doi:10.1002/adma.202203325.
76. Liao, J., Hou, B. & Huang, H. Preparation, properties and drug controlled release of chitin-based hydrogels: An updated review. *Carbohydr Polym* 283, 119177 (2022).
77. Tang, H. et al. High-strength paper enhanced by chitin nanowhiskers and its potential bioassay applications. *Int J Biol Macromol* 150, 885–893 (2020).
78. Narkevicius, A. et al. Revealing the Structural Coloration of Self-Assembled Chitin Nanocrystal Films. *Advanced Materials* (2022) doi:10.1002/adma.202203300.
79. Yang, K. et al. Pseudosolvent Intercalator of Chitin: Self-Exfoliating into Sub-1 nm Thick Nanofibrils for Multifunctional Chitinous Materials. *Adv Mater* 33, e2007596 (2021).
80. Yang, X., Liu, J., Pei, Y., Zheng, X. & Tang, K. Recent Progress in Preparation and Application of Nano-Chitin Materials. *Energy & Environmental Materials* 3, (2020).
81. Gregorczyk, K. & Knez, M. Hybrid Nanomaterials through Molecular and Atomic Layer Deposition: Top Down, Bottom up, and In-between Approaches to Make and Modify New Materials. *Prog Mater Sci* 75, 1–37 (2016).
82. George, S. M., Yoon, B. & Dameron, A. Surface Chemistry for Molecular Layer Deposition of Organic and Hybrid Organic–Inorganic Polymers. *Acc Chem Res* 42, 498–508 (2009).
83. Puurunen, R. et al. 121301 Surface chemistry of atomic layer deposition: A case study for the trimethylaluminum/water process (52 pages). *J Appl Phys* 97, 121301 (2005).
84. Feng, M. et al. Direct conversion of shrimp shells to O-acylated chitin with antibacterial and anti-tumor effect by natural deep eutectic solvent. *Green Chemistry* 21, (2018).
85. Sajomsang, W. & Gonil, P. Preparation and characterization of α -chitin from cicada sloughs. *Materials Science and Engineering: C* 30, 357–363 (2010).

86. Kaya, M., Tozak, K. Ö., Baran, T., Sezen, G. & Sargin, I. Natural porous and Nano fiber chitin structure from *Gammarus Argaeus* (Gammaridae Crustacea). *EXCLI J* 12, 503–510 (2013).
87. Oh, D., Shin, S., Lim, C. & Hwang, D. Dopamine-Mediated Sclerotization of Regenerated Chitin in Ionic Liquid. *Materials* 6, 3826–3839 (2013).
88. Feng, M. et al. One-step preparation of an antibacterial chitin/Zn composite from shrimp shells using urea-Zn(OAc)₂·2H₂O aqueous solution. *Green Chem.* 20, 2212–2217 (2018).
89. Lichtenegger, H., Schöberl, T., Bartl, M., Waite, H. & Stucky, G. High Abrasion Resistance with Sparse Mineralization: Copper Biomineral in Worm Jaws. *Science* 298, 389–392 (2002).
90. Lee, S. M. et al. Greatly increased toughness of infiltrated spider silk. *Science* (1979) 324, 488–492 (2009).
91. Lichtenegger, H. C., Schöberl, T., Bartl, M. H., Waite, H. & Stucky, G. D. High Abrasion Resistance with Sparse Mineralization: Copper Biomineral in Worm Jaws. *Science* (1979) 298, 389–392 (2002).
92. Jia, T., Fu, F., Yu, D., Cao, J.-L. & Sun, G. Facile synthesis and characterization of N-doped TiO₂/C nanocomposites with enhanced visible-light photocatalytic performance. *Appl Surf Sci* 430, (2017).
93. Triunfo, M. et al. Characterization of chitin and chitosan derived from *Hermetia illucens*, a further step in a circular economy process. *Sci Rep* 12, 6613 (2022).
94. Vasconcelos, C., Dittrich, M. & McKenzie, J. A. Evidence of microbiocoenosis in the formation of laminae in modern stromatolites. *Facies* 60, 3–13 (2014).
95. Macías-Sánchez, E., Willinger, M. G., Pina, C. & Checa, A. Transformation of ACC into aragonite and the origin of the nanogranular structure of nacre. *Sci Rep* 7, (2017).
96. Politi, Y. et al. Nano-channels in the spider fang for the transport of Zn ions to cross-link His-rich proteins pre-deposited in the cuticle matrix. *Arthropod Struct Dev* 46, (2016).

97. Wang, C. et al. Crystal and electronic structure of lithiated nanosized rutile TiO₂ by electron diffraction and electron energy-loss spectroscopy. *Appl Phys Lett* 94, 233116 (2009).
98. Kucharska, M., Sikora, M., Brzoza-Malczewska, K. & Owczarek, M. Antimicrobial Properties of Chitin and Chitosan. in 169–187 (2019). doi:10.1002/9781119450467.ch7.
99. Abdel-Mohsen, A. M. et al. Novel chitin/chitosan-glucan wound dressing: Isolation, characterization, antibacterial activity and wound healing properties. *Int J Pharm* 510, (2016).
100. Howell, M., Daniel, J. & Brown, P. Live Cell Fluorescence Microscopy to Observe Essential Processes During Microbial Cell Growth. *Journal of Visualized Experiments* 2017, (2017).
101. Bakshi, S. et al. Non-perturbative Imaging of Nucleoid Morphology in Live Bacterial Cells during Antimicrobial Peptide Attack. *Appl Environ Microbiol* 80, (2014).
102. Ashurbekova, K. et al. Biocompatible Silicon-Based Hybrid Nanolayers for Functionalization of Complex Surface Morphologies. *ACS Appl Nano Mater* 5, 2762–2768 (2022).
103. Alonso-Lerma, B. et al. High performance crystalline nanocellulose using an ancestral endoglucanase. *Commun Mater* 1, 57 (2020).
104. Feng, G. et al. Bacterial attachment and biofilm formation on surfaces are reduced by small-diameter nanoscale pores: How small is small enough? *NPJ Biofilms Microbiomes* 1, (2015).
105. Angelov, O., Stoyanova, D., Ivanova, I. & Todorova, S. Antimicrobial effect of Al₂O₃, Ag and Al₂O₃/Ag thin films on *Escherichia coli* and *Pseudomonas putida*. *J Phys Conf Ser* 764, 012015 (2016).
106. Sorrentino, R. et al. Reduced bacterial adhesion on ceramics used for arthroplasty applications. *J Eur Ceram Soc* 38, 963–970 (2018).

107. Barandiaran, L. et al. Enzymatic upgrading of nanochitin using an ancient lytic polysaccharide monoxygenase. *Commun Mater* 3, (2022).
108. Selenius, O., Korpela, J., Salminen, S. & Gómez-Gallego, C. Effect of chitin and chitooligosaccharide on in vitro growth of *Lactobacillus rhamnosus* GG and *Escherichia coli* TG. *Applied Food Biotechnology* 5, 163–172 (2018).
109. Kubacka, A. et al. Understanding the antimicrobial mechanism of TiO₂-based nanocomposite films in a pathogenic bacterium. *Sci Rep* 4, (2014).
110. Kumaravel, V. et al. Antimicrobial TiO₂ nanocomposite coatings for surfaces, dental and orthopaedic implants. *Chemical Engineering Journal* 416, 129071 (2021).
111. Yang, J. et al. Gallium–Carbenicillin Framework Coated Defect-Rich Hollow TiO₂ as a Photocatalyzed Oxidative Stress Amplifier against Complex Infections. *Adv Funct Mater* 30, (2020).
112. Zheng, K., Li, S., Jing, L., Chen, P. & Xie, J. Synergistic Antimicrobial Titanium Carbide (MXene) Conjugated with Gold Nanoclusters. *Adv Healthc Mater* 9, (2020).
113. Hermansson, M. The DLVO theory in microbial adhesion. *Colloids Surf B Biointerfaces* 14, 105–119 (1999).
114. Redman, J. A., Walker, S. L. & Elimelech, M. Bacterial Adhesion and Transport in Porous Media: Role of the Secondary Energy Minimum. *Environ Sci Technol* 38, 1777–1785 (2004).
115. Poortinga, A., Bos, R., Norde, W. & Busscher, H. Electric double layer interactions in bacterial adhesion to surfaces. *Surf Sci Rep* 47, 1–32 (2002).
116. Boks, N., Norde, W., van der Mei, H. & Busscher, H. Forces involved in bacterial adhesion to hydrophilic and hydrophobic surfaces. *Microbiology (Reading)* 154, 3122–3133 (2008).
117. Rijnaarts, H. H. M., Norde, W., Lyklema, J. & Zehnder, A. J. B. DLVO and steric contributions to bacterial deposition in media of different ionic strengths. *Colloids Surf B Biointerfaces* 14, 179–195 (1999).

118. Günther, J. et al. Differentiating *Staphylococcus aureus* from *Escherichia coli* mastitis: *S. aureus* triggers unbalanced immune-dampening and host cell invasion immediately after udder infection. *Sci Rep* 7, 4811 (2017).
119. Romaniuk, J. & Cegelski, L. Bacterial cell wall composition and the influence of antibiotics by cell-wall and whole-cell NMR. *Philosophical Transactions of the Royal Society B: Biological Sciences* 370, (2015).
120. Mai-Prochnow, A., Clauson, M., Hong, J. & Murphy, A. B. Gram positive and Gram negative bacteria differ in their sensitivity to cold plasma. *Sci Rep* 6, 38610 (2016).
121. Sonohara, R., Muramatsu, N., Ohshima, H. & Kondo, T. Difference in surface properties between *Escherichia coli* and *Staphylococcus aureus* as revealed by electrophoretic mobility measurements. *Biophys Chem* 55 3, 273–7 (1995).
122. Abbaszadegan, A. et al. The Effect of Charge at the Surface of Silver Nanoparticles on Antimicrobial Activity against Gram-Positive and Gram-Negative Bacteria: A Preliminary Study. *J Nanomater* 2015, 8 (2015).
123. Chen, Y.-M., Chung, Y.-C., Wang, L.-W., Chen, K.-T. & Li, S.-Y. Antibacterial properties of chitosan in waterborn pathogen. *J Environ Sci Health A Tox Hazard Subst Environ Eng* 37, 1379–1390 (2002).
124. Xiao, B., Wan, Y., Zhao, M., Liu, Y. & Zhang, S. Preparation and characterization of antimicrobial chitosan-N-arginine with different degrees of substitution. *Carbohydr Polym* 83, 144–150 (2011).
125. Renger, C. et al. Colloid probe investigation of the stabilization mechanism in aqueous 1,2-propanediol nano-zirconia dispersions. *Physical Chemistry Chemical Physics - PHYS CHEM CHEM PHYS* 6, (2004).
126. Hashiba, M., Okamoto, H., Nurishi, Y. & Hiramatsu, K. Dispersion of ZrO₂ particles in aqueous suspensions by ammonium polyacrylate. *J Mater Sci* 24, 873–876 (1989).
127. Angelova, M. I. & Dimitrov, D. S. Liposome Electro formation. *Faraday Discuss. Chem. SOC* vol. 81 (1986).

128. Oh, J. K. et al. The influence of surface chemistry on the kinetics and thermodynamics of bacterial adhesion. *Sci Rep* 8, 17247 (2018).
129. Chung, Y.-C. et al. Relationship between antibacterial activity of chitosan and surface characteristics of cell wall. *Acta Pharmacol Sin* vol. 25 <http://www.ChinaPhar.com> (2004).
130. Scardino, A. J., Guenther, J. & de Nys, R. Attachment point theory revisited: the fouling response to a microtextured matrix. *Biofouling* 24, 45–53 (2008).
131. Angelova, M. I. & Dimitrov, D. S. Liposome electroformation. *Faraday Discuss. Chem. Soc.* 81, 303–311 (1986).
132. Aktas, O. C. et al. Enhanced fibroblast cell adhesion on Al/Al₂O₃ nanowires. *Appl Surf Sci* 257, 3489–3494 (2011).
133. Meretoja, V. v, Rossi, S., Peltola, T., Pelliniemi, L. J. & Närhi, T. O. Adhesion and proliferation of human fibroblasts on sol-gel coated titania. *J Biomed Mater Res A* 95A, 269–275 (2010).
134. Iglin, V. et al. The effect of Sol-gel alumina biocomposite on the viability and morphology of dermal human fibroblast cells. *ACS Biomater Sci Eng* XXXX, (2020).
135. MAROUDAS, N. G. Chemical and Mechanical Requirements for Fibroblast Adhesion. *Nature* 244, 353–354 (1973).
136. Sun, Q., Hou, Y., Chu, Z. & Wei, Q. Soft overcomes the hard: Flexible materials adapt to cell adhesion to promote cell mechanotransduction. *Bioact Mater* 10, 397–404 (2022).
137. Pelham, R. J. & Wang, Y. Cell locomotion and focal adhesions are regulated by substrate flexibility. *Proceedings of the National Academy of Sciences* 94, 13661–13665 (1997).
138. Breathnach, A. S. Development and Differentiation of Dermal Cells in Man. *Journal of Investigative Dermatology* 71, 2–8 (1978).
139. OMAGARI, N. & OGAWA, K. Three Dimensional Arrangement of Fibrocytes in the Dermal Papilla of the Human Sole Skin. *Okajimas Folia Anat Jpn* 67, 195–202 (1990).

140. van Exan, R. J. & Hardy, M. H. The differentiation of the dermis in the laboratory mouse. *American Journal of Anatomy* 169, 149–164 (1984).
141. Grinnell, F., Ho, C.-H., Tamariz, E., Lee, D. & Skuta, G. Dendritic Fibroblasts in Three-dimensional Collagen Matrices. *Mol Biol Cell* 14, 384–395 (2003).
142. Rampioni, G., D'Angelo, F., Leoni, L. & Stano, P. Gene-Expressing Liposomes as Synthetic Cells for Molecular Communication Studies. *Front Bioeng Biotechnol* 7, (2019).
143. Majhy, B., Priyadarshini, P. & Sen, A. Effect of surface energy and roughness on cell adhesion and growth -facile surface modification for enhanced cell culture †. *RSC Adv* 11, 15467–15476 (2021).
144. Gentile, F. et al. Cells preferentially grow on rough substrates. *Biomaterials* 31, 7205–7212 (2010).
145. Francis, A. Biological evaluation of preceramic organosilicon polymers for various healthcare and biomedical engineering applications: A review. *J Biomed Mater Res B Appl Biomater* 109, 744–764 (2021).
146. Pryce Lewis, H. G., Edell, D. J. & Gleason, K. K. Pulsed-PECVD Films from Hexamethylcyclotrisiloxane for Use as Insulating Biomaterials. *Chemistry of Materials* 12, 3488–3494 (2000).
147. O'Shaughnessy, W., Gao, M. & Gleason, K. Initiated Chemical Vapor Deposition of Trivinyltrimethylcyclotrisiloxane for Biomaterial Coatings. *Langmuir* 22, 7021–7026 (2006).
148. Kazimierczak, P. & Przekora, A. Osteoconductive and Osteoinductive Surface Modifications of Biomaterials for Bone Regeneration: A Concise Review. *Coatings* 10, (2020).
149. Knez, M., Nielsch, K. & Niinistö, L. Synthesis and Surface Engineering of Complex Nanostructures by Atomic Layer Deposition. *Advanced Materials* 19, 3425–3438 (2007).

150. George, S. M., Yoon, B. & Dameron, A. Surface Chemistry for Molecular Layer Deposition of Organic and Hybrid Organic–Inorganic Polymers. *Acc Chem Res* 42, 498–508 (2009).
151. Malygin, A. A., Drozd, V. E., Malkov, A. A. & Smirnov, V. M. From V. B. Aleskovskii's "Framework" Hypothesis to the Method of Molecular Layering/Atomic Layer Deposition. *Chemical Vapor Deposition* 21, 216–240 (2015).
152. Ashurbekova, K., Ashurbekova, K., Botta, G., Yurkevich, O. & Knez, M. Vapor phase processing: a novel approach for fabricating functional hybrid materials. *Nanotechnology* 31, 342001 (2020).
153. Ashurbekova, K. et al. Molecular layer deposition of hybrid siloxane thin films by ring opening of cyclic trisiloxane (V3D3) and azasilane. *Chemical Communications* 56, 8778–8781 (2020).
154. Ashurbekova, K. et al. Ultrathin Hybrid SiAlCOH Dielectric Films through Ring-Opening Molecular Layer Deposition of Cyclic Tetrasiloxane. *Chemistry of Materials* 33, 1022–1030 (2021).
155. Ashurbekova, K. et al. Radical-triggered cross-linking for molecular layer deposition of SiAlCOH hybrid thin films. *Chemical Communications* 57, 2160–2163 (2021).
156. Momtazi, L., Sønsteby, H. H. & Nilsen, O. Biocompatible organic-inorganic hybrid materials based on nucleobases and titanium developed by molecular layer deposition. *Beilstein Journal of Nanotechnology* 9, 399–411 (2019).
157. Momtazi, L., Dartt, D. A., Nilsen, O. & Eidet, J. R. Molecular layer deposition builds biocompatible substrates for epithelial cells. *J Biomed Mater Res A* 106, 3090–3098 (2018).
158. Launer, P. & Arkles, B. Infrared Analysis of Organosilicon Compounds. in 175–178 (2013).
159. Gates, S. et al. Preparation and structure of porous dielectrics by plasma enhanced chemical vapor deposition. *J Appl Phys* 101, 94103 (2007).

160. Burkey, D. D. & Gleason, K. K. Temperature-resolved Fourier transform infrared study of condensation reactions and porogen decomposition in hybrid organosilicon-porogen films. *Journal of Vacuum Science & Technology A* 22, 61–70 (2003).
161. Wang, Q. et al. Interface engineering of an AlNO/AlGa_N/Ga_N MIS diode induced by PEALD alternate insertion of AlN in Al₂O₃. *RSC Adv.* 7, 11745–11751 (2017).
162. Casserly, T. & Gleason, K. Chemical Vapor Deposition of Organosilicon Thin Films from Methylmethoxysilanes. *Plasma Processes and Polymers* 2, 679–687 (2005).
163. Oh, J. K. et al. The influence of surface chemistry on the kinetics and thermodynamics of bacterial adhesion. *Sci Rep* 8, 17247 (2018).
164. Silva, G. Neuroscience nanotechnology: Progress, opportunities and challenges. *Nat Rev Neurosci* 7, 65–74 (2006).
165. Denes, E., Barriere, G., Poli, E. & Lévèque, G. Alumina Biocompatibility. *J Long Term Eff Med Implants* 28, (2018).
166. Jackson, N., Keeney, L. & Mathewson, A. Flexible-CMOS and Biocompatible Piezoelectric AlN material for MEMS Applications. *Smart Mater Struct* 22, 115033 (2013).
167. Jackson, N., Olszewski, O. Z., O'Murchu, C. & Mathewson, A. Shock-induced aluminum nitride based MEMS energy harvester to power a leadless pacemaker. *Sens Actuators A Phys* 264, (2017).
168. Zhou, J. et al. The effects of surface topography of nanostructure arrays on cell adhesion. *Physical Chemistry Chemical Physics* 20, 22946–22951 (2018).
169. Khraiche, M. L., Jackson, N. & Muthuswamy, J. Early onset of electrical activity in developing neurons cultured on carbon nanotube immobilized microelectrodes. in *2009 Annual International Conference of the IEEE Engineering in Medicine and Biology Society* 777–780 (2009). doi:10.1109/IEMBS.2009.5333590.
170. Salloum, D. S., Olenych, S. G., Keller, T. C. S. & Schlenoff, J. B. Vascular Smooth Muscle Cells on Polyelectrolyte Multilayers: Hydrophobicity-Directed Adhesion and Growth. *Biomacromolecules* 6, 161–167 (2005).

171. Guo, S. et al. Parallel Control over Surface Charge and Wettability Using Polyelectrolyte Architecture: Effect on Protein Adsorption and Cell Adhesion. *ACS Appl Mater Interfaces* 8, (2016).
172. Wei, J. et al. Adhesion of mouse fibroblasts on hexamethyldisiloxane surfaces with wide range of wettability. *J Biomed Mater Res B Appl Biomater* 81, 66–75 (2007).
173. Cai, S. et al. Recent advance in surface modification for regulating cell adhesion and behaviors. *Nanotechnol Rev* 9, 971–989 (2020).
174. Hoogenboom, R. & Schlaad, H. Bioinspired Poly(2-oxazoline)s. *Polymers (Basel)* 3, 467–488 (2011).
175. Adams, N. & Schubert, U. S. Poly (2-oxazolines) in biological and biomedical application contexts. *Adv Drug Deliv Rev* 59, 1504–1520 (2007).
176. Sedlacek, O., Monnery, B. D., Filippov, S. K., Hoogenboom, R. & Hruby, M. Poly(2-Oxazoline)s – Are They More Advantageous for Biomedical Applications Than Other Polymers? *Macromol Rapid Commun* 33, 1648–1662 (2012).
177. Luxenhofer, R. et al. Poly(2-oxazoline)s as Polymer Therapeutics. *Macromol Rapid Commun* 33, 1613–1631 (2012).
178. R. de la Rosa, V. Poly(2-oxazoline)s as materials for biomedical applications. *J Mater Sci Mater Med* 25, (2013).
179. Glassner, M., Vergaelen, M. & Richard, H. Poly(2-oxazoline)s: A comprehensive overview of polymer structures and their physical properties. *Polym Int* 67, (2017).
180. Maechling, C. et al. Synthesis and adsorption of a poly(N-acetyleneimine)-polyethyleneoxide-poly (N-acetyleneimine) triblock-copolymer at a silica/solution interface. Influence of its preadsorption on platelet adhesion and fibrinogen adsorption. *J Biomed Mater Res* 23, 1395–1410 (1990).
181. Park, Y., Kang, Y. S. & Chung, D. Formation and blood compatibility of thin layers of hyperbranched polymers on polyurethane films. *e-Polymers* 2, (2002).
182. Gundloori, R. Gelatin hydrogels: Enhanced biocompatibility, drug release and cell viability. *J Mater Sci Mater Med* 19, 2351–2358 (2008).

183. Sedlacek, O., Monnery, B., Filippov, S., Richard, H. & Hruby, M. Poly(2-Oxazoline)s - Are They More Advantageous for Biomedical Applications Than Other Polymers? *Macromol Rapid Commun* 33, 1648–1662 (2012).
184. Wang, Y., Bai, L., Tan, L., chen, juan & Liu, S. Preparation and characterizations of poly(2-methyl-2-oxazoline) based antifouling coating by thermally induced immobilization. *J. Mater. Chem. B* 2, (2014).
185. Miyamoto, M., Naka, K., Shiozaki, M., Chujo, Y. & Saegusa, T. Preparation and enzymatic activity of poly[(N-acylimino) ethylene]-Modified catalase. *Macromolecules* 23, (1990).
186. Woodle, M., Engbers, C. & Zalipsky, S. New Amphipatic Polymer-Lipid Conjugates Forming Long-Circulating Reticuloendothelial System-Evading Liposomes. *Bioconjug Chem* 5, 493–496 (1994).
187. Hsiue, G.-H., Chiang, H.-Z., Wang, C.-H. & Juang, T.-M. Nonviral Gene Carriers Based on Diblock Copolymers of Poly(2-ethyl-2-oxazoline) and Linear Polyethylenimine. *Bioconjug Chem* 17, 781–786 (2006).
188. Waschinski, C. J., Herdes, V., Schueler, F. & Tiller, J. C. Influence of Satellite Groups on Telechelic Antimicrobial Functions of Polyoxazolines. *Macromol Biosci* 5, 149–156 (2005).
189. Waschinski, C. J. & Tiller, J. C. Poly(oxazoline)s with Telechelic Antimicrobial Functions. *Biomacromolecules* 6, 235–243 (2005).
190. Miyamoto, M., Aoi, K., Yamanaka, H. & Saegusa, T. Preparation of Block Copolymer Consisting of Poly(2-methyl-2-oxazoline) and Poly(propylene oxide) Blocks. A New Nonionic Surfactant. *Polym J* 24, 405–409 (1992).
191. Schubert, U., Hartlieb, M. & Kempe, K. Covalently cross-linked poly(2-oxazoline) materials for biomedical applications - from hydrogels to self-assembled and templated structures. *J Mater Chem B* 3, (2014).

192. Lüdtkke, K., Jordan, R., Hommes, P., Nuyken, O. & Naumann, C. Lipopolymers from New 2-Substituted-2-Oxazolines for Artificial Cell Membrane Constructs. *Macromol Biosci* 5, 384–393 (2005).
193. SZWARC, M. 'Living' Polymers. *Nature* 178, 1168–1169 (1956).
194. Kobayashi, S. & Uyama, H. Polymerization of cyclic imino ethers: From its discovery to the present state of the art. *J Polym Sci A Polym Chem* 40, 192–209 (2002).
195. Kobayashi, S. *Catalysis in precision polymerization*. (John Wiley, 1997).
196. Kagiya, T., Narisawa, S., Maeda, T. & Fukui, K. Ring-opening polymerization of 2-substituted 2-oxazolines. *J Polym Sci B* 4, 441–445 (1966).
197. Seeliger, W. et al. Recent Syntheses and Reactions of Cyclic Imidic Esters. *Angew Chem Int Ed Engl* 5, 875–888 (1966).
198. Glassner, M., Vergaelen, M. & Richard, H. Poly(2-oxazoline)s: A comprehensive overview of polymer structures and their physical properties. *Polym Int* 67, (2017).
199. Fijten, M. W. M., Hoogenboom, R. & Schubert, U. S. Initiator effect on the cationic ring-opening copolymerization of 2-ethyl-2-oxazoline and 2-phenyl-2-oxazoline. *J Polym Sci A Polym Chem* 46, 4804–4816 (2008).
200. Pepper, D. C. Cationic ring-opening polymerization, Part 2: Synthetic applications (*Advances in Polymer Science*, Volumes 68/69). By S. Penczek, P. Kubisa and K. Matyjaszewski, Springer-Verlag, Berlin Heidelberg, 1985. pp. 300, price DM 188.00. ISBN 3-540-13781-5. *British Polymer Journal* 18, 399–400 (1986).
201. Park, J.-S. & Kataoka, K. Precise Control of Lower Critical Solution Temperature of Thermosensitive Poly(2-isopropyl-2-oxazoline) via Gradient Copolymerization with 2-Ethyl-2-oxazoline as a Hydrophilic Comonomer. *Macromolecules* 39, 6622–6630 (2006).
202. Shen, J. & Zheng, S. Comparative studies on miscibility and phase behavior of linear and star poly(2-methyl-2-oxazoline) blends with poly(vinylidene fluoride). *J Polym Sci B Polym Phys* 44, 942–952 (2006).
203. Warakowski, J. M. & Thill, B. P. Evidence for long chain branching in polyethyloxazoline. *J Polym Sci A Polym Chem* 28, 3551–3563 (1990).

204. Hoogenboom, R., Wiesbrock, F., Leenen, M. A. M., Meier, M. A. R. & Schubert, U. S. Accelerating the Living Polymerization of 2-Nonyl-2-oxazoline by Implementing a Microwave Synthesizer into a High-Throughput Experimentation Workflow. *J Comb Chem* 7, 10–13 (2005).
205. Wiesbrock, F., Hoogenboom, R., Leenen, M. A. M., Meier, M. A. R. & Schubert, U. S. Investigation of the living cationic ring-opening polymerization of 2-methyl-, 2-ethyl-, 2-nonyl-, and 2-phenyl-2-oxazoline in a single-mode microwave reactor. *Macromolecules* 38, 5025–5034 (2005).
206. Wiesbrock, F., Hoogenboom, R., Abeln, C. H. & Schubert, U. S. Single-mode microwave ovens as new reaction devices: accelerating the living polymerization of 2-ethyl-2-oxazoline. *Macromol Rapid Commun* 25, 1895–1899 (2004).
207. Mansfield, E., Sillence, K., Hole, P., Williams, A. & Khutoryanskiy, V. POZylation; a new approach to enhance nanoparticle diffusion through mucosal barriers. *Nanoscale* 7, (2015).
208. Abilova, G. et al. Chitosan/poly(2-ethyl-2-oxazoline) films for ocular drug delivery: Formulation, miscibility, in vitro and in vivo studies. *Eur Polym J* 116, (2019).
209. Colombo, A. et al. Highly transparent poly(2-ethyl-2-oxazoline)-TiO₂ nanocomposite coatings for the conservation of matte painted artworks. *RSC Adv* 5, 84879–84888 (2015).
210. Svoboda, J., Sedlacek, O., Riedel, T., Hruby, M. & Pop-Georgievski, O. Poly(2-oxazoline)s One-Pot Polymerization and Surface Coating: From Synthesis to Antifouling Properties Out-Performing Poly(ethylene oxide). *Biomacromolecules* 20, (2019).
211. Konradi, R., Pidhatika, B., Mühlebach, ‡ & Textor, M. Poly-2-methyl-2-oxazoline: A Peptide-like Polymer for Protein-Repellent Surfaces. *Langmuir* 24, 613–616 (2008).
212. Vlasi, E., Papagiannopoulos, A. & Pispas, S. Hydrolyzed Poly(2-phenyl-2-oxazoline)s in Aqueous Media and Biological Fluids. *Macromol Chem Phys* 219, 1800047 (2018).

213. Paulovicova, E., Kroneková, Z., Paulovičová, L., Majerčíková, M. & Kronek, J. Cell-Mediated Immunoreactivity of Poly(2-isopropenyl-2-oxazoline) as Promising Formulation for Immunomodulation. *Materials* 14, 1371 (2021).
214. Chistyakov, E., Filatov, S., Sulyanova, E. & Volkov, V. Determination of the Degree of Crystallinity of Poly(2-methyl-2-oxazoline). *Polymers (Basel)* 13, 4356 (2021).
215. Bouten, P. J. M., Lava, K., van Hest, J. C. M. & Hoogenboom, R. Thermal Properties of Methyl Ester-Containing Poly(2-oxazoline)s. *Polymers (Basel)* 7, 1998–2008 (2015).
216. Chistyakov, E., Filatov, S., Sulyanova, E. & Volkov, V. Determination of the Degree of Crystallinity of Poly(2-methyl-2-oxazoline). *Polymers (Basel)* 13, 4356 (2021).